# Rational Design of Advanced Materials for Li-Se and Na-Se Batteries

A thesis presented for the award of the degree of

**Doctor of Philosophy**

from

**University of Technology Sydney**

**By Fan Zhang, B.Sc., M.Sc.**

**October, 2021**

# Certificate of original authorship

I certify that the work in this thesis has not previously been submitted for a degree nor has it been submitted as part of requirements for a degree except as fully acknowledged within the text.

I also certify that the thesis has been written by me. Any help that I have got in my research work and the preparation of the thesis has been acknowledged.

In addition, I certify that all information sources and literature used in the thesis are indicated.

This research is supported by an Australian Government Research Training Program.

Fan Zhang

Production Note:
Signature removed prior to publication.

Sydney, Australia

Oct, 06 2021

# Acknowledgments

It has been three and a half years since I was enrolled as a PhD student in August 2017. It was hard time for me, at which time I dropped out of City University of Hong Kong and was confused about my future. However, thanks to my experience during PhD studies, I have received numerous help from the people and the institute to support me finishing my PhD study.

Firstly, I would like to express my sincere gratitude to my supervisor, Professor Guoxiu Wang, who has given me guidance and support in my academic activities as well as logical thinking. Professor Wang gave me insightful feedback, which pushed me to sharpen my idea and brought my work to a higher level. In addition, Professor Wang gave me a lot of opportunities to presenting in international conferences, communicating with academic masters, studying in advanced battery companies, he is never too stingy to give us opportunities to broaden our thoughts.

I would also like to express my deep-heart thanks to my co-supervisor, Professor Hao Liu, who was actually a friend to me. Professor Hao Liu offered a lot of help to my literature writing, especially in my first write-up. He also provided me with much financial support to my academic activities.

I would like to thank Dr. Jane Yao who was the lab manager in full responsibilities. During the 3 and a half years of my PhD studies, I have received tremendous help from her in my research activities and daily life. She was a very kind lab manager, helpful and responsible.

I would like to thank Professor Pan Xiong who offered much help during my literature writing and experiments. He was expertized in materials synthesis, materials characterization

and logical thinking. I improved my academic skills via the cooperation with Professor Pan Xiong - my friend.

I would also like to thank my colleagues at University of Technology Sydney, Dr. Bing Sun, Dr. Dawei Su, Dr. Dong Zhou, Dr. Liubin Dong, Dr. Huajun Tian, Dr. Xin Guo, Dr. Jinqiang Zhang, Dr. Yufei Zhao, Dr. Jing Xu, Dr. Weizhai Bao, Dr. Lin Liu, Shaoqi Hou, Xingxing Yu, Jiayan Liao, Yi Chen, Shijian Wang, Xiao Tang, Kang Yan, Xiaochun Gao Javad Safaei, Shuoqin Zhao, Tianyi Wang, Wang Yang, Wu Yang, Min Luo, Ziqi Guo, Anastasia Tkacheva, Tuhin Subhra Sahu, Pauline Jaumaux, and Yuhan Xie for all your kind assistance and collaboration during my Ph.D. study and life.

I appreciate the excellent technical support from Dr. Ronald Shimmon, Dr. Linda Xiao, Alexander Angeloski, Katie McBean, Herbert Yuan, Mark Berkahn, Mark Lockrey, and Geoff McCredie.

Financial support provided by UTS (International Research Scholarship & UTS President's Scholarship), Australian Research Council (ARC) through the ARC Future Fellow Project (FT180100705) and the Discovery Projects (DP160104340, DP170100436, and DP180102297) is gratefully acknowledged.

Lastly, I would like to express my deep thanks to my father (Yaowen Zhang), my mother (Xianxia Lv), my brother (Linchang Zhang) and his wife (Lihan Wang), my niece (Yuxian Zhang), who has provided great support to me during my PhD period of life.

Thanks to the happy experience with them, I not only developed well understanding in academics, but also developed my interests in a wide range of fields, including batteries, catalysis, fuel cells, carbon dioxide electrolysis, water electrolysis, industrial machining, machine learning, artificial intelligence, big data technologies, robots technologies, industrial

materials and manufacturing, self-media technologies, computer technology and global trading, full of expectations for the future.

# Abstract

The battery design, including cathodes, separators and anodes, has significant influence on the performance of the cell. This Ph.D. project focuses the novel materials design, e.g. cathode materials optimization and separator modification, for advanced lithium selenium (Li-Se) and sodium selenium (Na-Se) batteries. Both Li-Se and Na-Se batteries suffer from the severe shuttle effect and insufficient use of the active material, especially in the ether-based electrolyte system. General strategies such as providing strong chemical bonding in cathode side, blocking the shuttling effect via a 'defensive wall' on the separator are effective in resolving these issues, leading to improved electrochemical performance. A nitrogen and sulphur dual-doped hierarchical porous carbon (NSHPC) with interconnected conductive polyaniline (i-PANI) coating strategy is achieved via a carbonization process followed by *in-situ* polymerization of aniline. *Ex situ* characterizations and density functional theory (DFT) calculations demonstrate that the i-PANI coating and N, S dual-doping can provide both physical diffusion barrier and strong chemical affinity for polyselenides. In addition, the interconnected conductive polyaniline network enhances the conductivity for electrons and ions. With this strategy, the as-prepared cathode can deliver high reversible capacities and stable cycling performances.

Further investigation was conducted via preparing the MXene composite separator to regulate a preferable interface between the cathode and the separator. The hybrid separator can immobilize the polyselenides via enhanced Lewis acid-base interactions to the polyselenides. In addition, the incorporation of carbon nanotube (CNT) helps to improve the electrolyte infiltration and facilitate the ionic transport. *In situ* permeation experiments are conducted for the first time to visually study the behaviour of polyselenides, providing a insightful understanding of shuttling effect. When serving as the separators in both Li-Se and Na-Se batteries, it delivers high capacities and better cycling stabilities.

# Publication list

1. **Zhang, F.**; Xiong, P.; Guo, X.; Zhang, J.; Yang, W.; Wu, W.; Liu, H.; Wang, G., A nitrogen, sulphur dual-doped hierarchical porous carbon with interconnected conductive polyaniline coating for high-performance sodium-selenium batteries. *Energy Storage Materials* **2019,** *19*, 251-260.

2. **Zhang, F.**; Guo, X.; Xiong, P.; Zhang, J.; Song, J.; Yan, K.; Gao, X.; Liu, H.; Wang, G., Interface Engineering of MXene Composite Separator for High-Performance Li–Se and Na–Se Batteries. *Advanced Energy Materials* **2020,** *10* (20), 2000446.

3. Xiong, P.; **Zhang, F.**; Zhang, X.; Wang, S.; Liu, H.; Sun, B.; Zhang, J.; Sun, Y.; Ma, R.; Bando, Y.; Zhou, C.; Liu, Z.; Sasaki, T.; Wang, G., Strain engineering of two-dimensional multilayered heterostructures for beyond-lithium-based rechargeable batteries. *Nat Commun* **2020,** *11* (1), 3297.

4. **Zhang, F.**; Németh, K.; Bareño, J.; Dogan, F.; Bloom, I. D.; Shaw, L. L., Experimental and theoretical investigations of functionalized boron nitride as electrode materials for Li-ion batteries. *RSC Advances* **2016,** *6* (33), 27901-27914.

5. Xiao, J.; **Zhang, F.**; Tang, K.; Li, X.; Wang, D.; Wang, Y.; Liu, H.; Wu, M.; Wang, G., Rational Design of a P2-Type Spherical Layered Oxide Cathode for High-Performance Sodium-Ion Batteries. *ACS Cent Sci* **2019,** *5* (12), 1937-1945.

6. Tian, H.; Wang, T.; **Zhang, F.**; Zhao, S.; Wan, S.; He, F.; Wang, G., Tunable porous carbon spheres for high-performance rechargeable batteries. *Journal of Materials Chemistry A* **2018,** *6* (27), 12816-12841.

7. Yang, W.; Yang, W.; **Zhang, F.**; Wang, G.; Shao, G., Hierarchical Interconnected Expanded Graphitic Ribbons Embedded with Amorphous Carbon: An Advanced Carbon Nanostructure for Superior Lithium and Sodium Storage. *Small* **2018,** *14* (39), 1802221.

8. Wang, S.; Xiong, P.; Guo, X.; Zhang, J.; Gao, X.; **Zhang, F.**; Tang, X.; Notten, P. H. L.; Wang, G., A Stable Conversion and Alloying Anode for Potassium-Ion Batteries: A Combined Strategy of Encapsulation and Confinement. *Advanced Functional Materials* **2020,** *30* (27), 2001588.

9. Zhou, D.; Tkacheva, A.; Tang, X.; Sun, B.; Shanmukaraj, D.; Li, P.; **Zhang, F.**; Armand, M.; Wang, G., Stable Conversion Chemistry-Based Lithium Metal Batteries Enabled by Hierarchical Multifunctional Polymer Electrolytes with Near-Single Ion Conduction. *Angewandte Chemie International Edition* **2019,** *58* (18), 6001-6006.

10. Tian, H.; Tian, H.; Wang, S.; Chen, S.; **Zhang, F.**; Song, L.; Liu, H.; Liu, J.; Wang, G., High-power lithium-selenium batteries enabled by atomic cobalt electrocatalyst in hollow carbon cathode. *Nat Commun* **2020,** *11* (1), 5025.

11. Gao, H.; Guo, X.; Wang, S.; **Zhang, F.**; Liu, H.; Wang, G., Antimony-based nanomaterials for high-performance potassium-ion batteries. *EcoMat* **2020,** *2* (2), e12027.

12. Chen, L.; Liu, Y.; **Zhang, F.**; Liu, C.; Shaw, L. L., PVP-Assisted Synthesis of Uniform Carbon Coated Li2S/CB for High-Performance Lithium-Sulfur Batteries. *ACS Appl Mater Interfaces* **2015,** *7* (46), 25748-56.

13. Xu, S.; Yang, D.; **Zhang, F.**; Liu, J.; Guo, A.; Hou, F., Fabrication of NiCo2O4 and carbon nanotube nanocomposite films as a high-performance flexible electrode of supercapacitors. *RSC Advances* **2015,** *5* (90), 74032-74039.

14. Xiong, P.; Zhang, X.; **Zhang, F.**; Yi, D.; Zhang, J.; Sun, B.; Tian, H.; Shanmukaraj, D.; Rojo, T.; Armand, M.; Ma, R.; Sasaki, T.; Wang, G., Two-Dimensional Unilamellar Cation-Deficient Metal Oxide Nanosheet Superlattices for High-Rate Sodium Ion Energy Storage. *ACS Nano* **2018,** *12* (12), 12337-12346.

15. Guo Y.; Ma W.; **Zhang F.,** The Effect of PSN Content on MPB of $0.3Pb(Ni_{1/3}Nb_{2/3})O_3$-$0.7Pb(Zr_{1-x}T_x)O_3$ System, Journal of Materials Science: Materials in Electronics **2016**, 10.1007/s10854-015-3919-x.

# Table of Contents

# List of Figures

# List of Tables

# Chapter 1 Introduction

High-energy and low-cost rechargeable battery has been highly demanded for powering portable electronics, electric vehicles and renewable energy storage. Recently, selenium (Se), one of the chalcogen elements, has attracted considerable attention owing to its high specific capacity (678 mAh $g^{-1}$). The good conductivity of Se ($1 \times 10^{-3}$ S $m^{-1}$) endows it highly reactive with alkali metals through a conversion type reaction: $2M^{+} + Se + 2e^{-} \leftrightarrow M_2Se$, M=Li, Na. These features make it a promising cathode candidate with high energy densities for both Li and Na based batteries.

The first work on Li-Se and Na-Se batteries was first reported in 2012 by Professor Khalil Amine's group.[1] Their work investigated the electrode structural mechanisms during electrochemical process and showed that the Se cathodes are promising electrodes for both Li and Na based batteries. The high voltages of Li-Se batteries up to 4.6 V can also provide higher energy density and higher volumetric energy density than Li-S batteries. In the next year 2013, they further studied the crystalline phase transition of Li-Se batteries during battery cycling via the advanced *in situ* synchrotron high-energy X-ray diffraction method, which gave fundamental understanding in Li-Se systems.[2]

The discovery of the Se-based battery systems can be a good alternative to the S-based batteries. However, Se cathodes also suffer from rapid capacity decay and low Coulombic efficiency (CE) because of the shuttling of polyselenides from the cathode to the anode, which is a common issue in alkali-chalcogen batteries. Cathodes and separators are two of the most important components in the batteries.

Tremendous efforts have been devoted to the design of advanced cathode host materials to mitigate the shuttle effect. These designed cathode strategies include: employing porous carbon materials as the hosts; coating the cathode materials with graphene, metal oxide or conductive polymers; and hetero-atoms doping. In an early report, Professor Wang's group used the mesoporous carbon spheres to host selenium. As a result, the Se/mesoporous carbon composites delivered a reversible capacity over 1000 cycles in Li-Se batteries and 380 cycles in Na-Se batteries.[3] Liu et al. found that metal-

organic framework derived microporous carbon plyhedra (MICP) can be a promising host material for Se.[4] The interconnected micropores achieved a reasonable Se loading (51 wt%) and can provide a large surface area buffering the volume expansion of Se during cycling. However, the relatively weak physical interaction between Se and the carbon substrate cannot ensure an ultra-long and robust cycling performance. Heteroatoms doping in carbon can provide strong chemical binding between the doped carbon substrate and polyselenides. Nitrogen (N) is the most commonly employed doping element.[5-7] Jiang et al. used the N doped microporous carbon spheres as the host materials for Li-Se batteries, in which the N doping can improve the electric conductivity and the reactivity.[5] The N-doped carbon carbon can be directly derived from many sources, such as metal organic frameworks (MOFs)[6, 8, 9] and polypyrrole[7].

Moreover, heteroatoms dual-doping can further enhance the chemical affinity to the polyselenides compared the single atom doping. In 2018, an interesting work reported by Zhao et al. indicated that N, O dual-doping can provide strong chemical bonding to the polyselenides.[10] With the N, O dual-doped hierarchical porous carbon-selenium cathodes, the as-assembled Li-Se battery can deliver a high reversible 545 mAh $g^{-1}$ at 0.5C after 1500 cycles and Na-Se battery can retain 402 mAh $g^{-1}$ after 500 cycles at 0.5 C. Similar results have also been reported by Yu's group, in which they have prepared the 3D interconnected CNT wrapped N,O dual-doped porous carbon skeletons and Se composite cathode (Se@NOPC-CNT).[11] The Se@NOPC-CNT composite cathode can perform well in both Na-Se and K-Se batteries.

Besides the cathode materials engineering, functional separators/interlayers have been prepared to inhibit the shuttle effect in Se based batteries.[12-15] So far, several materials have been investigated as the functianl compoents, such as metal oxide, graphene, porous carbon, covalent organic frameworks (COFs) and etc. The functional separators/interlayers can not only provide physical block, but also provide strong chemcial affinity to the polyselenides based on the functional materials.

The main purpose of this thesis is to improve the electrochemical performances of Li-Se and Na-Se batteries by preparing novel advanced materials for use in the cathode side and

separators. The outline of each chapter is listed below,

- Chapter 1 introduces the general background of Se cathode materials for both Li-Se and Na-Se batteries, and point out the issues and research interests in this field.

- Chapter 2 presents a literature review in the pioneer works of Li-Se and Na-Se batteries, in terms of mechanisms study, preparation method of cathode composite materials, porous carbon-based host materials, heteroatom-doped carbon hosts, coating strategies of cathode materials, development of separators and interlayers for Li-Se and Na-Se batteries

- Chapter 3 provides the detailed methodology of research applied in this thesis. The material synthesis methods, physical characterizations methods, the electrodes preparation methods and electrochemical measurement methods are all illustrated.

- Chapter 4 show the investigations of advanced cathode materials design for Na-Se batteries. An N, S dual-doped hierarchical porous carbon/Se composite coated with interconnected polyaniline (i-PANI@NSHPC/Se) was prepared via the *in situ* polymerization process. Influences of the N, S dual-doping and interconnected PANI coating on the electrochemical performance are systematically studied.

- Chapter 5 introduces a novel self-assembled cetrimonium bromide (CTAB)/carbon nanotube (CNT)/Ti3C2Tx MXene composite modified polypropylene (PP) (CCNT/MXene/PP) separator which works well in both Li-Se and Na-Se batteries. The mechanism of electrochemical behavior of Li-Se battery have been studied using the *in situ* permeation test.

- Chapter 6 summarizes the work in this thesis and provides an outlook for the future research.

1. Abouimrane, A.; Dambournet, D.; Chapman, K. W.; Chupas, P. J.; Weng, W.; Amine, K., A new class of lithium and sodium rechargeable batteries based on selenium and selenium-sulfur as a positive electrode. *J Am Chem Soc* **2012,** *134* (10), 4505-8.

2. Cui, Y.; Abouimrane, A.; Lu, J.; Bolin, T.; Ren, Y.; Weng, W.; Sun, C.; Maroni, V. A.; Heald, S. M.; Amine, K., (De)lithiation mechanism of Li/SeS(x) (x = 0-7) batteries determined by in situ synchrotron X-ray diffraction and X-ray absorption spectroscopy. *J Am Chem Soc* **2013,** *135* (21), 8047-56.

3. Luo, C.; Xu, Y.; Zhu, Y.; Liu, Y.; Zheng, S.; Liu, Y.; Langrock, A.; Wang, C., Selenium@Mesoporous Carbon Composite with Superior Lithium and Sodium Storage Capacity. *ACS Nano* **2013,** *7* (9), 8003-8010.

4. Liu, Y.; Si, L.; Zhou, X.; Liu, X.; Xu, Y.; Bao, J.; Dai, Z., A selenium-confined microporous carbon cathode for ultrastable lithium–selenium batteries. *J. Mater. Chem. A* **2014,** *2* (42), 17735-17739.

5. Jiang, Y.; Ma, X.; Feng, J.; Xiong, S., Selenium in nitrogen-doped microporous carbon spheres for high-performance lithium–selenium batteries. *Journal of Materials Chemistry A* **2015,** *3* (8), 4539-4546.

6. Li, Z.; Yin, L., MOF-derived, N-doped, hierarchically porous carbon sponges as immobilizers to confine selenium as cathodes for Li-Se batteries with superior storage capacity and perfect cycling stability. *Nanoscale* **2015,** *7* (21), 9597-606.

7. Yi, Z.; Yuan, L.; Sun, D.; Li, Z.; Wu, C.; Yang, W.; Wen, Y.; Shan, B.; Huang, Y., High-performance lithium–selenium batteries promoted by heteroatom-doped microporous carbon. *Journal of Materials Chemistry A* **2015,** *3* (6), 3059-3065.

8. Dong, W.; Chen, H.; Xia, F.; Yu, W.; Song, J.; Wu, S.; Deng, Z.; Hu, Z.-Y.; Hasan, T.; Li, Y.; Wang, H.; Chen, L.; Su, B.-L., Selenium clusters in Zn-glutamate MOF derived nitrogen-doped hierarchically radial-structured microporous carbon for advanced

rechargeable Na–Se batteries. *Journal of Materials Chemistry A* **2018,** *6* (45), 22790-22797.

9. Park, S. K.; Park, J. S.; Kang, Y. C., Metal-Organic-Framework-Derived N-Doped Hierarchically Porous Carbon Polyhedrons Anchored on Crumpled Graphene Balls as Efficient Selenium Hosts for High-Performance Lithium-Selenium Batteries. *ACS Appl Mater Interfaces* **2018,** *10* (19), 16531-16540.

10. Zhao, X.; Yin, L.; Zhang, T.; Zhang, M.; Fang, Z.; Wang, C.; Wei, Y.; Chen, G.; Zhang, D.; Sun, Z.; Li, F., Heteroatoms dual-doped hierarchical porous carbon-selenium composite for durable Li–Se and Na–Se batteries. *Nano Energy* **2018,** *49*, 137-146.

11. Yao, Y.; Chen, M.; Xu, R.; Zeng, S.; Yang, H.; Ye, S.; Liu, F.; Wu, X.; Yu, Y., CNT Interwoven Nitrogen and Oxygen Dual-Doped Porous Carbon Nanosheets as Free-Standing Electrodes for High-Performance Na-Se and K-Se Flexible Batteries. *Adv Mater* **2018,** *30* (49), e1805234.

12. Yang, Y.; Hong, X.-J.; Song, C.-L.; Li, G.-H.; Zheng, Y.-X.; Zhou, D.-D.; Zhang, M.; Cai, Y.-P.; Wang, H., Lithium bis(trifluoromethanesulfonyl)imide assisted dual-functional separator coating materials based on covalent organic frameworks for high-performance lithium–selenium sulfide batteries. *Journal of Materials Chemistry A* **2019,** *7* (27), 16323-16329.

13. Yang, Z.; Zhu, K.; Dong, Z.; Jia, D.; Jiao, L., Stabilization of Li-Se Batteries by Wearing PAN Protective Clothing. *ACS Appl Mater Interfaces* **2019,** *11* (43), 40069-40077.

14. Fang, R.; Zhou, G.; Pei, S.; Li, F.; Cheng, H. M., Localized polyselenides in a graphene-coated polymer separator for high rate and ultralong life lithium-selenium batteries. *Chem Commun (Camb)* **2015,** *51* (17), 3667-70.

15. Mukkabla, R.; Kuldeep; Killi, K.; Shivaprasad, S. M.; Deepa, M., Metal Oxide Interlayer for Long-Lived Lithium-Selenium Batteries. *Chemistry* **2018,** *24* (65), 17327-17338.

# Chapter 2 Literature Revew

## 2.1 Overview

Among the existing energy storage and conversion technologies, batteries have exceptional advantages such as promising energy density, high versatility and portability. The 2019 Nobel Prize in Chemistry was jointly awarded to John B. Goodenough, M. Stanley Whittingham, and Akira Yoshino, recognizing their pioneering work on lithium-ion batteries (LIBs). Lithium ion (Li-ion) battery is one of the most famous battery system which was firstly commercialized in 1991 by SONY Company. Over the past 30 years, significant commercial and academic progress have been made on the Li-ion batteries. The rising star – Telsa has accelerated the application of Li-ion batteries in the field of electric vehicles, which could be a revolution for the future travelling.

Cathode is one of the most important component in a battery. Sulfur, the second element in group 16 (VI A), has emerged as a promising cathode materials for lithium sulfur (Li-S) batteries due to its nontoxic, cost-effective, high theoretical specific capacity and volumetric capacity density.[1] However, the intrinsic insulation and large volume expansion of sulfur during charge and disrchage hinder its large-scale applications. As a competitive cathode material to sulfur, lithium selenium (Li-Se) batteries show superior volumetric capacity to the Li-S batteries (Se, 3268 mAh $cm^{-3}$ vs. S, 3467 mAh $cm^{-3}$) and higher electrical conductivity (Se, $1x10^{-3}$ S $m^{-1}$ vs. S, $5x10^{-28}$ S $m^{-1}$).[2] In addition, Li-Se batteries also deliver a higher output voltage (~0.5 V higher than that of Li-S batteries) which will provide a higher energy density as a result.[3]

Furthermore, selenium can also act as a superior cathode material for sodium metal based battery. Unlike sodium sulphur (Na-S) battery, selenium shows high activity with sodium at

room temperature and have a high theoretical capacity of 678 mAh $g^{-1}$.[4] As it is well known, sodium ion (Na-ion) battery, another most studied system, is emerging as the next generation large-scale energy storage system due to its earth abundance and cost effective. As an alternative to Li-ion battery, the commercialization of Na-ion battery would reduce the battery cost by nearly 30% or even higher.[4] This chapter summarizes the recent progress of Li-Se and Na-Se batteries in terms of reaction mechanisms, synthesis methods, host materials for Se, modification of cathode composite materials and separators.

## 2.2 Basics of Li-Se and Na-Se batteries

Since the first pioneering work by Amine's group in 2012, Li-Se and Na-Se batteries have been widely investigated (**Figure 2.1**) with the overall redox reaction of $M + Se + 2e^- \leftrightarrow M_2Se$ (M = Li, Na). However, both Li-Se and Na-Se batteries suffer from the well-known 'shuttle effect' reaction, in which the polyselenides occurs during the first discharge and shuttling across the separator during the initial charge. The polyselenides shuttling will inevitably lose the active material from the cathode, followed by the parasitic reaction between polyselenides and the metal anodes.[5] So far, various strategies have been developed to relieve the polyselenides shuttling, mainly via physical confinement,[6-7] chemical adsorption,[5, 8] electrostatic attraction[2] and manipulating redox reaction pathway.[9]

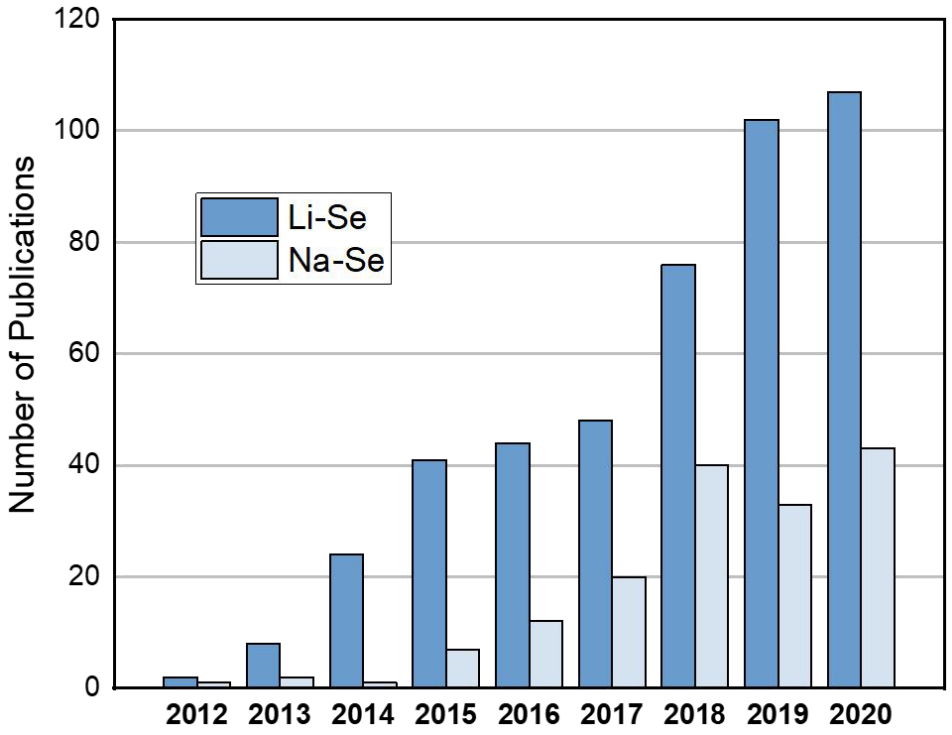


**Figure 2.1** Number of annual publications in Li-Se and Na-Se batteries during the period of 2012-2020. Data collected from Institute for Scientific Information (ISI) Web of Science on 20th January 2021.

## 2.3 Mechanism study of Li-Se and Na-Se batteries

In 2012, Professor Amine's group reported the first rechargeable Li-Se and Na-Se batteries in carbonate-based (ethylene carbonate (EC)/ethyl methyl carbonate (EMC)) electrolyte.[10] In their work, they found that Li-Se battery undergoes a single phase transition from Se to $Li_2Se$ during the initial discharge, while it forms an intermediate phase when discharging to the final product ($Na_2Se$). During the following initial charge process, there were apparent overcharging capacities in both Li-Se and Na-Se batteries. The overcharging behaviour suggest a partial dissolution of the soluble $M_nSe$ (M=Li, Na, n<2) electrode – known as the 'shuttle effect'.

After that in 2013, Amine's group further investigated the mechanism of Li-Se batteries in ether-based electrolyte using the *in situ* synchrotron X-ray diffraction and X-ray absorption spectroscopy.[11] Unlike the electrochemical behaviour in carbonate-based electrolyte, Se is reduced to the polyselenides, $Li_2Se_n$ ($n \geq 4$), $Li_2Se_2$, and $Li_2Se$ sequentially during the discharge followed by the oxidization of $Li_2Se$ to Se through $Li_2Se_n$ ($n \geq 4$) during charging in the ether-based electrolyte (**Figure 2.2(a)**). They further concluded that the ether-based electrolyte can enable higher efficiency and higher stability for the Li-Se battery system compared to that of carbonate-based electrolyte.

To investigate the (de)lithiation mechanism of Li-Se batteries with Se cathodes in different phases, Zhou *et al.* prepared amorphous Se (a-Se) nanowires (NWs), crystalline Se (c-Se) NWs and crystalline/amorphous Se (c/a-Se) NWs.[12] As indicated in **Figure 2.2(b-d)**, both a-Se and c/a-Se show three obvious plateaus during the lithiation process. However, the battery with c-Se cathode only presents one platform (~1.55 V) and the Se helical chains are reduced fast to $Li_2Se$ with a low capacity. All batteries were conducted in carbonate-based electrolyte. It is found that amorphous Se has more active sites than the crystalline Se due to the 'dangling bonds' and high specific surface area in a-Se.[3] The high active sites render the initial fast lithiation for a-Se and c/a-Se compared to that of c-Se.[12]

In a most recent study, Zhao et al. has manipulated the redox reaction pathway for enhancing the electrochemical performance of Li-Se batteries via adding diphenyl diselenide (DPDSe) as an electrolyte additive.[9] The DPDSe molecule contains a Se-Se bond that can reversibly break and store two $Li^+$ during cycling. As shown in **Figure 2.2(e)**, the Se-Se bonds in DPDSe undergoes homolytic cleavage into two PhSe• radicals which will form PhSeLi or PhSeSe•, ending with PhSeLi and $Li_2Se$ during discharge. In the following charge process, PhSeLi is de-lithiated to PhSe• and PhSeSe• radicals, forming the final products of

PhSeSePh (DPDSe) and PhSeSeSePh (DPTSe), respectively. The formation of DPTSe can entrap the extra Se (polyselenides) in the electrolyte and prohibit the shuttling effects. In this study, the authors also indicated that an optimized mass ratio of DPDSe to Se (2:1) can provide best electrochemical performance in terms of stability and efficiency compared to the other ratios (1:1 and 3:1).

To investigate the redox reaction mechanism of Na-Se batteries, Li *et al.* studied the sodiation reactions with Se nanotube cathode and $Na_2O$ solid electrolyte using *in situ* transmission electron microscopy (TEM) method.[4] Unlike the one-step lithiation reaction of Li-Se battery in **Figure 2.2(f)**, Na-Se battery exhibits a three-step reaction mechanism: Se $\rightarrow Na_{0.5}Se \rightarrow Na_2Se_2 \rightarrow Na_2Se$. In addition, they also find that the sodiation kinetics is about 4-5 times faster than that of lithiation in general, which is attributed to the improved electronic and ionic conductivity of Na-based intermediates compared to that of Li-based intermediates during sodiation/lithiation. At the meantime, Goodenough *et al.* studied the electrochemical behaviour of $Se_x$ molecules in microporous slits in carbon with carbonate electrolyte.[13] Similar to Li's work,[4] it shows a sequential redox reaction for Na-Se batteries and a single-step reaction for Li-Se batteries in **Figure 2.2(g, h)**. The interesting thing is that, unlike Zhou's work which also employed carbonate-based electrolyte, the single-step reaction for Se is attribute to existence of the single-chain Se molecules in microporous slits in carbon. They further concluded that the behaviour of confined Se in microporous slits in carbon is similar to that of sulphur.

To further clarify the electrochemistry of Se in micropores, Professor Mitlin's group reported the site-specific sodiation mechanisms of selenium in microporous carbon host recently.[14] In their work, they confined Se in a representative nanoporous carbon host architecture. As shown in **Figure 2.2(i)**, the Se chains are progressively cut to polyselenides

with various length upon sodiation. They also found that the Se nearest the interface of carbon/Se sodiated first, forming a core-shell compositional profile. After the first cycle, nanoscale fractures originating from the physical separation of Se from the carbon host will occur, leading to extra interfaces and faster $Na^+$ diffusion rates.

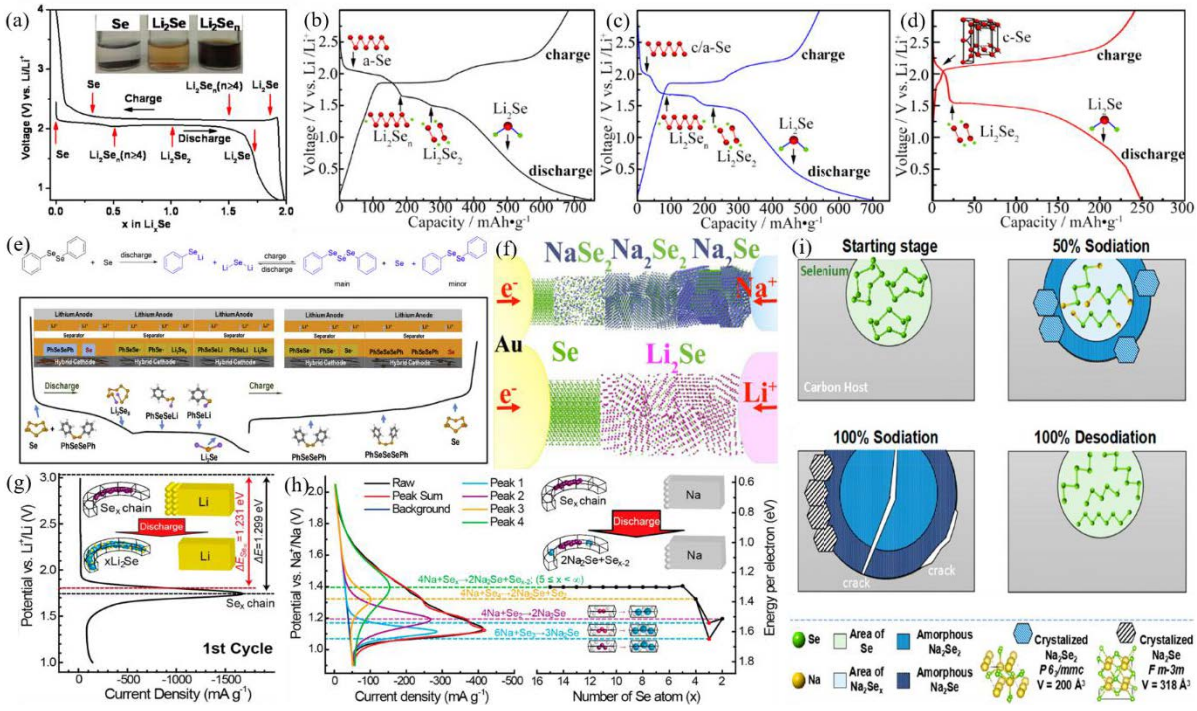


**Figure 2.2 (a)** Representation of cathode phase evolution during charge and discharge of a Li/Se cell in an ether-based electrolyte,[11] **(b-d)** Initial charge−discharge curves of the **(b)** a-Se, **(c)** c/a-Se, and **(d)** c-Se NWs (600 rpm, 10 h) at a current density of 0.1 C between 0.01 and 3.0 V. (The red ball is Se and green ball is Li),[12] **(e)** The scheme of proposed redox reactions of the Li|Se-DPDSe cell,[9] **(f)** Schematic illustration of sodiation and lithiation of selenium nanotubes. Three different phases appeared in sodiation due to the alloying reaction. In lithiation, selenium transforms to polycrystalline $Li_2Se$ phase,[4] **(g)** Electrochemistry of a Li−$Se_x$ battery in Cycle 1, **(h)** Electrochemistry of a Na−$Se_x$ battery in Cycle 1,[13] **(i)** Scheme summary of the Key Aspects of the Phase Transformation Sequence during Sodiation and Desodiation of Se-PCS.[14]

## 2.4 Development of cathode composite materials for Li-Se and Na-Se batteries

Similar to Li-S and Na-S batteries, the Se-based batteries also suffer from the well-known 'shuttle effect' together with the significant volume expansion during cycling. As previously reported, there existed 88% and 336% volume expansion for Li-Se and Na-Se batteries upon fully lithiation and sodiation, respectively.[4] The large volume expansion will result in the shrinkage of the active material (Se) in the following charge process, which inevitably cause cracks in the bulk Se cathode. Both the 'shuttle effect' and cracks will lead to fast capacity decay by loss of active materials and poor ionic/electric conductivity. In order to address these issues, loading of Se into conductive hosts is the most effective way. Herein, we summarize the cathode materials preparation methods, cathode host materials and cathode materials improvement strategies for Li-Se and Na-Se batteries.

### 2.4.1 Preparation of cathode composite materials

Cathode material is one the most important component for both Li-Se and Na-Se batteries. So far, various methods have been developed to prepare the cathode composite materials. Zhou *et al.* prepared selenium nanowires with different phases.[12] Amorphous Se nanowires (a-Se NWs) was synthesized via a facile high-energy ball-milling method. Crystalline (c) and crystalline/amorphous (c/a) Se NWs were synthesized via subsequent annealing process of c-Se NWs. It revealed that the a-Se NWs exhibited the highest capacity while the c-Se NWs performed the worst. The favourable electrochemical performance of a-Se NWs could be attributed to the higher surface area of a-Se, in which the initial (de)lithiation process only occurred at the surface. However, a-Se NWs still suffer from fast capacity decay due to the severe shuttle effect. A universal method to relieve the

polyselenides shuttling is to incorporate the Se powder into conductive host via melt-diffusion process.

Shiraz et al. prepared Microporous carbon/Se (MPC/Se) composite with different Se loading of 50wt% (MPC/Se 50), 60wt% (MPC/Se 60) and 70wt% (MPC/Se 70) at 260 ºC for 12 h.[15] Due to the effective confinement of Se into the micropores MPC/Se 50 exhibits the best cycling performance and rate capability. The higher loading of Se in the cathode will lead to insufficient loading of Se in the micropores and significantly reduced Li-ion diffusion coefficient due to the existence of bulk Se nanoparticles on the surface of carbon. The presence of bulk Se is a common phenomenon when the melt-diffusion method is used, especially under high Se loadings.

Li *et al.* developed a novel baked-in-salt method to enable better infiltration of Se into metal-complex-derived porous carbon (Se/MnMC-B) in **Figure 2.3 (a)**.[16] During the infiltration process, Se is confined in the narrow space between two compact NaCl solid disks which avoids the need for protection with argon gas or vacuum. The baked-in-salt melt diffusion method not only facilitates the close combination of Se and the porous carbon host, but also achieves an effective high Se loading of 72 wt%. As a result, the Se/MnMC-B cathode (with 72% selenium loading) exhibits a high capacity of 580 mAh $g^{-1}$ over 1000 cycles at 1C, outstanding rate capability up to 20 C for Li-Se battery and a capacity of 535 mAh $g^{-1}$ for 150 cycle at 0.1 C.

After that, Yang *et al.* developed a vacuum calcination (VC) approach via directly heating carbon-coated Se wires at 500 ºC for 2 h in a vacuum-sealed glass bottle.[17] As shown in **Figure 2.3 (b)**, the Se wire turns from crystalline to amorphous and diffuse outward to form Se/carbon tubes (SeCT). In addition, the carbon matrix is reduced in terms of increased carbon/oxygen atomic ratio, leading to a higher electric conductivity. When paired with Na

metal anode, the SeCT cathode delivered impressive capacity retention of more than 90% after 1000 cycles at a high current density of 20 C.

Although the vacuum calcination method is efficient in incorporating Se into porous structures, it requires high temperature and high vacuum conditions which inevitably increases the cost of materials preparation. Wu et al. used lithium selenide ($Li_2Se$) nanoparticles as the active material, which was prepared via a facile chemical reaction between Se powder and Li super hydride solution (**Figure 2.3(c)**).[18] $Li_2Se$ is a stable solid state even under a high temperature of 700 ºC. When combining $Li_2Se$ with carbon via carbonization process, both C-$Li_2Se$ and C-$Li_2Se$@C composites exhibits high capacities and cycling stability. The use of dense C-$Li_2Se$ is also preferable for developing all-solid state Li-Se battery, enabling high volumetric energy density.

The solid selenium nanoparticles can also be prepared directly for use in Li-Se batteries. Wang *et al.* prepared selenium multiwalled carbon nanotubes composite (Se/MWCNTs) by a solution-based method.[19] The solution approach can reduce the particle size of the as-synthesized Se nanoparticles which uniformly distribute on MWCNTs. As a result, the Se/MWCNTs cathode exhibit good cycling and rate performance After that, Mukkabla *et al.* further synthesized Se/CTAB decorated MWCNTs composite (Se NPs@CTAB-MWCNTs) via a scalable solution phase method. During the reaction, Se NPs can be *in-situ* grown on the surface of MWCNTs in **Figure 2.3(d)**. Due to the absence of carbon black, the final product (Se NPs@CTAB-MWCNTs) can achieve a high Se content of 72 wt%. The high content of Se enables a high electrical conductivity and the porous structure of CTAB-MWCNTs traps the soluble polyselenides. As a result, the Se NPs@CTAB-MWCNTs presents a reasonable capacity during 500 cycles.

However, due to the weak physical interaction between Se and the carbon matrix, the shuttle effect is still serve which lead to unsatisfied cycling performance. Building up chemical binding between Se atoms and the substrates can greatly enhance the Se-substrate affinities. A self-repairing strategy has been developed by Professor Yang's group to prepare a Se-C chemically bonded Se/graphene composite (Se-GE). The Se-Ge composite was synthesized via a facile high-energy ball-milling process.

High-speed ball-milling treatment will induce the exfoliation of graphene sheet, activation of $sp^2$ C to $sp^3$ C in graphene and reconstruction of chemical bonds in Se, leading to new formed chemical binding between Se and graphene. As expected, the Se-GE cathode can deliver a stable cycling performance in the long run of 500 cycles. Besides, carbonization of Se/polymer composites can convert Se to chain-like $Se_x$ molecules which will be bonded to the carbonized polymer during heat treatment.[20-22] Polyacrylonitrile (PAN) is the most commonly used polymer, which was initially reported for producing sulphur/PAN composite.[23] As shown in **Figure 2.3(e)**, Guo *et al.* prepared a conductive selenized PAN composite via direct carbonization of Se/PAN composite at 500 ºC under argon atmosphere for 6 h.[21] During heat treatment, the $-CH_2$, $-CH_2$ -CN groups break and Se radicals then chemically combine with the positively polarized carbon atoms to form C-Se bonds. The authors believe that the selenized PAN composite is a type of Se-containing conductive polymer instead of Se trapped in carbonized PAN matrix. A new electrochemical reaction mechanism was developed that the nitrogen groups also contribute to the overall capacity and facilitate the redox reaction. As a result, the selenized polymer cathode delivers a stable cycling performance over 1000 cycles with a total capacity decay of 0.57% after the 2$^{nd}$ cycle.

Perylene-3,4,9,10-tetracarboxylic dianhydride (PTCDA), another kind of polymer, is also used to produce C/Se composite cathode.[22] Similar to that of selenized PAN, the

preparation of C/Se derived from PTCDA/Se can also be prepared via calcination process. Se can be physically encapsulated and chemically bonded by carbon, thus leading to mitigated polyselenides shuttling. The *in situ* formed C/Se composites exhibit superior cycling stability for both Li-ion and Na-ion batteries in carbonate-based electrolytes.

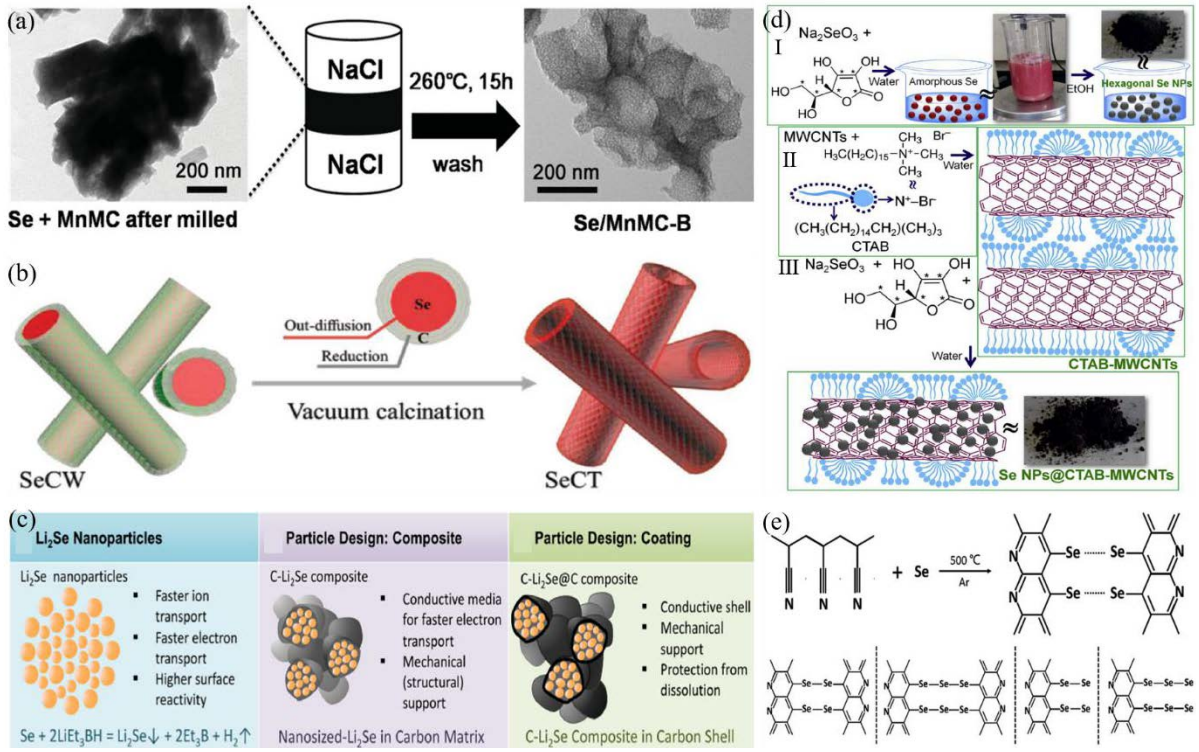


**Figure 2.3 (a)** Schematic of the baked-in-salt approach for confining selenium in a metal complex-derived porous carbon,[16] **(b)** Schematic illustration of the conversion of SeCW to SeCT,[17] **(c)** Concepts of Li2Se-based cathodes for Li and Li-ion batteries,[18] **(d)** Schematic of the preparation of (I) Se NPs, (II) CTAB-MWCNTs, and (III) the Se NPs@CTAB-MWCNTs composite,[24] **(e)** The reaction during heating and the possible molecular structure of the as-prepared selenized polyacrylonitrile composites.[21]

## 2.4.2 Porous carbon-based host materials

Carbon framework with porous structure is the most widely used host for loading Se and S cathodes due to the large surface area, fast electron/ion transport, buffer of the volume change during cycling.[7, 25] In addition, Se can exist in amorphous state which can render a preferable electrochemical activity. Specifically, carbon materials with micropores (d < 2 nm),[15, 26-30] mesopores (2< d < 50 nm)[31-34] and hierarchical pores[35-40] exhibit outstanding electrochemical performance for both Li-Se and Na-Se batteries.

### 2.4.2.1 Microporous carbon hosts

Micropores are ideal vessels for accommodating Se and immobilizing polyselenides. When loaded into the micropores, the small Se molecules become amorphous nature. In addition, the small pore size of the carbon can also facilitate the formation a compact and robust solid-electrolyte interface (SEI) with a low interfacial resistance. Feng and co-workers[28] synthesized carbon nanotubes (CNTs) microspheres full of micropores via an ultrasonic spray method, followed by a molten diffusion strategy of Se loading at 300 ºC (**Figure 2.4(a)**). They further did a heat-treatment under 350 ºC for 2 h to remove the excess Se particles on the surface of CNTs. The total specific surface area of CNTs microspheres is ~571.2 $m^2 g^{-1}$ with the average pore diameter of 1.9 nm, which enables a high Se loading of 73.3 wt% filling the micropores. Consequently, Se/CNTs microspheres exhibit a high capacity retention of 80% after 500 cycles at 1 C rate. However, in their work, they did not clearly point out the role of the micropres because they used both CNTs composites and CNTs microsperes as the hosts for Se. The better electrochemical performance of Se/CNTs microspheres than Se/CNTs composites suggests a more important influence of the microsphere structure on the battery rather than the micropores. Professor Liu's group[15]

reported polyvinylidene fluoride derived microporous carbon (MPC) via an activation-free approach (**Figure 2.4(b-d)**). The MPC-800 (synthesized at 800 ºC) has a high specific surface area of 830.0 $m^2$ $g^{-1}$ with fruitful micropores, which could effectively confine Se and reduce side reactions with electrolytes. As a result, The MPC-800/Se cathode, with 50wt% Se, exhibited a superior reversible capacity of 508.8 mAh $g^{-1}$ at 0.1 C over 100 cycles. They further concluded that the redox reaction can proceed fast with suitable content of Se (**Figure 2.4(c)**), while the reaction goes slowly and insufficiently if the Se content is too high to fill the micropores. Lei *et al.*[29] prepared microporous carbon spheres (MPCS) via a two-step hydrothermal followed by KOH activation method in **Figure 2.4(e)**. The MPCS/Se cathodes exhibit excellent electrochemical performance in both carbonate-based and ether-based electrolytes. Recently, Wang and co-workers[30] provided a new insight into the confinement effects in Li-Se batteries (**Figure 2.4(f)**). In their work, two porous carbon hosts with different pore distributions (MiC, ~1.02 nm and MeC, ~4.35 nm) were developed to evaluate the relationships between the pore structure of carbon and the electrode kinetics. It is revealed that the MiC/Se composite has better ionic and electronic conductivities compared to that of MeC/Se. The micropores (<1.35 nm) in MiC/Se can not only facilitate the formation of a compact and robust solid-electrolyte interface with a low interfacial resistance, but also alters the insulation nature of $Li_2Se$ due to the generation of itinerant electrons. As a result, the MiC/Se has favourable redox kinetics and high Se utilization.

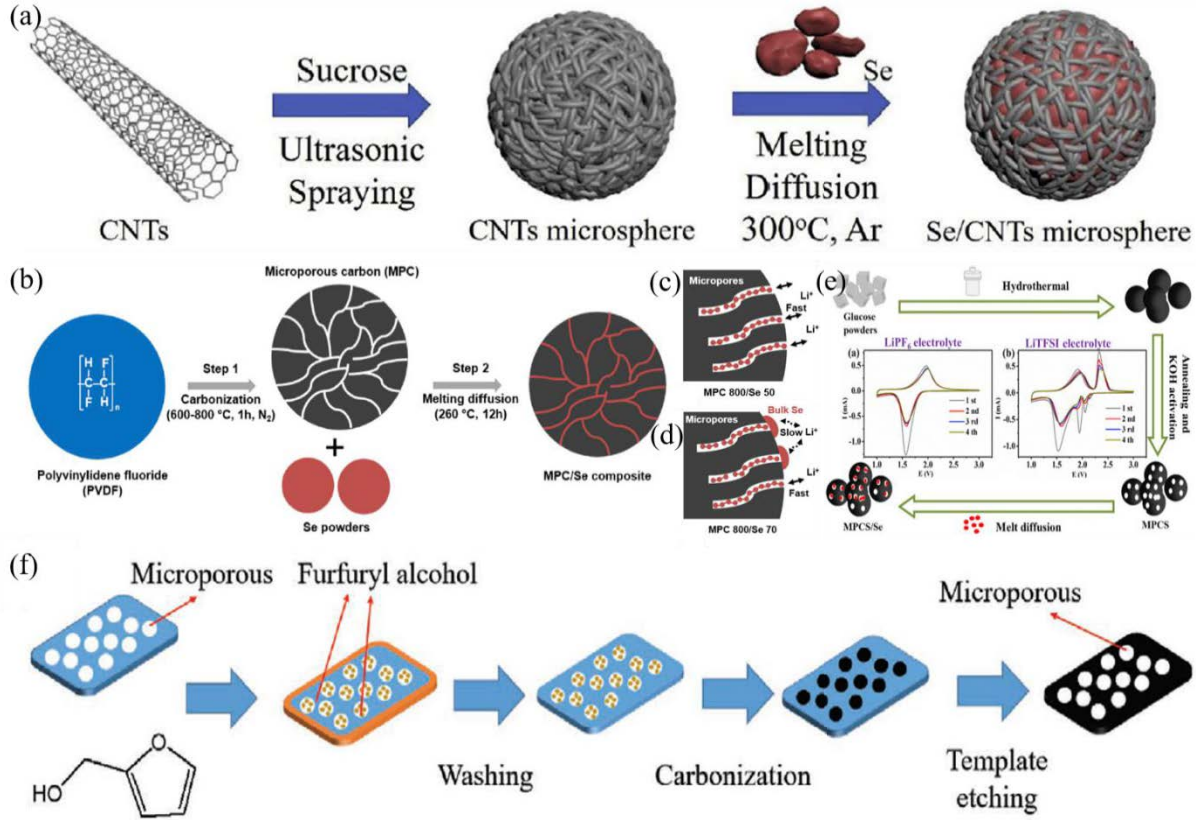


**Figure 2.4 (a)** Synthesis flow chart of Se/CNTs microspheres,[28] **(b)** Schematic illustration of the preparation process for microporous carbon (MPC) by the direct carbonization of PVDF at 600–800 ºC for 1 h in N2 atmosphere (Step 1), and for MPC/Se composites by melting diffusion of Se powders into MPC at 260 ºC for 12 h (Step 2). Schematics of **(c)** MPC 800/Se 50 with all Se infiltrated into microspore carbon, allowing fast Li-ion diffusion from electrolytes to Se and **(d)** MPC 800/ Se 70 with bulk Se distributed on the surface of carbon, which slows down diffusion of Li ions from/to Se in micropore carbon,[15] **(e)** Schematic preparation of microporous carbon spheres/ selenium composite (MPCS/Se)[29], **(f)** Schematic illustration of the synthesis process of microporous carbon (MiC) materials.[30]

### 2.4.2.2 Mesoporous carbon hosts

Mesopores hold a pore diameter between 2 and 50 nm, which means they can have the potential advantages of both micropores and macropores. The mesopores with small

diameters can act like micropores for better Se confinement while the larger ones can serve as macropores for hosting more active materials and better electrolyte transport, leading to satisfied electrochemical performance.[41]

An early study using the mesoporous carbon spheres as the host material for Se was reported Professor Wang's group.[31] Se was infused into the mesoporous carbon spheres under vacuum at 600 ºC. The mesopores can stabilize and trap the polyselenides during cycling. As a result, the $Se_8$/C composite cathode exhibits excellent electrochemical performance in low-cost carbonate-based electrolyte for both Li-ion and Na-ion batteries.

At the same time, Yang *et al.* reported ordered CMK-3 hosted Se cathode materials (Se/CMK-3) in Li-Se batteries.[32] As shown in **Figure 2.4(b),** there is no obvious bulk Se on surface of CMK-3 after heating treatment, indicative of effective infiltration of Se into the mesopores. The lithiation/delithiation mechanism of Se/CMK-3 is then proposed in **Figure 2.4(c)**. During the heating process, the trigonal Se transform to cyclic $Se_8$ molecules inside the mesopores of CMK-3. The $Se_8$ molecules then directly react with $Li^+$ to form the final $Li_2Se$ product without intermediates during the first discharge. Chain-like Se is formed instead of the original cyclic $Se_8$ molecules in the following charge process. It is revealed that the chain-like $Se_n$ molecules have better affinities to the carbon substrate compared to that of cyclic $Se_8$ molecules, which enables better electric conductivity and confinement of Se in the cathode materials.

In a traditional way of making cathode materials, carbon black, PVDF and solvent need to be incorporated to form a slurry. However, these additives will inevitably reduce the content of active material in the cathode, leading to a low overall capacity. Self-supported additive-free cathode materials are promising candidates to achieve high energy density batteries. In regard of this issue, Zeng *et al*. prepared a free-standing porous carbon

nanofibers/Se (Se@PCNFs) cathode via electrospinning method with Pluronic F127 as a template in **Figure 2.5(d-f)**.[42] Due to the introduce of Pluronic F127, PCNFs exhibit more mesopores with a high specific surface area of 936 $m^2$ $g^{-1}$, much higher than that of carbon nanofibers prepared without Pluronic F127 (f-PCNFs), 623 $m^2$ $g^{-1}$. As a result, the PCNFs can host a high Se mass loading of 52.3 wt%, higher than that of most slurry coating prepared electrodes if all other additives are taken into calculations. With the advantages of fruitful mesopores and interwoven network, Se@PCNFs can deliver a high capacity of 516 mAh $g^{-1}$ over 900 cycles without any capacity decay at 0.5 A $g^{-1}$ in Li-Se batteries. The composite cathode can also maintain a reversible of 520 mAh $g^{-1}$ after 80 cycles at 0.05 A $g^{-1}$ in Na-Se batteries.

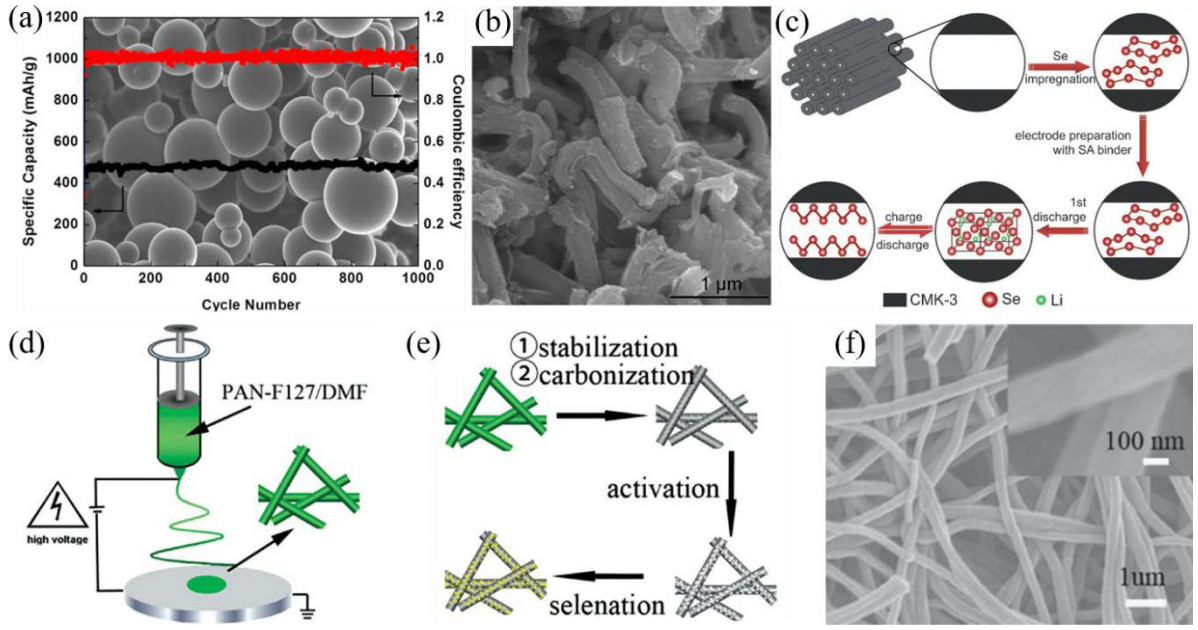


**Figure 2.5 (a)** SEM images of mesoporous carbon spheres and cycling performance of the Se/C composite for Li-Se battery,[31] **(b)** SEM images of Se/CMK-3, **(c)** proposed lithiation/delithiation processes of Se/CMK-3,[32] **(d, e)** Schematic illustration of the synthesis process of the Se@PCNFs electrode, **(f)** FESEM images of Se@PCNFs.[42]

### 2.4.2.3 Hierarchical porous carbon hosts

Hierarchical porous carbons (HPCs) possess a multimodal pore size distribution of micropores, mesopores, and/or macropores. HPCs show high electrochemically accessible surface area, short diffusion distance, and high mass transfer rate when served as electrode materials in energy storage devices. Furthermore, when used as host materials for Se, HPCs can confine higher loading of active materials compared to carbon materials with only micorpores or mesopores.

An early study by Professor Guo's group reported micro/mesoporous carbon spheres (HPCSs) via a hydrothermal method.[43] When used as host material in Li-Se battery, it shows an ultra-stable cycling stability after 1000 cycles.

After that, Lee *et al.*[36] synthesized ordered meso-/microporous carbon derived from silicon carbide (OM-SiC-CDC). Thanks to the dual pore size distribution and high Li salt concentration in electrolyte, the as prepared Se/OM-SiC-CDC cathode shows significantly better performance with high Se utilization than Se-activated carbons with similar physical properties.

Jiang and co-workers proposed a possible heating-melt process of Se in hierarchical porous carbon aerogels (HPCA) with micro-/mesopores and the discharge reaction model of the HPCA/Se composite cathode in **Figure 2.6(a)**.[35] In the heating melt diffusion process, Se nanoparticles (several nanometers) may first occupy the micropores followed by filling up of mesopres. During discharge, Se first react with Li to form polyselenide intermediates and then to the final products $Li_2Se$.

A typical morphology of hierarchical porous carbon is shown in **Figure 2.6(b)**, the authors prepared the macro-/microporous biochar-dervied carbon (MMPBC) via

carbonization of the inner spongy layer of pomelo pericarp and subsequent KOH activation.[37] An optimal mass ratio of carbonized sponge to KOH at 1:2 is determined to produce the integrated honeycomb-like carbon skeleton with a high specific surface area of 1539.4 $m^2 g^{-1}$. When used in Li-Se batteries, the MMPBC/Se cathode delivers a promising electrochemical behaviour over 300 cycles at 0.2 C. However, the cycling performance is still unsatisfied to meet its further applications. The unsatisfied cycling stability could be due to the improper ratio of micro-/macropores in MMPBC, which needs to be further investigated and optimized.

Metal-organic frameworks (MOFs) is another kind of materials that can produce hierarchical porous carbons. Liu *et al.*[38] prepared hierarchical porous carbon microcubes (HPCMCs) with micro-/mesopores from Zn/Ni-MOF2 precursors. As shown in **Figure 2.6(c)**, the microcube shape can be maintained after annealing and Se loading. No obvious bulk Se can be observed on the surface of HPCMCs/Se, indicating successful infiltration of Se into HPCMCs. In addition, the HPCMCs also show a hollow structure with irregular bubbles inside the carbon matrix, which will increase the ionic conductivity and mass transport As a result, the HPCMCs/Se achieves an ultrahigh initial discharge capacity and a reversible capacity of 425.2 mAh $g^{-1}$ over 100 cycles at 0.2 C.

In a recent work, Jin and co-workers successfully prepared hierarchical porous carbon nanosheets (PCNs) with fish-scale like surface morphology via carbonization of self-assembled MOFs.[44] With a large surface area of ~1571.4 $m^2 g^{-1}$, the PCNs still have a certain residual volume of micro-/mesopores after hosting a high content of 58 wt% Se. When used in Li-Se batteries, the PCNs/Se cathode maintains a high coulombic efficiency of 99.9% after 1000 cycles.

Inspired by the advantages of MOFs materials, MOF-derived N-doped hierarchical porous carbon polyhedrons anchored on crumpled graphene balls (NPC/CGBs) was

developed by Professor Kang's group in **Figure 2.6(e)**.[45] Considering ZIF-8 derived carbon only consists micorpores, they used mesoporous CGB, obtained via a spray pyrolysis method, as the substrate to growth of ZIF-8. Therefore, the NPC/CGBs can provide both mesopores from CGBs and micropores from ZIF-8 derived carbon. Therefore, Se can be effectively confined in the mico-/mesopores. Moreover, the porous CGBs matrix can serve as the 'bridge' among the individual NPC polyhedrons, offering fast electron/ion conductive pathways and electrolyte transport. They then further reported a novel porous carbon nanofibers host derived from carbonization of electrospun ZIF-8/PAN nanofibers for Li-Se batteries (**Figure 2.6(f)**).[46] During carbonization and KOH activation process, mesopores and micropores are introduced to form a bimodal porous nanofibers (BP-CNF). The final BP-CNF/Se composite can deliver 588 mA $h^{-1}$ after 300 cycles at 0.5 C with capacity retention of 79.2% from the 2$^{nd}$ cycle.

The bimodal porous structure (micro-/mesopores) can also be prepared via spray pyrolysis method. With an additional post-treatment of the spray-pyrolysis product, Park *et al.*[47] created a carbon microspheres with well-developed micro- and mesopores after vanadium oxide etching. More recently, Zheng *et al.* prepared a pomegranate-like porous carbon (PPC) matrix via a hydrothermal method and subsequent carbonization process.[48] The PPC matrix shows a combined pore distribution of mesopores (~2 nm) and micopores (0.56 nm).

Recently, Lei et al. prepared a novel hierarchical porous carbon via a one-step template route (**Figure 2.6(g)**).[49] In their work, different $SnO_2$@chitosan precursor ($SnO_2$@CIS-x, x=29/58/87) was prepared via a hydrothermal process. Then, the reduction of $SnO_2$@CIS-x was conducted with Se at 1000 ºC to generate the CISC-x and reduced gas product. Compared with CISC-00, all CISC-x samples have larger particle sizes and rougher surfaces.

Due to the removal of $SnO_2$ template in the reduction process, there appears cracks in CISC-x samples and large amount of micro-/mesopores with good connections. After loading with Se, the Se@CISC-x cathode delivers a high reversible capacity of 590.8 mAh $g^{-1}$ after 500 cycles at a high current density of 1 A $g^{-1}$.

Obviously, hierarchical porous carbons (HPCs) have superior properties compared to microporous carbons and mesoporous carbon. Developing HPCs with well-designed pore structure not only can host more active materials but also can supress the shuttle effect, enhance electron/ion conductivity and electrolyte transport through the carbon matrix.

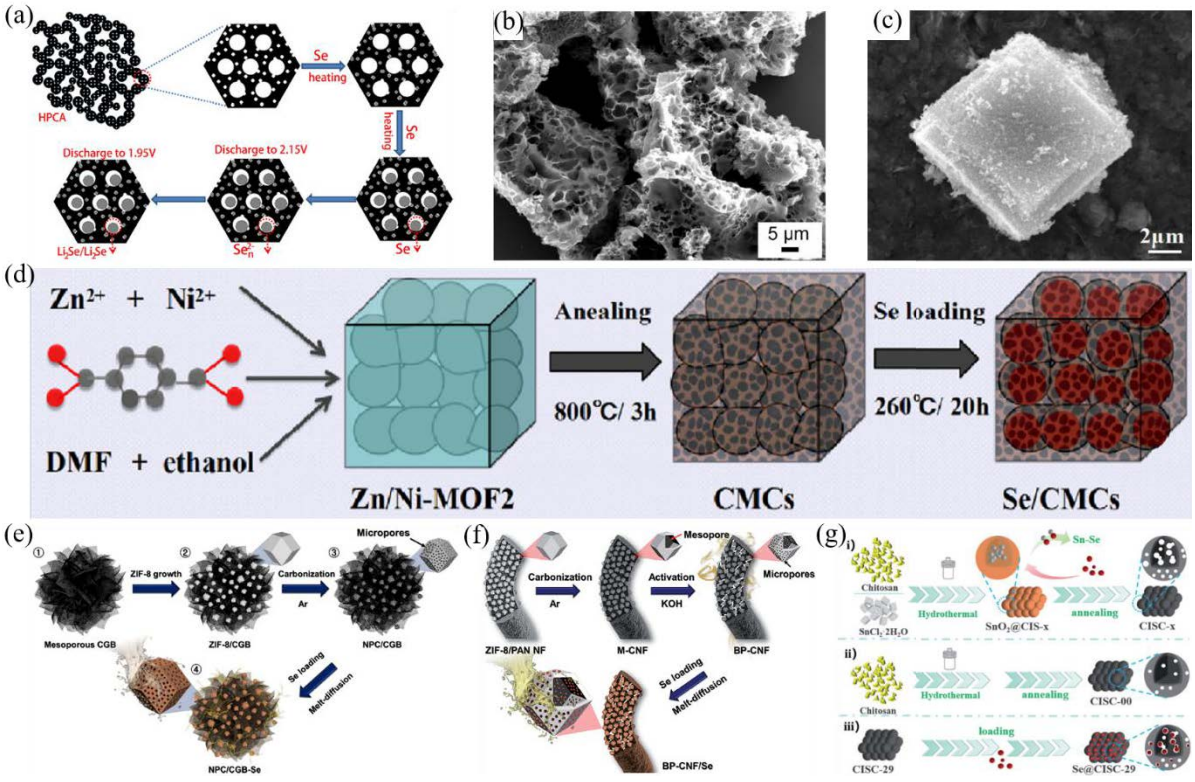


**Figure 2.6 (a)** Scheme of the possibility of the heating-melt process and the discharge reaction model of the HPCA/Se composite cathode,[35] **(b)** SEM images of pristine macro-/microporous biochar-dervied carbon (MMPBC),[37] **(c)** SEM images of the Se/HPCMCs composite, **(d)** schematic illustration of the preparation of Se/HPCMCs composites,[38] **(e)** formation mechanism of Se-nanoparticle-filled hierarchically porous NPC/CGB composite,[45]

**(f)** formation mechanism of bimodal porous nitrogen-doped carbon nanofiber homogeneously filled with chain-like Se,[46] **(g)** Schematic of the synthesis of composite materials and hierarchical porous carbons.[49]

### 2.4.2.4 Heteroatom-doped carbon hosts

Although conductive porous carbon materials have been proved to be effect matrix for hosting Se, the relatively weak physical interaction between carbon substrate and Se molecules/polyselenides cannot ensure a stable cycling performance over a long life. Introducing heteroatoms into the carbon matrix can induce chemical binding between the substrates and $Se_x$ species, which is more efficient to trap the polyselenide intermediates during cycling.

Nitrogen is one of the most common heteroatom as the doping element in carbon materials. **Table 2.1** summarized the first-principle calculated binding energies between N-doped carbon and $Li^+$/Se.[50] Nitrogen exists in the form of N-5, N-6 and N-Q in the carbonized polypyrrole. As shown in **Table 2.1**, the heteroatoms (both N and O) exhibit stronger interactions with Se and $Li^+$ in terms of higher binding energies than that of carbon atoms. The high affinities of heteroatoms to Se and Li ions can effectively suppress the shuttle effect and facilitate the reaction kinetics.

**Table 2.1** Binding energy of different atoms in carbonized polypyrrole (CP) with $Li^+$ and Se calculated by first principles[50]

| Structure | N-5 with Se | N-6 with Se | N-Q with Se | O-1 with Se | O-2 with Se | C with Se |
|---|---|---|---|---|---|---|
| Energy/eV | −5.47 | −2.54 | −3.29 | −4.36 | −2.53 | −2.25 |
| Structure | N-5 with $Li^+$ | N-6 with $Li^+$ | N-Q with $Li^+$ | O-1 with $Li^+$ | O-2 with $Li^+$ | C with $Li^+$ |
| Energy/eV | −3.92 | −4.32 | −4.17 | −4.2 | −4.32 | −3.51 |

Jiang and co-workers also prepared N-doped porous carbon (NPC) via carbonization of polypyrrole.[51] XPS results show that N doping enhances the affinities between Se and the

carbon host. In addition, oxygen in the form of Se-O bonds also help to improve the cycling stability. As a result, the Se/NPC cathode material can deliver an outstanding cycling performance after 1600 cycles at a high current density of 2 C without obvious capacity decay.

At almost the same time, Li *et al.* prepared N-doped carbon sponges (NC) via carbonization of rod-like Al-MOF under Ar/$NH_3$ gas at 800 ºC for 3 h.[52] The obtained NC sponges maintain a cuboid, rod-like structure with hierarchical interconnected porous carbon layers. After loading with Se in **Figure 2.7 (a)**, no bulk Se can be observed, indicating the successful confinement of Se in NC sponges. To study the N doping on the electrochemical performance of Li-Se batteries, the author also prepared carbon sponges loaded with Se without nitrogen doping (C/Se). The cycling performance of Li-Se batteries with different cathode materials is displayed in **Figure 2.7(b)**, it is obviously that NC/Se composites exhibit much better electrochemical performance than C/Se composites in Li-Se batteries. However, the NC/Se cathode with 60 wt% content of Se still suffer from severe capacity decay after 40 cycles, which might be due to the insufficient confinement of high Se loading within the NC sponges.

Zn-glutamate MOF is also used to prepare N-doped hierarchically radical-structured microporous carbon (N-HRMC) without $NH_3$ treatment due to the N source in the reactant (sodium 2-aminopentanedioate).[53] The nitrogen doping strongly enhances the electrical conductivity of the cathode materials and shows stronger affinities to $Na_2Se$, as confirmed by DFT calculations. As a result, the Se/N-HRMC cathode with a high Se loading of 62 wt% can deliver 612 mAh $g^{-1}$ at 0.2 C for 200 cycles and almost ~100% capacity retention at 0.5 C from the $20^{th}$ cycle to 500 cycles.

Another work reported by Professor Jin's group also achieved high cycling stability with 50 wt% Se loading.[54] In their work, they prepared N-doped carbon scaffolds (NCSs) via a bottom-up solution phase method. The Se/NCSs cathode delivers superior cycling stability and rate capability compared to that of Se/pristine carbon scaffolds. Although tremendous doping strategies have been developed to improve the electric properties of the cathodes and chemical adsorption of the substrates to polyselenides, the long-life performance over 1000 cycles is still far from satisfactory for its wide applications.

Beyond the single element doping strategies, Zhao *et al.* developed heteroatoms dual-doped hierarchical porous carbon (HDHPC) as the host for durable Li-Se and Na-Se batteries.[8] As shown in **Figure 2.7(c)**, HDHPC can be obtained by directly carbonization of poly dopamine (PDA) and KOH. The as-prepared HDHPC possess a hierarchical porous structure with interconnected macro/meso/micropores, which benefits the electrolyte penetration, bears the volume change of Se and traps the polyselenides during cycling. In addition, the heteroatom dopants (N and O) in the HDHPC matrix provide strong chemical interaction between the carbon substrate and polyselenides. With the synergistic effect of hierarchical porous structure and N, O dual-doping, the Se/HDHPC cathode shows outperformed electrochemical performance in both Li-Se and Na-Se batteries compared to previous work. When used as cathode material in Li-Se battery, Se/HDHPC composite can deliver an extremely low capacity decay of 0.0074% per cycle over 1500 cycles. For the Na-Se battery, Se/HDHPC cathode can deliver a reversible capacity of 402 mAh $g^{-1}$ after 500 cycles at 0.5 C. This study also confirms that N, O dual-doped carbon matrix has stronger binding energy compared to that of pristine carbon matrix, pyrrolic-N doped carbon and kenotic-O doped carbon by DFT calculations, demonstrating the advantages of heteroatoms dual-doped carbon for Li-Se batteries.

Inspired by this work, Professor Yu's group reported a novel 3D flexible Se/C composite cathode by infiltration of Se in the carbon nanotube (CNT) interwoven N, O dual-doped porous carbon nanosheets (Se@NOPC-CNT) (**Figure 2.7(d, e)**).[55] When used as cathode materials in Na-Se battery, Se@NOPC-CNT composite exhibits an outstanding cycling performance with a reversible capacity of 400 mAh $g^{-1}$ at 1 A $g^{-1}$ after 2000 cycles, which is one of the best performance. Notably, this cathode also achieves promising cycling stability with 335 mAh $g^{-1}$ at 0.8 A $g^{-1}$ after 700 cycles for potassium-selenium battery which is a more challenging energy storage system.

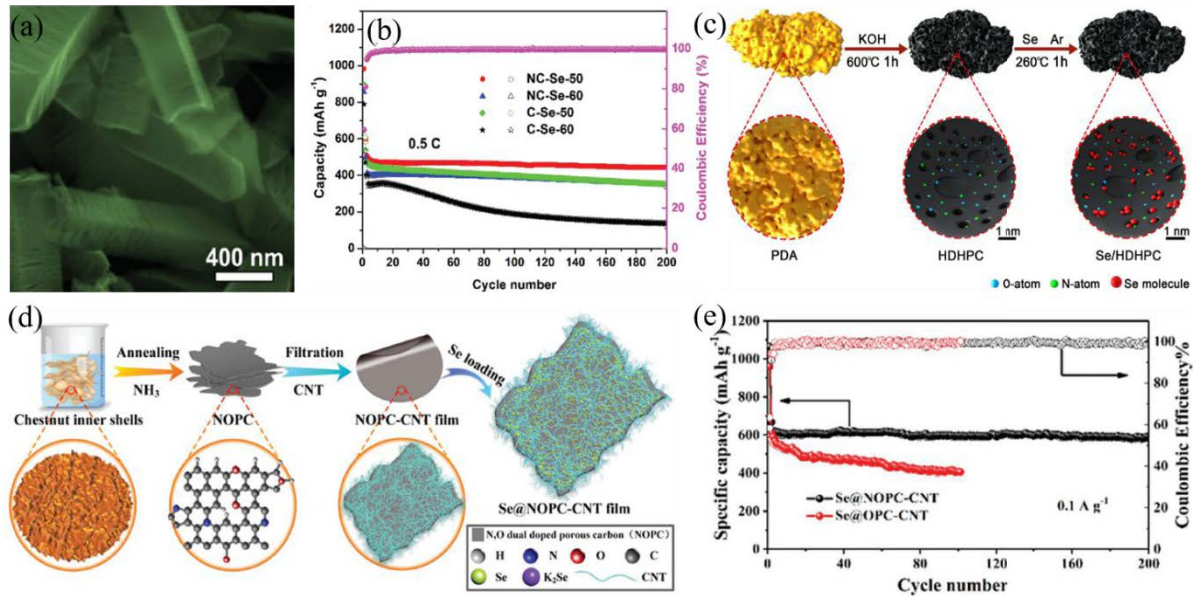


**Figure 2.7 (a)** FESEM images of the NCS/Se-50 composites. **(b)** Cycling performances of NCS/Se and CS/Se composites at 0.5 C, and pink circles show the Coulombic efficiency of NCS/Se-50.[52] **(c)** Schematic illustration of the synthesis process of Se/HDHPC composite.[8] **(d)** Synthesis procedure of the Se@NOPC-CNT film electrode. **(e)** Comparison of cycling performance between Se@NOPC-CNT and Se@OPC-CNT at 0.1 A $g^{-1}$.[55]

## 2.4.3 Coating strategies of cathode materials

Cathode materials coated with a thin protective layer show superior physical and electrochemical performances. For example, coating $Li_{1.17}Ni_{0.17}Co_{0.17}Mn_{0.5}O_2$ cathode with a hybrid surface protection layer composed of $Mg^{2+}$ pillar and Li-Mg-$PO_4$ layer can effectively inhibit the undesired side reactions between the cathode and electrolyte, leading to enhanced structural stability of the Li-rich cathode material.[56] Zhang *et al.* suppressed the severe surface lattice oxygen release in Li-rich cathode materials via a heterostructured spinel $Li_4Mn_5O_{12}$ coating method.[57] Recently, Jamil and co-workers coated the Ni-rich layered oxide cathode material ($LiNi_{0.87}Co_{0.1}Al_{0.03}O_2$) with an amorphous Li ion conductor $Li_2O$-$BPO_4$ (LBP). The LBP coating layer can not only facilitate the $Li^+$ transfer at the solid-electrolyte interface, but also protect the cathode materials from corrosion.

Coating with a protective layer is also a commonly used method in Li-S batteries. So far, tremendous effects have been made to develop novel coating materials for Li-S batteries.[58-59] The protective coating layer provides additional barriers to trap the polysulfides and thus inhibit the shuttle effect.

Inspired by the state of the art works in these battery systems, coating strategies have also been proved to be effective in recent studies for Li-Se and Na-Se batteries.[60-62] Reduced graphene oxide (rGO) was initially employed as a wrapping layer on Se nanoparticles (Se@rGO).[63] The Se@rGO cathode with a high Se content of 80 wt% exhibit superior excellent electrochemical performance compared to that of bare Se composite. Beyond the rGO coating,

Wang *et al.* prepared a polyaniline (PANI)-coated Se/C composite wrapped by reduced graphene oxide nanosheet.[64] In their work, PANI was first coated on the Se/C nanocomposite

with a positively charged surface. Then, the negatively charged GO can be uniformly self-assembled with PANI@Se/C. The final product (rGO@PANI@Se/C) will be obtained after a reduction process. It shows that the double layer conductive coating (PANI & rGO) can efficiently suppress the shuttle effect, improve the utilization of Se and electronic conductivity of the cathode. As a result, the rGO@PANI@Se/C delivers a high capacity of 528.6 mAh $g^{-1}$ at 2 C after 500 cycles. However, the preparation of the double-layer coating is complicated and it inevitably decrease the overall content of active material (Se) in the cathode composites.

Conductive polymer itself can be solely used as a coating layer with outstanding properties. Mukkabla and co-workers used polycarbazole (PCZ) as the conducting polymer coating layer on Se@conical carbon nanofibers (Se@CCNFs). Compared to the Se@CCNFs without PCZ coating, Se@CCNFs-PCZ can deliver an extremely high reversible capacity of 640 mAh $g^{-1}$ after 100 cycles at 0.1 C, which is close to its theoretical capacity of 675 mAh $g^{-1}$. The superior electrochemical performance is enhanced by the PCZ coating layer which not only provides a diffusion barrier to polyselenides shuttling, but also offers a favourable solid-electrolyte interface with fast electron/ion transport.

Although coating with graphene (rGO) and conductive polymer can efficiently enhance the electrochemical performance of Se cathode, however, the coating process usually requires a complex multistep *ex situ* or *in situ* preparation of the cathode composites. A more optimized way is to develop the facile, cost-effective "in batteria electrochemical polymerization" method, which forms a conductive layer on the Se/C composite spontaneously with the applying of an electrochemical signal. Most recently, Lee et al. choose aniline as monomer for the "in batteria electrochemical polymerization" process.[65] As we know, polyaniline (PANI) possess a high electrical conductivity and the positively

charged amino-containing surface groups can provide strong affinities to the polyselenides, which is an idea polymer candidate. **Figure 2.8(a-c)** shows the schematic of in batteria electrochemical polymerization of aniline on a Se/C cathode. During which, the aniline monomers anchor on the Se/C electrode surface upon a specific current is applied, forming the initial PANI (leucoemeraldine) on the Se/C surface in **Figure 2.8(b)**. Further oxidation can convert the initial PANI into the conductive emeraldine PANI (**Figure 2.8(c**) which is more preferable for fast electron/ion transport. Unlike the *ex situ* and *in situ* polymerization method that yields irregular PANI layer with nanoparticles, the "in batteria electrochemical polymerization" treatment enables ultrathin uniform coating (≤ 10 nm) without agglomeration. Due to the uniform coating of PANI layer and its superior conductive property, the ET-Se/C/aniline cathode exhibits an outstanding cycling perfromence, which retains 40% higher capacity than that of EC-Se/C in **Figure 2.8(e)**. UV-vis spectroscopy also confirms the effective trapping of polyselenides by the PANI layer at the discharged state of the cathode in **Figure 2.8(d)**.

Besides graphene (rGO) and conductvie polymer, metal oxides and metal selenide can also be coated onto Se/C surface to provide better electrochemical performance.[6, 66-67] For example, *Ma et al.* prepared $Al_2O_3$-coated Se/porous N-doped carbon nanofibers composite (Se/PCNFs-$Al_2O_3$) via the advanced atomic layer deposition method (ALD), shown in **Figure 2.8(f)**.[6] The thickness of $Al_2O_3$ layer can be precisely controlled by adjusting ALD cycle numbers, which can achieve as low as 1.5-5 nm in **Figure 2.8(g)**. The ultrathin layer $Al_2O_3$ will not decrease the overall Se content in the cathode while significantly enhance the electrode property in terms of high mechanical strength and high cycling performance. This work demonstrate that ALD technique is a promising method to enhance the Na-Se battery performance, which might also be applicable to other energy storage systems.

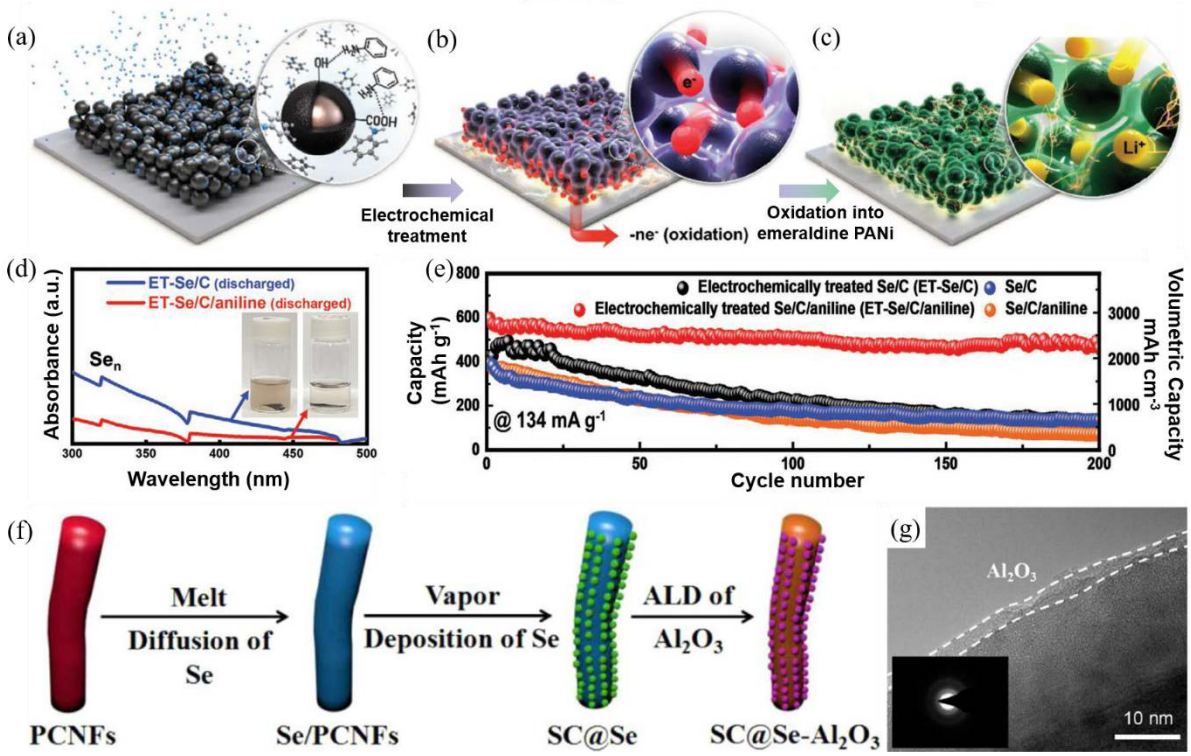


**Figure 2.8** Schematic image of in batteria electrochemical polymerization of aniline on a Se/C cathode: **(a)** Adsorption of aniline, **(b)** electrochemical polymerization of aniline, and **(c)** a protective ion/electron conducting PANi layer on the Se/C particles (electrochemically treated Se/C/aniline). **(d)** Images (insets) of electrodes (the first discharged electrodes) soaked in the electrolytes (1.0 m $LiPF_6$ in EC/DEC) and corresponding UV-vis spectra of ET-Se/C and ET-Se/C/aniline. **(e)** Cyclic performances (discharge capacities-cycle number graphs) of ET-Se/C, ET-Se/C/aniline, Se/C/aniline, and Se/C. The galvanostatic charge-discharge tests were conducted in the range of 2.85-1.0 V $Li^+/Li$ at 134 mA $g^{-1}$ for 200 cycles.[65] **(f)** Schematic illustration of the preparation process for SC@ Se-xAl2O3 composites. **(g)** HRTEM image of the SC@Se-25$Al_2O_3$ composite.[6]

## 2.5 Development of separators and interlayers for Li-Se and Na-Se batteries

In addition to the tremendous efforts in Se cathode materials, it is also efficient to block the polyselenides shuttling on its way across the separator.[68] So far, several materials have been employed to modify the separator or been used to fabricate the interlayer, such as graphene,[68] metal oxide ($WO_3$),[69] covalent organic frameworks (COFs),[70-71] and carbonized polyacrylonitrile (PAN) nanofiber.[72] Separators and interlayers are preferable to be designed as thin and light as possible because the thin and light separator/interlayer accounts for negligible volume and mass proportion in the whole battery configuration. The modified separator/interlayer should also possess high blocking efficiency to the polyselenides shuttling either by physical barrier, chemical binding or electrostatic repulsion/attraction.

Applying a physical diffusion barrier between the cathode and separator can effectively suppress the shuttle effect. Si and co-workers prepared a covalent organic framework via the polymerization of 2,5-Dimethoxy-1,4-Dicarboxaldehyde and Tetrakis(4-aminophenyl)ethane (DMTA-COF).[70] The as-synthesized DMTA-COF have a high surface area of 300 $m^2/g$ with a pore size of 0.56 nm which is much smaller than that of polyselenides ($Li_2Se_n$, $4<n\leq8$). Therefore, the polyselenides is effectively confined on the cathode side without inhibiting the Li ion transport. In the same year, Yang *et al.* also prepared a COF coated separator based on 1,3,5-tri(4-aminophenyl)benzene (TPB), 2,5-dimethoxyterephthalaldehyde (DMTP), denoted as TPB-DMTP-COF, for Li-$SeS_2$ battery.[71] TPB-DMTP-COF can selectively adsorb lithium bis(trifluoromethanesulfonyl)imide (LiTFSI) in the electrolyte through hydrogen boding, leading to the accumulation of LiTFSI in the TPB-DMTP-COF channels and a narrowed channel pore size. The rich LiTFSI and narrowed channel will not only block the intermediates (polyselenides and polysulfides) shuttling, but also facilitate Li ion transport

(**Figure 2.9(a)**). **Figure 2.9(b)** shows that the electrolyte in the right-hand side still remains colourless after 48 h permeation test, which confirms the blocking effects of TPB-DMTP-COF separator. As expected, the TPB-DMTP-COF separator fabricated battery achieved a long lifespan of 800 cycles under a high areal loading of 4 mg $cm^{-2}$.

Besides the sieve effect by tuning the size of transport pathway, a more facile method is to apply a porous carbon onto the separators. Wang et al. prepared a bind-free, self-interwoven carbon nanofiber-Se composite (CNF@Se) cathode combined with a light-weight porous carbon-coated glass fiber separator for Na-Se batteries.[73] The carbon-coated separator with a small mass loading of 0.3 mg $cm^{-2}$ was prepared via a facile tape casting method in **Figure 2.9(c, d)**. With this carbon-coated separator, the shuttle effect can be significantly suppressed and long static (shelf-life) performance is also investigated by experimental (**Figure 2.9(e)**) and density-functional theory (DFT) calculations. With the combination of CNF@Se and carbon-coated separator, the battery with a high Se area mass loading of 4.4 mg $cm^{-2}$ delivers high reversible capacity of 599 mAh $g^{-1}$ at 0.1 C and 382 mAh $g^{-1}$ at 5 C.

Therefore, separator modification and interlayer configuration plays an important role in suppressing the shuttle effect and maintain the long lifespan capacity.

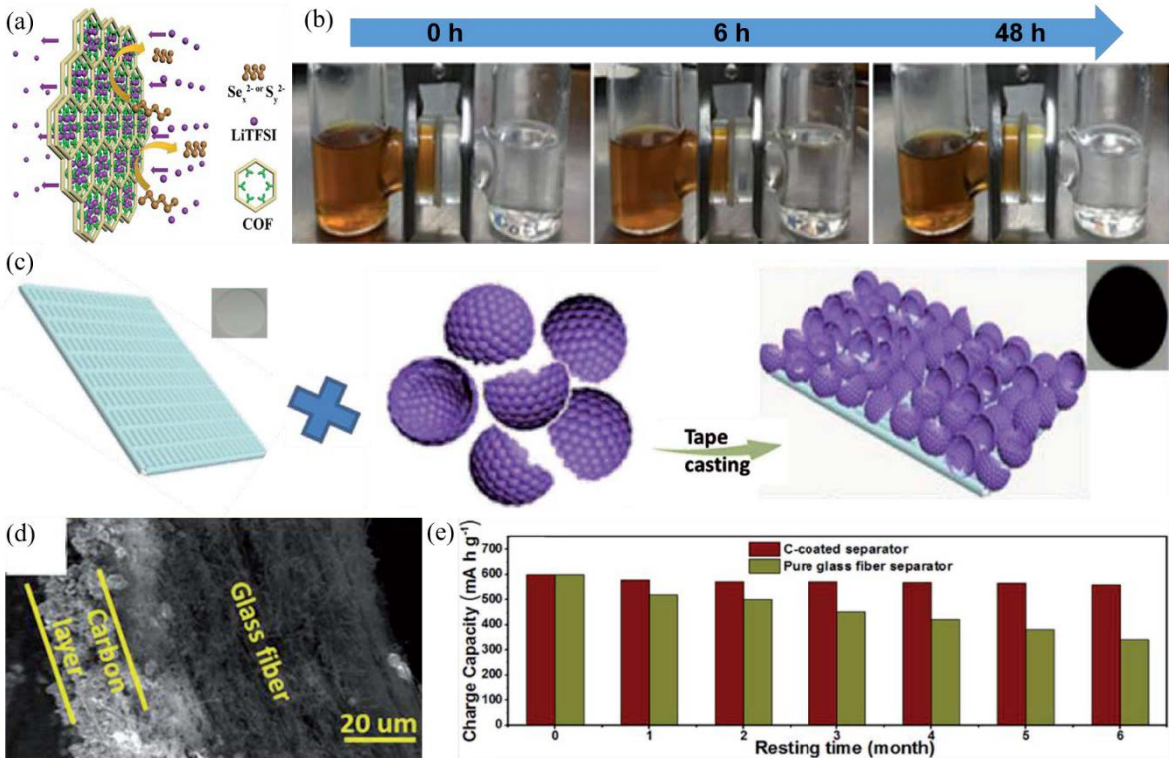


**Figure 2.9 (a)** Schematic showing the bifunctional TPB-DMTP-COF separator coating materials that can selectively block the transport of polysulfides/polyselenides while improving lithium ion conductivity, leading to high performance lithium–selenium sulfide batteries. **(b)** The sieving effect experiment: H-tube permeation test with Celgard separator coated with TPB-DMTP-COF separator.[71] **(c)** Schematic illustration of the synthesis process of the light-weight carbon-coated separator. **(d)** FESEM images of carbon-coated glass fiber cross-sections. **(e)** Static electrochemical stability: charge capacity retention of the cells after storing for various times.[73]

## 2.6 Summary

Great efforts have been made to achieve high performance Li-Se and Na-Se batteries. Cathode materials preparations and separator/interlayer configurations have shown significant influences on the final battery performances. Besides, the mechanisms of the Se-based batteries are far from fully understanding. Inspired by the above literature analysis, this

project focuses on preparing novel cathode materials via applying hierarchical porous carbon, doping strategies and conductively polymer coating in Chapter 4. Additionally, an interface engineering strategy is also proposed by preparing a MXene composite separator for both Na-Se and Li-Se batteries in Chapter 5. The mechanisms of Li-Se and Na-Se batteries are also studied in Chapter 4 and 5.

## 2.7 References


1. Pang, Q.; Liang, X.; Kwok, C. Y.; Nazar, L. F., Advances in lithium–sulfur batteries based on multifunctional cathodes and electrolytes. *Nature Energy* **2016,** *1* (9).

2. Zhang, F.; Guo, X.; Xiong, P.; Zhang, J.; Song, J.; Yan, K.; Gao, X.; Liu, H.; Wang, G., Interface Engineering of MXene Composite Separator for High-Performance Li–Se and Na–Se Batteries. *Advanced Energy Materials* **2020,** *10* (20).

3. Jin, J.; Tian, X.; Srikanth, N.; Kong, L. B.; Zhou, K., Advances and challenges of nanostructured electrodes for Li–Se batteries. *Journal of Materials Chemistry A* **2017,** *5* (21), 10110-10126.

4. Li, Q.; Liu, H.; Yao, Z.; Cheng, J.; Li, T.; Li, Y.; Wolverton, C.; Wu, J.; Dravid, V. P., Electrochemistry of Selenium with Sodium and Lithium: Kinetics and Reaction Mechanism. *ACS Nano* **2016,** *10* (9), 8788-95.

5. Zhang, F.; Xiong, P.; Guo, X.; Zhang, J.; Yang, W.; Wu, W.; Liu, H.; Wang, G., A nitrogen, sulphur dual-doped hierarchical porous carbon with interconnected conductive polyaniline coating for high-performance sodium-selenium batteries. *Energy Storage Materials* **2019,** *19*, 251-260.

6. Ma, D.; Li, Y.; Yang, J.; Mi, H.; Luo, S.; Deng, L.; Yan, C.; Zhang, P.; Lin, Z.; Ren, X.; Li, J.; Zhang, H., Atomic layer deposition-enabled ultrastable freestanding carbon-selenium cathodes with high mass loading for sodium-selenium battery. *Nano Energy* **2018,** *43*, 317-325.

7. Zhao, C.; Xu, L.; Hu, Z.; Qiu, S. e.; Liu, K., Facile synthesis of selenium/potassium tartrate derived porous carbon composite as an advanced Li–Se battery cathode. *RSC Advances* **2016,** *6* (53), 47486-47490.

8. Zhao, X.; Yin, L.; Zhang, T.; Zhang, M.; Fang, Z.; Wang, C.; Wei, Y.; Chen, G.; Zhang, D.; Sun, Z.; Li, F., Heteroatoms dual-doped hierarchical porous carbon-selenium composite for durable Li–Se and Na–Se batteries. *Nano Energy* **2018,** *49*, 137-146.

9. Zhao, J.; Guo, W.; Fu, Y., Performance enhancement of Li–Se batteries by manipulating redox reactions pathway. *Materials Today Energy* **2020,** *17*.

10. Abouimrane, A.; Dambournet, D.; Chapman, K. W.; Chupas, P. J.; Weng, W.; Amine, K., A new class of lithium and sodium rechargeable batteries based on selenium and selenium-sulfur as a positive electrode. *J Am Chem Soc* **2012,** *134* (10), 4505-8.

11. Cui, Y.; Abouimrane, A.; Lu, J.; Bolin, T.; Ren, Y.; Weng, W.; Sun, C.; Maroni, V. A.; Heald, S. M.; Amine, K., (De)lithiation mechanism of Li/SeS(x) (x = 0-7) batteries determined by in situ synchrotron X-ray diffraction and X-ray absorption spectroscopy. *J Am Chem Soc* **2013,** *135* (21), 8047-56.

12. Zhou, X.; Gao, P.; Sun, S.; Bao, D.; Wang, Y.; Li, X.; Wu, T.; Chen, Y.; Yang, P., Amorphous, Crystalline and Crystalline/Amorphous Selenium Nanowires and Their Different (De)Lithiation Mechanisms. *Chemistry of Materials* **2015,** *27* (19), 6730-6736.

13. Xin, S.; Yu, L.; You, Y.; Cong, H. P.; Yin, Y. X.; Du, X. L.; Guo, Y. G.; Yu, S. H.; Cui, Y.; Goodenough, J. B., The Electrochemistry with Lithium versus Sodium of Selenium Confined To Slit Micropores in Carbon. *Nano Lett* **2016,** *16* (7), 4560-8.

14. Perras, F. A.; Hwang, S.; Wang, Y.; Self, E. C.; Liu, P.; Biswas, R.; Nagarajan, S.; Pham, V. H.; Xu, Y.; Boscoboinik, J. A.; Su, D.; Nanda, J.; Pruski, M.; Mitlin, D., Site-Specific Sodiation Mechanisms of Selenium in Microporous Carbon Host. *Nano Lett* **2020,** *20* (2), 918-928.

15. Aboonasr Shiraz, M. H.; Zhu, H.; Liu, Y.; Sun, X.; Liu, J., Activation-free synthesis of microporous carbon from polyvinylidene fluoride as host materials for lithium-selenium batteries. *Journal of Power Sources* **2019,** *438*.

16. Li, X.; Liang, J.; Hou, Z.; Zhang, W.; Wang, Y.; Zhu, Y.; Qian, Y., A New Salt-Baked Approach for Confining Selenium in Metal Complex-Derived Porous Carbon with Superior Lithium Storage Properties. *Advanced Functional Materials* **2015,** *25* (32), 5229-5238.

17. Yang, X.; Wang, H.; Yu, D. Y. W.; Rogach, A. L., Vacuum Calcination Induced Conversion of Selenium/Carbon Wires to Tubes for High-Performance Sodium-Selenium Batteries. *Advanced Functional Materials* **2018,** *28* (8).

18. Wu, F.; Lee, J. T.; Xiao, Y.; Yushin, G., Nanostructured Li2Se cathodes for high performance lithium-selenium batteries. *Nano Energy* **2016,** *27*, 238-246.

19. Wang, X.; Zhang, Z.; Qu, Y.; Wang, G.; Lai, Y.; Li, J., Solution-based synthesis of multi-walled carbon nanotube/selenium composites for high performance lithium–selenium battery. *Journal of Power Sources* **2015,** *287*, 247-252.

20. Wang, H.; Li, S.; Chen, Z.; Liu, H. K.; Guo, Z., A novel type of one-dimensional organic selenium-containing fiber with superior performance for lithium–selenium and sodium–selenium batteries. *RSC Adv.* **2014,** *4* (106), 61673-61678.

21. Guo, J.; Wen, Z.; Wang, Q.; Jin, J.; Ma, G., A conductive selenized polyacrylonitrile cathode material for re-chargeable lithium batteries with long cycle life. *Journal of Materials Chemistry A* **2015,** *3* (39), 19815-19821.

22. Luo, C.; Wang, J.; Suo, L.; Mao, J.; Fan, X.; Wang, C., In situ formed carbon bonded and encapsulated selenium composites for Li–Se and Na–Se batteries. *Journal of Materials Chemistry A* **2015,** *3* (2), 555-561.

23. Wang, J.; Yang, J.; Xie, J.; Xu, N., A Novel Conductive Polymer–Sulfur Composite Cathode Material for Rechargeable Lithium Batteries. *Advanced Materials* **2002,** *14* (13-14), 963-965.

24. Mukkabla, R.; Deshagani, S.; Deepa, M.; Shivaprasad, S. M.; Ghosal, P., Carbon black free Selenium/CTAB decorated carbon nanotubes composite with high selenium content for Li-Se batteries. *Electrochimica Acta* **2018,** *283*, 63-74.

25. Zhang, H.; Jia, D.; Yang, Z.; Yu, F.; Su, Y.; Wang, D.; Shen, Q., Alkaline lignin derived porous carbon as an efficient scaffold for lithium-selenium battery cathode. *Carbon* **2017,** *122*, 547-555.

26. Liu, Y.; Si, L.; Zhou, X.; Liu, X.; Xu, Y.; Bao, J.; Dai, Z., A selenium-confined microporous carbon cathode for ultrastable lithium–selenium batteries. *J. Mater. Chem. A* **2014,** *2* (42), 17735-17739.

27. Jia, D.; Yang, Z.; Zhang, H.; Liu, F.; Shen, Q., High performance of selenium cathode by

encapsulating selenium into the micropores of chitosan-derived porous carbon framework. *Journal of Alloys and Compounds* **2018,** *746*, 27-35.

28. Feng, N.; Xiang, K.; Xiao, L.; Chen, W.; Zhu, Y.; Liao, H.; Chen, H., Se/CNTs microspheres as improved performance for cathodes in Li-Se batteries. *Journal of Alloys and Compounds* **2019,** *786*, 537-543.

29. Lei, Z.; Lei, Y.; Liang, X.; Yang, L.; Feng, J., High stable rate cycling performances of microporous carbon spheres/selenium composite (MPCS/Se) cathode as lithium–selenium battery. *Journal of Power Sources* **2020,** *473*.

30. Wang, X.; Tan, Y.; Liu, Z.; Fan, Y.; Li, M.; Younus, H. A.; Duan, J.; Deng, H.; Zhang, S., New Insight into the Confinement Effect of Microporous Carbon in Li/Se Battery Chemistry: A Cathode with Enhanced Conductivity. *Small* **2020,** *16* (17), e2000266.

31. Luo, C.; Xu, Y.; Zhu, Y.; Liu, Y.; Zheng, S.; Liu, Y.; Langrock, A.; Wang, C., Selenium@Mesoporous Carbon Composite with Superior Lithium and Sodium Storage Capacity. *ACS Nano* **2013,** *7* (9), 8003-8010.

32. Yang, C. P.; Xin, S.; Yin, Y. X.; Ye, H.; Zhang, J.; Guo, Y. G., An advanced selenium-carbon cathode for rechargeable lithium-selenium batteries. *Angew Chem Int Ed Engl* **2013,** *52* (32), 8363-7.

33. Lai, Y.; Gan, Y.; Zhang, Z.; Chen, W.; Li, J., Metal-organic frameworks-derived mesoporous carbon for high performance lithium–selenium battery. *Electrochimica Acta* **2014,** *146*, 134-141.

34. Liu, T.; Zhang, Y.; Hou, J.; Lu, S.; Jiang, J.; Xu, M., High performance mesoporous C@Se composite cathodes derived from Ni-based MOFs for Li–Se batteries. *RSC*

*Advances* **2015,** *5* (102), 84038-84043.

35. Jiang, S.; Zhang, Z.; Lai, Y.; Qu, Y.; Wang, X.; Li, J., Selenium encapsulated into 3D interconnected hierarchical porous carbon aerogels for lithium–selenium batteries with high rate performance and cycling stability. *Journal of Power Sources* **2014,** *267*, 394-404.

36. Lee, J. T.; Kim, H.; Oschatz, M.; Lee, D.-C.; Wu, F.; Lin, H.-T.; Zdyrko, B.; Cho, W. I.; Kaskel, S.; Yushin, G., Micro- and Mesoporous Carbide-Derived Carbon-Selenium Cathodes for High-Performance Lithium Selenium Batteries. *Advanced Energy Materials* **2015,** *5* (1).

37. Zhang, H.; Yu, F.; Kang, W.; Shen, Q., Encapsulating selenium into macro-/micro-porous biochar-based framework for high-performance lithium-selenium batteries. *Carbon* **2015,** *95*, 354-363.

38. Liu, T.; Jia, M.; Zhang, Y.; Han, J.; Li, Y.; Bao, S.; Liu, D.; Jiang, J.; Xu, M., Confined selenium within metal-organic frameworks derived porous carbon microcubes as cathode for rechargeable lithium–selenium batteries. *Journal of Power Sources* **2017,** *341*, 53-59.

39. Xu, Q.; Liu, H.; Du, W.; Zhan, R.; Hu, L.; Bao, S.; Dai, C.; Liu, F.; Xu, M., Metal-organic complex derived hierarchical porous carbon as host matrix for rechargeable Na-Se batteries. *Electrochimica Acta* **2018,** *276*, 21-27.

40. Kim, J. K.; Kang, Y. C., Encapsulation of Se into Hierarchically Porous Carbon Microspheres with Optimized Pore Structure for Advanced Na-Se and K-Se Batteries. *ACS Nano* **2020,** *14* (10), 13203-13216.

41. Sun, J.; Du, Z.; Liu, Y.; Ai, W.; Wang, K.; Wang, T.; Du, H.; Liu, L.; Huang, W., State-

Of-The-Art and Future Challenges in High Energy Lithium-Selenium Batteries. *Adv Mater* **2021**, e2003845.

42. Zeng, L.; Zeng, W.; Jiang, Y.; Wei, X.; Li, W.; Yang, C.; Zhu, Y.; Yu, Y., A Flexible Porous Carbon Nanofibers-Selenium Cathode with Superior Electrochemical Performance for Both Li-Se and Na-Se Batteries. *Advanced Energy Materials* **2015,** *5* (4).

43. Ye, H.; Yin, Y.-X.; Zhang, S.-F.; Guo, Y.-G., Advanced Se–C nanocomposites: a bifunctional electrode material for both Li–Se and Li-ion batteries. *Journal of Materials Chemistry A* **2014,** *2* (33).

44. Jin, W.-w.; Li, H.-j.; Zou, J.-z.; Inguva, S.; Zhang, Q.; Zeng, S.-z.; Xu, G.-z.; Zeng, X.-r., Metal organic framework-derived carbon nanosheets with fish-scale surface morphology as cathode materials for lithium–selenium batteries. *Journal of Alloys and Compounds* **2020,** *820*.

45. Park, S. K.; Park, J. S.; Kang, Y. C., Metal-Organic-Framework-Derived N-Doped Hierarchically Porous Carbon Polyhedrons Anchored on Crumpled Graphene Balls as Efficient Selenium Hosts for High-Performance Lithium-Selenium Batteries. *ACS Appl Mater Interfaces* **2018,** *10* (19), 16531-16540.

46. Park, S.-K.; Park, J.-S.; Kang, Y. C., Selenium-infiltrated metal–organic framework-derived porous carbon nanofibers comprising interconnected bimodal pores for Li–Se batteries with high capacity and rate performance. *Journal of Materials Chemistry A* **2018,** *6* (3), 1028-1036.

47. Park, G. D.; Kim, J. H.; Lee, J.-K.; Chan Kang, Y., Carbon microspheres with well-developed micro- and mesopores as excellent selenium host materials for lithium–selenium batteries with superior performances. *Journal of Materials Chemistry A* **2018,** *6*

(43), 21410-21418.

48. Zheng, Z.; Su, Q.; Xu, H.; Zhang, Q.; Ye, H.; Wang, Z., A pomegranate-like porous carbon nanomaterial as selenium host for stable lithium-selenium batteries. *Materials Letters* **2019,** *244*, 134-137.

49. Lei, Y.; Liang, X.; Yang, L.; Jiang, P.; Lei, Z.; Wu, S.; Feng, J., Novel hierarchical porous carbon prepared by a one-step template route for electric double layer capacitors and Li–Se battery devices. *Journal of Materials Chemistry A* **2020,** *8* (8), 4376-4385.

50. Yi, Z.; Yuan, L.; Sun, D.; Li, Z.; Wu, C.; Yang, W.; Wen, Y.; Shan, B.; Huang, Y., High-performance lithium–selenium batteries promoted by heteroatom-doped microporous carbon. *Journal of Materials Chemistry A* **2015,** *3* (6), 3059-3065.

51. Jiang, Y.; Ma, X.; Feng, J.; Xiong, S., Selenium in nitrogen-doped microporous carbon spheres for high-performance lithium–selenium batteries. *Journal of Materials Chemistry A* **2015,** *3* (8), 4539-4546.

52. Li, Z.; Yin, L., MOF-derived, N-doped, hierarchically porous carbon sponges as immobilizers to confine selenium as cathodes for Li-Se batteries with superior storage capacity and perfect cycling stability. *Nanoscale* **2015,** *7* (21), 9597-606.

53. Dong, W.; Chen, H.; Xia, F.; Yu, W.; Song, J.; Wu, S.; Deng, Z.; Hu, Z.-Y.; Hasan, T.; Li, Y.; Wang, H.; Chen, L.; Su, B.-L., Selenium clusters in Zn-glutamate MOF derived nitrogen-doped hierarchically radial-structured microporous carbon for advanced rechargeable Na–Se batteries. *Journal of Materials Chemistry A* **2018,** *6* (45), 22790-22797.

54. Lv, H.; Chen, R.; Wang, X.; Hu, Y.; Wang, Y.; Chen, T.; Ma, L.; Zhu, G.; Liang, J.; Tie,

Z.; Liu, J.; Jin, Z., High-Performance Li-Se Batteries Enabled by Selenium Storage in Bottom-Up Synthesized Nitrogen-Doped Carbon Scaffolds. *ACS Appl Mater Interfaces* **2017,** *9* (30), 25232-25238.

55. Yao, Y.; Chen, M.; Xu, R.; Zeng, S.; Yang, H.; Ye, S.; Liu, F.; Wu, X.; Yu, Y., CNT Interwoven Nitrogen and Oxygen Dual-Doped Porous Carbon Nanosheets as Free-Standing Electrodes for High-Performance Na-Se and K-Se Flexible Batteries. *Adv Mater* **2018,** *30* (49), e1805234.

56. Liu, W.; Oh, P.; Liu, X.; Myeong, S.; Cho, W.; Cho, J., Countering Voltage Decay and Capacity Fading of Lithium-Rich Cathode Material at 60 °C by Hybrid Surface Protection Layers. *Advanced Energy Materials* **2015,** *5* (13), 1500274.

57. Zhang, X. D.; Shi, J. L.; Liang, J. Y.; Yin, Y. X.; Zhang, J. N.; Yu, X. Q.; Guo, Y. G., Suppressing Surface Lattice Oxygen Release of Li-Rich Cathode Materials via Heterostructured Spinel Li4 Mn5 O12 Coating. *Adv Mater* **2018**, e1801751.

58. Huang, X.; Shi, K.; Yang, J.; Mao, G.; Chen, J., MnO 2 -GO double-shelled sulfur (S@MnO 2 @GO) as a cathode for Li-S batteries with improved rate capability and cyclic performance. *Journal of Power Sources* **2017,** *356*, 72-79.

59. Wang, W.; Wang, D.; Wang, G.; Zheng, M.; Wang, G., Elastic, Conductive Coating Layer for Self-Standing Sulfur Cathode Achieving Long Lifespan Li–S Batteries. *Advanced Energy Materials* **2020,** *10* (25).

60. Huang, D.; Li, S.; Luo, Y.; Xiao, X.; Gao, L.; Wang, M.; Shen, Y., Graphene oxide-protected three dimensional Se as a binder-free cathode for Li-Se battery. *Electrochimica Acta* **2016,** *190*, 258-263.

61. Youn, H. C.; Jeong, J. H.; Roh, K. C.; Kim, K. B., Graphene-Selenium Hybrid Microballs as Cathode Materials for High-performance Lithium-Selenium Secondary Battery Applications. *Sci Rep* **2016,** *6*, 30865.

62. Zeng, L.; Chen, X.; Liu, R.; Lin, L.; Zheng, C.; Xu, L.; Luo, F.; Qian, Q.; Chen, Q.; Wei, M., Green synthesis of a Se/HPCF–rGO composite for Li–Se batteries with excellent long-term cycling performance. *Journal of Materials Chemistry A* **2017,** *5* (44), 22997-23005.

63. Peng, X.; Wang, L.; Zhang, X.; Gao, B.; Fu, J.; Xiao, S.; Huo, K.; Chu, P. K., Reduced graphene oxide encapsulated selenium nanoparticles for high-power lithium–selenium battery cathode. *Journal of Power Sources* **2015,** *288*, 214-220.

64. Wang, B.; Zhang, J.; Xia, Z.; Fan, M.; Lv, C.; Tian, G.; Li, X., Polyaniline-coated selenium/carbon composites encapsulated in graphene as efficient cathodes for Li-Se batteries. *Nano Research* **2018,** *11* (5), 2460-2469.

65. Lee, S.; Lee, H.; Ha, N.; Lee, J. T.; Jung, J.; Eom, K., In Batteria Electrochemical Polymerization to Form a Protective Conducting Layer on Se/C Cathodes for High-Performance Li–Se Batteries. *Advanced Functional Materials* **2020,** *30* (19).

66. Sun, F.; Li, Y.; Wu, Z.; Liu, Y.; Tang, H.; Li, X.; Yue, Z.; Zhou, L., In situ reactive coating of metallic and selenophilic Ag2Se on Se/C cathode materials for high performance Li–Se batteries. *RSC Advances* **2018,** *8* (57), 32808-32813.

67. Ye, W.; Li, W.; Wang, K.; Yin, W.; Chai, W.; Qu, Y.; Rui, Y.; Tang, B., ZIF-67@Se@MnO2: A Novel Co-MOF-Based Composite Cathode for Lithium–Selenium Batteries. *The Journal of Physical Chemistry C* **2018,** *123* (4), 2048-2055.

68. Fang, R.; Zhou, G.; Pei, S.; Li, F.; Cheng, H. M., Localized polyselenides in a graphene-coated polymer separator for high rate and ultralong life lithium-selenium batteries. *Chem Commun (Camb)* **2015,** *51* (17), 3667-70.

69. Mukkabla, R.; Kuldeep; Killi, K.; Shivaprasad, S. M.; Deepa, M., Metal Oxide Interlayer for Long-Lived Lithium-Selenium Batteries. *Chemistry* **2018,** *24* (65), 17327-17338.

70. Si, L.; Wang, J.; Li, G.; Hong, X.; Wei, Q.; Yang, Y.; Zhang, M.; Cai, Y., High energy density lithium-selenium batteries enabled by a covalent organic framework-coated separator. *Materials Letters* **2019,** *246*, 144-148.

71. Yang, Y.; Hong, X.-J.; Song, C.-L.; Li, G.-H.; Zheng, Y.-X.; Zhou, D.-D.; Zhang, M.; Cai, Y.-P.; Wang, H., Lithium bis(trifluoromethanesulfonyl)imide assisted dual-functional separator coating materials based on covalent organic frameworks for high-performance lithium–selenium sulfide batteries. *Journal of Materials Chemistry A* **2019,** *7* (27), 16323-16329.

72. Yang, Z.; Zhu, K.; Dong, Z.; Jia, D.; Jiao, L., Stabilization of Li-Se Batteries by Wearing PAN Protective Clothing. *ACS Appl Mater Interfaces* **2019,** *11* (43), 40069-40077.

73. Wang, H.; Jiang, Y.; Manthiram, A., Long Cycle Life, Low Self-Discharge Sodium-Selenium Batteries with High Selenium Loading and Suppressed Polyselenide Shuttling. *Advanced Energy Materials* **2018,** *8* (7).

# Chapter 3 Experimental and Methodology

## 3.1 overview

The overall research route of this project mainly involves three procedures, as shown in **Figure 3.1**. Firstly, the materials are synthesized through different methods: *in situ* polymerization method is used for preparing the N, S dual-doped hierarchical porous carbon/Se composite coated with interconnected polyaniline (i-PANI@NSHPC/Se) cathode materials, and self-assembly method is employed for preparing the self-assembled cetrimonium bromide (CTAB)/carbon nanotube (CNT)/$Ti_3C_2T_x$ MXene composite modified polypropylene (PP) (CCNT/MXene/PP) separator.

Characterizations are conducted after the preparation process. In general, scanning electron microscopy (SEM) is used to observe the morphologies of the as-prepared materials, Raman and Fourier transform infrared (FTIR) spectroscopy are employed to for molecular examinations, ultraviolet-visible spectroscopy (UV-vis) for property characterization, X-ray diffraction (XRD) and thermogravimetric analysis (TGA) for additional experiments.

After characterizations, electrochemical measurements such as electrochemical impedance spectroscopy (EIS), cyclic voltammetry (CV), and galvanostatic discharge-charge, chronoamperometry techniques, are used to determine the performance of the as-fabricated batteries In addition, in situ permeation tests are conducted to visually observe the behaviour of polyselenides in Li-Se batteries. Contact angle tests are also performed.

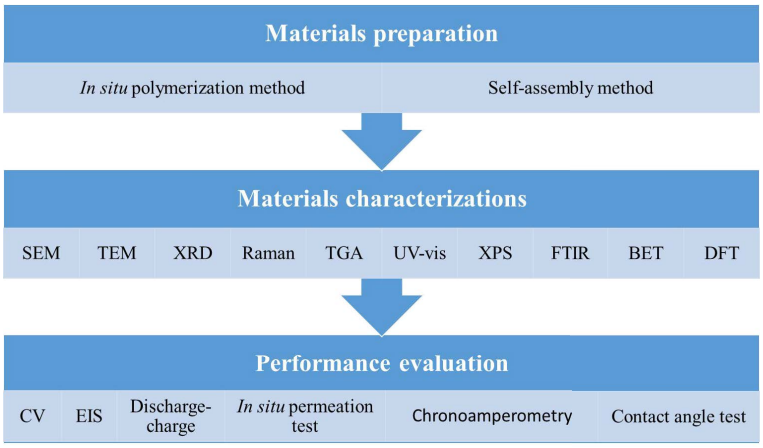


**Figure 3.1** Schematic illustration for materials preparation, characterizations and performance evaluations.

## 3.2 Materials and chemicals

A list of the names of materials and chemicals used in this project along with their formula, purity and supplier, is shown below in **Table 3.1**.

**Table 3.1** Materials and chemicals used in this research project

| Materials and Chemicals | Formula | Purity (%) | Supplier |
|---|---|---|---|
| Carbon black | C | 99 | SCI Materials Hub |
| Ethanol | $C_2H_5OH$ | 99.8 | Sigma-Aldrich |
| Poly(vinylidene fluoride) (PVDF) | $(CH_2CF_2)_n$ | -- | Sigma-Aldrich |
| N-Methyl-2-pyrrolidinone (NMP, anhydrous) | $C_5H_9NO$ | 99.5 | Sigma-Aldrich |
| Isopropyl alcohol | C3H8O | 98% | Chem-Supply |
| Acetone | $CH_3COCH_3$ | 99.9 | Chem-Supply |
| Aniline | $C_6H_5NH_2$ | 99 | Sigma-Aldrich |
| Hydrochloric acid | HCl | 32 | Sigma-Aldrich |
| Hexadecyltrimethylammonium bromide (CTAB) | $C_{19}H_{42}BrN$ | 99 | Sigma-Aldrich |
| Multi-walled carbon nanotubes | C | 96 | SCI Materials Hub |
| Copper foil | Cu | 99.9 | SCI Materials Hub |

| | | | |
|---|---|---|---|
| Aluminium foil | Al | 99.9 | SCI Materials Hub |
| Potassium hydroxide | KOH | 99.99 | Sigma-Aldrich |
| Sodium citrate dihydrate | $Na_3C_6H_5O_7 \cdot 2H_2O$ | 99 | Sigma-Aldrich |

## 3.3 Materials preparation

In this project, two different methods are mainly used to prepare cathode materials and composite separator materials for use in Li-Se and Na-Se batteries: *in situ* polymerization method and self-assembly method.

### 3.3.1 *In situ* polymerization method

*In situ* polymerization is used to develop various polymer nanocomposites and polymer coating. *In situ* polymerization usually involves an initiation step (initiated by an initiator), followed by a series of polymerization steps when exposed to heat, radiation and electrochemical signals. Therefore, by controlling the reaction conditions (such as pH, temperature, monomer concentration, initiator concentration, type of monomer and initiator, etc.), the polymerization kinetics can be adjusted with the desired particle shape and size.

Interestingly, the polymerization process can be carried out on the substrate materials with uniform growth layer to protect the internal cathode materials, such as 3D porous carbon materials, 2D graphene and reduced graphene oxide, 1D carbon nanotubes, etc. In this project, *in-situ* polymerization is mainly used for coating conductive thin layer on Se / C composites. By controlling the experimental conditions, the interconnected conductive network can be obtained.

### 3.3.2 Self-assembly method

Self-assembly method has been widely used in the synthesis of nanoparticles and heterostructures. When the pre-existing disordered system forms an ordered structural arrangement or pattern due to the interaction between species, the self-assembly process will occur. Self-assembly method can be driven by internal or external influences, such as electrical, magnetic, chemical, and interface energy minimization. In this project, the electrostatic attraction is the driving force of combining positively charged CTAB modified CNTs with negatively charged MXene nanosheets.

## 3.4 Materials characterizations

### 3.4.1 X-ray diffraction (XRD)

XRD measurement is widely used to analyze crystal structure based on the interaction between electromagnetic radiation (X-ray with wavelength of about 10-10 m) and samples. X-rays are generated in a vacuum X-ray tube, which consists of an anode (usually Cu) and a cathode (usually tungsten filament). If the condition satisfies Bragg's law, the interaction between the incident radiation and the sample will produce constructive interference

Bragg's law: $n\lambda=2d \sin \theta$,

where d is the crystal interplanar spacing, $\theta$ is the Bragg angle, n is the reflection order, and $\lambda$ is the wavelength of X-ray irradiation. The obtained XRD patterns can be matched with the crystal database by using the software (Jade, PDF 2019) to index the crystals of the samples. The Bruker D8 diffractometer with Cu K$\alpha$ radiation ($\lambda$ = 1.5418 Å) provided by UTS is used in this paper.

### 3.4.2 Scanning electron microscopy (SEM)

Scanning electron microscope (SEM) is a characterization technology, which can directly observe the sample by scanning the sample with high energy electron beam in grating scanning mode. After each scan, the signals generated by the sample contain information about the surface morphology, composition and conductivity of the sample, which are made up by the interaction between electrons and sample atoms.

Generally, SEM is used for the preliminary analysis of some materials. The basic use of SEM in this research project is to observe the morphology of porous carbon materials and electrode surfaces after cycling.

The SEM instrument used in this project is Zeiss Supra 55VP field emission SEM (FE-SEM). The accelerating voltage is 5-20 kV and the aperture is 10-30 mm at Sydney University of technology.

### 3.4.3 Transmission electron microscopy (TEM)

TEM measurements are used to analyze the morphology of the sample by allowing accelerated electron transport through the sample. The basic setup of TEM consists of five parts: vacuum system, sample stage, electron gun, electron lens and aperture.

Typically, TEM uses a high voltage of about 200 kV, which requires an ultra-high vacuum of $10^{-7}$-$10^{-9}$ Pa to prevent arcing at the TEM cathode. In order to prevent gas molecules from diffusing from the main chamber to the higher vacuum gun, a special isolated vacuum system is designed for the gun by using valves or differential pump aperture. The sample stage is equipped with an air lock, which can be inserted into the sample holder and minimize the vacuum loss in the whole vacuum chamber. The sample is usually dispersed in a solution and then dropped onto a grid (e.g., copper, molybdenum, gold, or platinum grid) and transferred to a sample holder and a sample stage. Electrons are generated by connecting

the filament to the negative power supply, and then be "pumped" from the electron gun to the anode plate and TEM column to complete the circuit. The electron lens is designed to focus parallel electrons to a small spot with a constant focal distance. In general, electromagnetic coils are also used to produce convex lenses. Since the deviation from the magnetic lens will cause aberration and worsen the spherical and chromatic aberration, the field produced by the lens must be radially symmetric.

Apertures are used to allow axial electrons to pass through; therefore, on the one hand, the beam intensity is reduced, which can be used for the analysis of sensitive samples. On the other hand, some unwanted scattered electrons can be removed by filtration to reduce the spherical aberration or chromatic aberration and diffraction when interacting with the sample. The imaging system has two modes: bright field imaging mode and diffraction imaging mode. The former is widely used in the current research because it gives a visual result of the sample morphology: the thicker area scatters electrons at a larger angle and presents a darker. In contrast, thinner areas show brighter images. This is especially useful for amorphous materials. The TEM instruments used in this thesis are Tecnai-G2 F30 S-Twin at UTS and JEM-2011 at Yangzhou University.

### 3.4.4 $N_2$ sorption/desorption measurement

N2 adsorption/desorption measurement is a powerful technique for analyzing the physical parameters (including specific surface area, pore size distribution and pore volume) of porous materials. In general, $N_2$ is used as an absorbent and cooled to 77K in liquid form. Then, a known amount of $N_2$ is diffused into the measuring tube, and a certain amount of $N_2$ gas is adsorbed on the sample surface due to the existence of pores. Finally, based on the fact that the amount of $N_2$ adsorbed is a function of the relative gas pressure P/P0, a typical adsorption isotherm plots is given. Pores can be divided into micropores, mesopores and

macropores, and can also be identified from isotherms according to IUPAC (the International Union of Pure and Applied Chemistry) classification.

In addition, the classical Brunauer Emmet Teller (BET) model is usually used to determine the surface area of samples. Kelvin equation is used to calculate the pore size distribution. Moreover, assuming that the density of the condensate at the experimental temperature is the same as that of the corresponding bulk liquid, the total pore volume can be determined by the amount of gas adsorbed on the plateau. In this paper, a Micrometrics ASAP2020 adsorption analyzer provided by UTS was used to measure the pore properties of the as-prepared materials

### 3.4.5 Raman spectroscopy

Raman spectroscopy, named after C.V. Raman, is a non-destructive and rapid detection spectroscopy technology, which relies on laser in the range of visible light, near-infrared light and near ultraviolet light to observe vibration, rotation and other low-frequency modes.

The vibrational information obtained in Raman spectroscopy is specific to the chemical bond and symmetry of molecules, thus providing enough information to identify specific molecular structures.

In this thesis, Raman spectroscopy is mainly used to identify the as-synthesized materials. The Renishaw inVia Raman spectrometer system for this project is equipped with Leica DMLB microscope (Wetzlar, Germany) and a 17 mW at 633 nm Renishaw helium neon laser.

### 3.4.6 Thermogravimetric analysis (TGA)

Thermogravimetric analysis (TGA) is a type of measurement commonly used to determine the weight change of certain samples during temperature changes in a controlled

atmosphere. This analysis can detect the weight of the sample as the temperature increases precisely. The results are usually presented in the curves to identify the weight loss processes associated with chemical reactions and water evaporation at certain temperatures.

In this project, TGA was used to determine the weight ratio of active material (Se) in the cathode composite. The TGA instrument used in this project is Simultaneous TG-DTA, in which the $Al_2O_3$ crucible is used as the sample holder. The temperature was set to increase to a certain point under $N_2$ atmosphere at the speed of 5-10 °C/min.

### 3.4.7 Fourier transform infrared (FT-IR) spectroscopy

Fourier transform infrared spectroscopy (FT-IR) is used to obtain infrared spectra of absorption, emission, photoconductivity or Raman scattering of solids, liquids or gases. FT-IR spectrometer can simultaneously collect spectral data in a wide spectral range. Compared with the dispersive spectrometer which only measure the intensity in a narrow wavelength range, it has obvious advantages.

The basic use of FT-IR in this research project is to analyze the structure of the samples (carbon materials and MXene composite separators). The FTIR instrument used in this project is Thermo Scientific FT-IR spectrometer, with a resolution of 4 $cm^{-1}$ and 64 scans at room temperature.

### 3.4.8 Ultraviolet-visible (UV-vis) spectroscopy

Ultraviolet-visible spectroscopy (UV-vis) is a technique that uses the absorption/reflection spectroscopy in part of the ultraviolet and the full, adjacent visible spectrum region. After absorbing the energy of ultraviolet or visible light, the molecules in the samples containing π - electrons or non-bonding electrons excite the electrons to higher

anti-bonding molecular orbitals.

In this project, the UV-vis instrument is mainly used to determine the chemical composition of the electrolytes in the *in situ* permeation experiments after discharging.

The UV-vis absorption spectra, using the Beer-Lambert Law, in this thesis are measured by a Cary 60 UV-vis spectrophotometer at UTS.

### 3.4.9 X-ray photoelectron spectroscopy (XPS)

XPS is a common technique for analyzing the surface chemistry of samples, including element composition, chemical formula, chemical state and electronic state of samples. The technique is based on counting the number of internal / valence photoelectrons emitted by atoms and their binding energies. Each element will produce a set of characteristic XPS peaks at a given binding energy. XPS technology has been applied in many research fields because of its ability to test various samples in the fields of nanomaterials, photovoltaic, catalysis, energy storage, corrosion science and inorganic synthesis.

In this thesis, an EASY ESCA spectrometer (VG ESCA LAB MKII) is used to identify the surface chemistry of samples.

### 3.4.10 Density functional theory (DFT) calculations

Density functional theory (DFT) is a very useful computational modeling method, which can be used in many fileds, such as physics, chemistry and materials science, because it plays a key role in studying the electronic structure of many-body systems, especially atoms, molecules and condensed phases.

DFT calculation can provide information about chemical interaction, bond length, Bard

charge and density of state, which is very constructive to provide support for experimental.

In this thesis, the Computational resources have been provided by the National Supercomputing Centers in Shanghai University.

## 3.5 Battery test

For all electrochemcial tests, the batteries are measured with the LANDdt Tester and/or Neware Tester system. Dscharge-charge profiles are recoreded at certain current densities by calculating the rate and mass of active materials.

The cyclic voltammograms (CV) and electrochemical impedance spectroscopy (EIS) measurements were collected with a VMP3 multichannel potentiostat at UTS.

# Chapter 4 A Nitrogen, Sulfur Dual-Doped Hierarchical Porous Carbon with Interconnected Conductive Polyaniline Coating for High-Performance Sodium-Selenium Batteries

## 4.1 Introduction

High-energy and low-cost rechargeable battery has been highly demanded for powering portable electronics, electric vehicles and renewable energy storage [1-4]. Recently, selenium (Se), one of the chalcogen elements, has attracted considerable attention owing to its high specific capacity (678 mAh $g^{-1}$). In addition, Se is highly conductive ($1 \times 10^{-3}$ S $m^{-1}$), which can render high utilization of Se and high rate performance. These features make it a promising cathode candidate with high energy densities [5-7]. On the other hand, compared to the limited resources of lithium (Li), sodium (Na) with abundant resources and similar electrochemical property to Li is more suitable for large-scale and low-cost industrial applications [8]. Therefore, the Na-Se battery is expected to be an advanced energy storage system with high energy densities and low cost [9-11].

However, Se cathodes suffer from rapid capacity decay and low Coulombic efficiency (CE) because of the shuttling of polyselenides from the cathode to the anode, which is a common issue in alkali-chalcogen batteries [6, 12-18]. Based on the previous works, the most widely used strategy is to incorporate Se in conductive hosts such as mesoporous carbon [6, 19] and carbon nanofiber [20]. Furthermore, it is well recognized that heteroatoms doping can enhance the chemical affinity with polyselenides. In this respect, different heteroatom (nitrogen, oxygen, sulphur) doped carbon hosts have been designed to inhibit the polyselenides shuttling and improve the electrochemical performances [18, 21-22]. However,

these strategies are less effective in Na-Se batteries compared to that of Li-Se batteries due to the sluggish kinetics in Na-Se batteries, especially when the content of Se is higher than 50 wt% in the cathode materials [22]. Recently, conductive polymer coating was designed as a protective barrier to confine polyselenides on the cathode side [23-26]. With the conductive polymer coating, the polyselenides are restricted inside the carbon host, leading to prohibited 'shuttle effect' and enhanced cycling stability. Although such strategies have been applied successfully in Li-S and Li-Se batteries [23, 26], few works on Na-Se batteries have been reported to achieve long cycle stability (1000 cycles) with high capacity under the conditions of high Se areal mass loading (3.5 mg $cm^{-2}$) and high current density (2 C).

Herein, we report a rationally designed architecture of N, S dual-doped hierarchical porous carbon/Se composite coated with interconnected polyaniline (i-PANI@NSHPC/Se) via an *in situ* polymerization approach. The interconnected polyaniline coating can be facilely synthesized by simply controlling the concentration of aniline and acetone during polymerization. The merits of such architecture include: 1) The hierarchical porous structure enables sufficient electrolyte penetration into the carbon host. 2) With the combination of PANI coating and heteroatoms doping, the 'shuttle effect' of polyselenides can be significantly suppressed owing to both physical confinement and chemical adsorption between the carbon matrix and $Na_xSe$ ($0<x\leq2$). 3) In addition, the interconnected PANI networks provide high-speed transfer pathway for electrons and charges, enabling high rate performance. As a result, the as-prepared i-PANI@NSHPC/Se cathode material can deliver a high reversible capacity of 617 mAh $g^{-1}$ after 200 cycles at 0.2 C, corresponding to 91.4% of its theoretical capacity. It also presents an excellent rate capability at 20 C of 380 mAh $g^{-1}$. Furthermore, stable cyclabilities over 1000 cycles have been achieved with different Se areal mass loadings (1.2, 2.3, 3.5 mg $cm^{-2}$) at 2 C.

## 4.2 Experimental section

### 4.2.1 Materials

Hydrochloric acid (HCl, 32%), aniline (99%) were purchased from Sigma-Aldrich. All chemicals were used as received without further purification.

### 4.2.2 Synthesis of N, S dual-doped hierarchical porous carbon

N, S dual-doped hierarchical porous carbon (denoted as NSHPC) was prepared according to a previous method with some modifications [27]. Briefly, sodium citrate dihydrate was dried at 155 °C under vacuum for 48 h before use. The dried sample was then ground to get ultrafine powders with a pestle in a mortar. To prepare NSHPC, 5 g of sodium citrate was mixed with 0.1 g thiourea and ground thoroughly. The mixture was then transferred to a tube furnace and calcined at 700 °C under Ar atmosphere for 1.5 h with a heating rate of 5 °C/min. Afterwards, the obtained product was washed with 1M HCl and DI water till the filtrate became neutral. The powder was then dried at 80 °C under vacuum overnight. Then the powder was further treated with KOH at a mass ratio of 1:3 in 10 ml deionized water and probe-sonicated for 30 min. The suspension was then dried at 80 °C under vacuum overnight. Further calcination treatment was conducted at 800 °C for 1h with a heating rate of 5 °C $min^{-1}$ under Ar atmosphere to get NSHPC. Hierarchical porous carbon (HPC) was also prepared without any thiourea.

### 4.2.3 Preparation of selenium-based cathodes

300 mg NSHPC was mixed thoroughly with 600 mg selenium powder by ground. The mixture was then poured into a sealed glass vial in the Ar-filled glovebox. After that, the

glass vial was heated at 260 °C for 12 h under $N_2$ atmosphere with a heating rate of 2 °C/min. The final product was collected as NSHPC/Se. HPC/Se was prepared in the same way.

### 4.2.4 Preparation of i-PANI@NSHPC/Se, PANI@NSHPC/Se and i-PANI@HPC/Se composites

The i-PANI@NSHPC/Se composite was prepared via *in situ* polymerization of aniline. A certain amount of acetone was added to control the growth of polyaniline. Firstly, 300 mg NSHPC/Se composite was dispersed in 17 ml DI water and 3 ml acetone in a round-bottomed flask and sonicated for 1 h to form a uniform suspension. Secondly, 0.03 g aniline monomer was injected into the flask and stirred for another 2 hours with an ice bath and $N_2$ bubbling to remove oxygen in the solution. Then, a solution of 0.06g ammonium persulfate, $(NH_4)_2S_2O_8$ (APS), in 19 ml 1M HCl aqueous solution with 2 ml acetone was pre-cold in a refrigerator before wise dropped into the suspension. This reaction was conducted for 6 h and the sample was collected as i-PANI@NSHPC/Se. For comparison, the polymerization was conducted in 51 ml DI water and 3 ml acetone with other conditions unchanged to prepare PANI@NSHPC/Se without interconnected structure. The i-PANI@HPC/Se composite was synthesized in the same way as the preparation of i-PANI@NSHPC/Se by replacing NSHPC/Se with HPC/Se.

### 4.2.5 Characterization

The X-ray diffraction technique (XRD) was used to investigate the phases of the samples using a Siemens D5000 diffractometer with Cu Kα radiation (λ = 1.5418 Å) in the range of 2θ = 10-80°. The morphologies of the samples were examined with a field emission scanning electron microscopy (FESEM, Zeiss Supra 55VP) and transmission electron microscopy

(TEM, JEOL JEM-2011). Raman spectra were obtained from a Renishaw inVia spectrometer system (Gloucestershire, UK) which is equipped with a Leica DMLB microscope (Wetzlar, Germany) and a Renishaw He-Ne laser source procuring 17 mW at 633 nm. XPS measurements were conducted on an ESCALAB250Xi (Thermo Scientific, UK) equipped with monochromated Al K alpha (energy 1486.68 eV). Brunauer-Emmett-Teller (BET) and Barret-Joyner-Halenda (BJH) method were used to determine specific surface area, pore volumes and pore size distribution with a Micromeritics 3Flex analyser (Micromeritics Instrument Corporation, Norcross, GA, USA). The selenium content was confirmed using a TGA thermogravimetric analyzer (2960 SDT system) under $N_2$ atmosphere at 650 °C with a heating rate of 10 °C $min^{-1}$.

## 4.2.6 Electrochemical measurements

To prepare the working electrodes, the i-PANI@NSHPC/Se composite was mixed with carbon black and sodium alginate (SA) binder in a weight ratio of 8:1:1 and ground to form a uniform slurry. Then, the slurry was pasted onto an aluminium foil and dried at 60 °C overnight under vacuum. The loading of active material in each electrode was approximately 1-2 mg $cm^{-2}$. Afterwards, the cells using the electrodes were prepared in an Ar-filled glovebox. Sodium foils were used as the counter and reference electrode. The electrolyte was prepared by adding 1 M sodium perchlorate ($NaClO_4$, Sigma-Aldrich, 99.95%) in EC/DEC (1:1 in v/v). The galvanostatic charge/discharge tests were conducted using a LAND CT2001A system in the range of 0.5-3V and the specific capacity is calculated based on the mass of Se. A VMP3 multichannel potentiostat was used to conduct cyclic voltammograms (CV) and electrochemical impedance spectroscopy (EIS) measurements. The CV tests were performed within the voltage range of 0.5-3 V at a scan rate of 0.1 mV $s^{-1}$. HPC/Se,

NSHPC/Se, PANI@NSHPC/Se and i-PANI@HPC/Se electrodes were also prepared and tested for comparison.

## 4.2.7 Density functional theory (DFT) calculations

The theoretical calculations were performed based on the first-principles method using the ab initio simulation package with VASP code, which applies projector augmented wave (PAW) pseudopotential to demonstrate the interaction between electrons and ions. The generalized gradient approximation (CGA) based on the Perdew-Burke-Ernzerhof version is employed to describe the electronic exchange-correlation effects. The convergence is ensured with a cut-off energy of 400 eV. A 6×6 supercell of single-layer graphene is constructed as the model of non-doped carbon. Herein, thiophene-like sulphur and pyrrolic nitrogen are employed as representative dopants for the doped carbon. To exclude the interactions between the graphene layer and its images, a vacuum layer in the vertical direction is set to be 16 Å. The Monkhorst-Pack method is used to make the k-space which is sampled with a 3×3×1 k-point grid. Ionic relation is calculated based on the conjugate-gradient algorithm. The binding energy ($E_b$) of $Na_2Se$ and $NaSe_2$ on the carbon substrate is defined as Equations (1) and (2):

$$E_{b1} = Esub + ENa_2Se - Esub+Na_2Se \quad (1)$$

$$E_{b2} = Esub + ENaSe_2 - Esub+NaSe_2 \quad (2)$$

Where Esub, $ENa_2Se$, $ENaSe_2$, $Esub+Na_2Se$ and $Esub+NaSe_2$ represent the ground-state energies of the carbon substrate, $Na_2Se$, $NaSe_2$, carbon-$Na_2Se$ and carbon-$NaSe_2$ composites, respectively. The more negative value means the stronger binding energy.

### 4.2.8 *Ex situ* characterization

To investigate the 'shuttle effect' behaviour of polyseneides during electrochemical reaction, the coins cells were disassembled after 100 cycles in the glove box. The cathodes and anodes were taken out and then washed with propylene carbonate (PC) several times to remove the residual electrolyte. After the evaporation of PC at 50°C in the glove box, the cathode materials were taken out for *ex situ* Raman and XPS characterizations. The Na anodes were sealed in argon and quickly transferred to SEM machine for morphology and EDX characterizations.

## 4.3 Results and discussion

### 4.3.1 Morphology and Structure

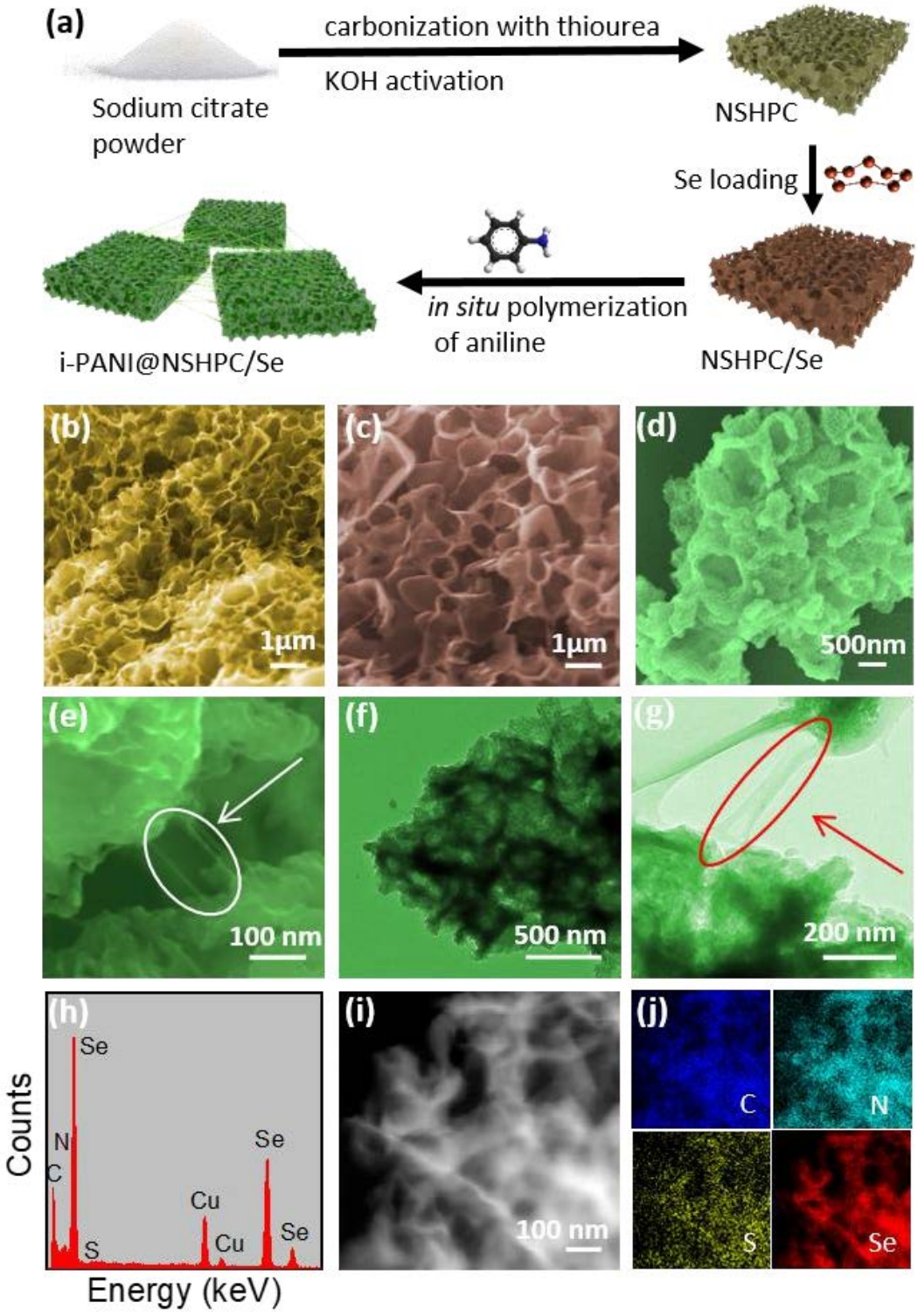

**Figure 4.1 (a)** Schematic illustration of the preparation of i-PANI@NSHPC/Se composite. SEM images of **(b)** NSHPC, **(c)** NSHPC/Se and **(d, e)** i-PANI@NSHPC/Se. **(f, g)** TEM images of i-PANI@NSHPC/Se. **(h)** HRTEM-EDS spectrum of i-PANI@NSHPC/Se. **(i, j)** HRTEM image and corresponding EDS elemental maps of C, N, S and Se in i-PANI@NSHPC/Se composite.

The preparation of i-PANI@NSHPC/Se composite is schematically illustrated in **Figure 4.1a**, in which the N, S dual-doped porous carbon with hierarchical pores is selected as the carbon host for loading Se. Herein, NSHPC was first prepared by carbonization of sodium citrate and thiourea, followed by KOH activation. The NSHPC/Se composite was then obtained via a simple melt-diffusion method. Finally, the polyaniline (PANI) layer with interconnected structure was grown on NSHPC/Se via an *in situ* polymerization of aniline at 0 °C in Ar atmosphere. The morphologies of the as-prepared samples were investigated by the scanning electron microscopy (SEM). **Figure 4.1b-d** present the SEM images of NSHPC, NSHPC/Se and i-PANI@NSHPC/Se composites, respectively. As indicated in **Figure 4.1b**, the as-prepared NSHPC has a hierarchical porous structure with large macropores.

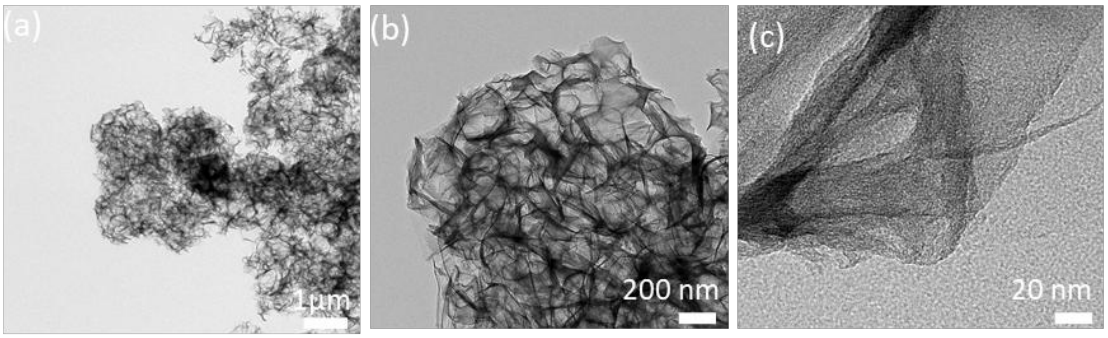


**Figure 4.2 (a, b)** TEM images of NSHPC. **(c)** HRTEM images of NSHPC.

In addition, plenty of micro and mesopores can also be observed in the transmission electron microscopy (TEM) images in **Figure 4.2**, which can provide a large surface area for

accommodating Se. After loading with Se, the morphology of NSHPC does not change and no detectable individual Se particles can be observed on the carbon surface in **Figure 4.1c**. This suggests that Se is successfully loaded into NSHPC via the melt-diffusion process. After coated with polyaniline (PANI), the i-PANI@NSHPC/Se composite still well maintains the hierarchical structure except that the surface of the composite becomes rough (**Figure 4.1d**). This indicates that PANI is successfully polymerized on the NSHPC/Se surface. TEM was employed to observe the thickness of the PANI coating (~20 nm) in **Figure 4.3a**. Notably, the PANI coating with interconnected networks can be clearly observed in **Figure 4.1e**, **Figure 4.3b and c**, which is expected to enhance the conductivity. High-resolution TEM image of i-PANI@NSHPC/Se in **Figure 4.1f** shows that the micropores almost disappear. This confirms that these pores are occupied by Se and the uniform PANI coating. The interconnected PANI structure is further characterized in **Figure 4.1g**, in which the two individual particles are connected by the PANI networks. The formation of interconnected PANI structure could be due to the proper concentration of aniline and acetone in the solution when polymerization proceeds. In order to investigate the element composition of i-PANI@NSHPC/Se, the HRTEM-EDS spectra and element mappings are shown in **Figure 4.1h-j,** which confirms the coexistence of C, N, S, Se and uniform elemental distributions in the i-PANI@NSHPC/Se composite.

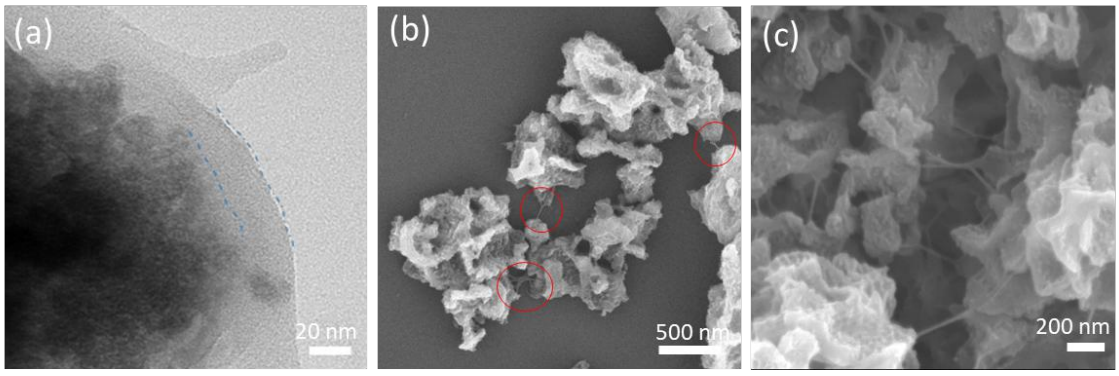

**Figure 4.3 (a)** TEM image of i-PANI@NSHPC/Se. **(b, c)** SEM image of i-PANI@NSHPC/Se

## 4.3.2 XRD, Raman BET and XPS characteriazations

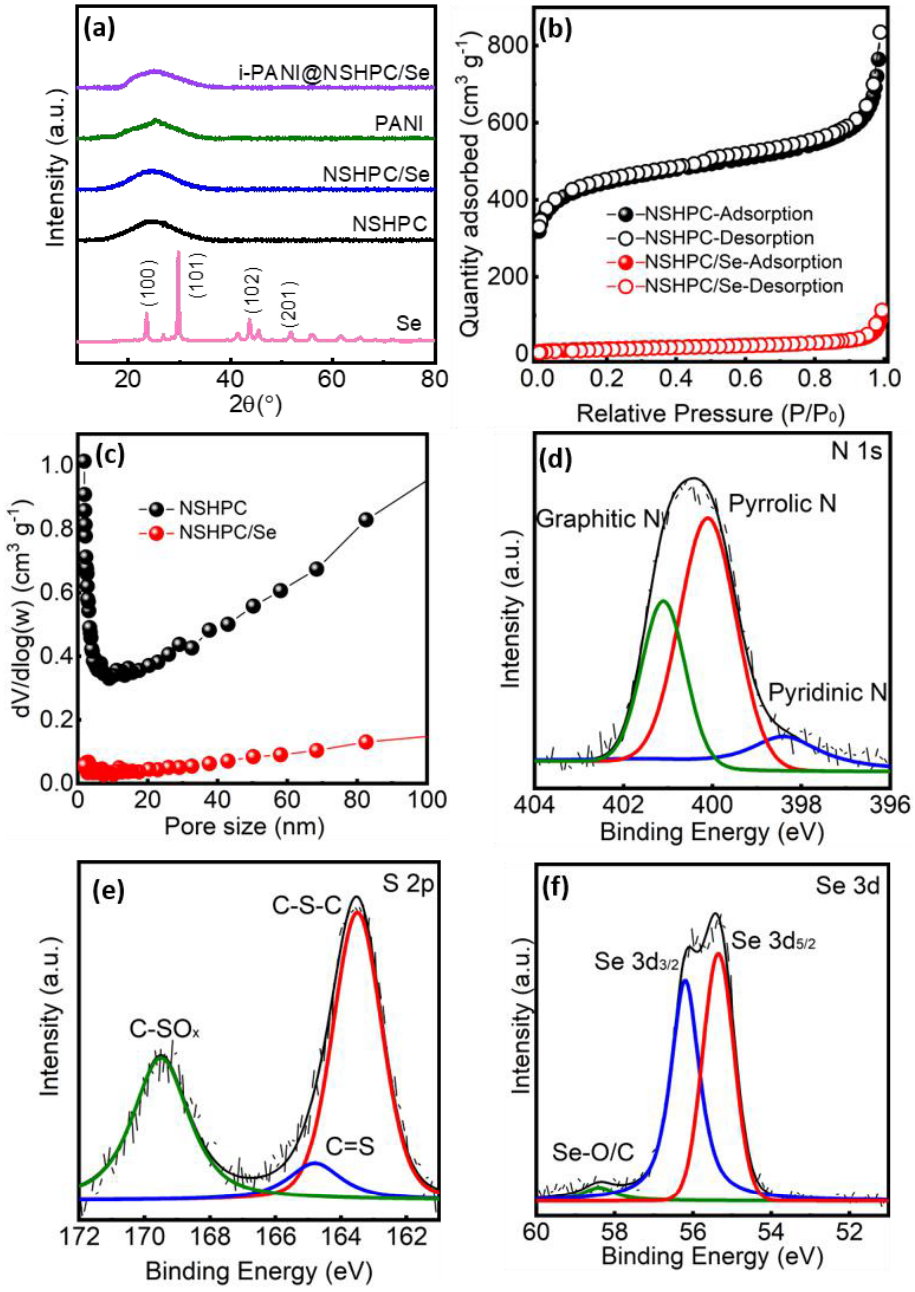


**Figure 4.4 (a)** XRD patterns of Se, NSHPC, NSHPC/Se, PANI and i-PANI@NSHPC/Se composites. **(b)** Nitrogen adsorption-desorption isotherms of NSHPC and NSHPC/Se

composite. **(c)** Pore size distributions of NSHPC and NSHPC/Se, XPS spectra of **(d)** N 1s, **(e)** S 2p and **(f)** Se 3d in i-PANI@NSHPC/Se composite.

The X-ray diffraction (XRD) patterns of Se, NSHPC, NSHPC/Se, PANI, and i-PANI@NSHPC/Se are presented in **Figure 4.4a**. The NSHPC shows a typical broad diffraction peak of amorphous carbon. The pristine Se is highly crystalline with well-defined sharp diffraction peaks, which are indexed to the trigonal crystal system $P3_221$. In contrast, the diffraction peaks of trigonal Se disappear in NSHPC/Se composite, indicating a low crystalline state of Se and a good dispersion of Se in the NSHPC host [28]. After coated with PANI, the peaks in i-PANI@NSHPC/Se composite is similar to that of NSHPC/Se.

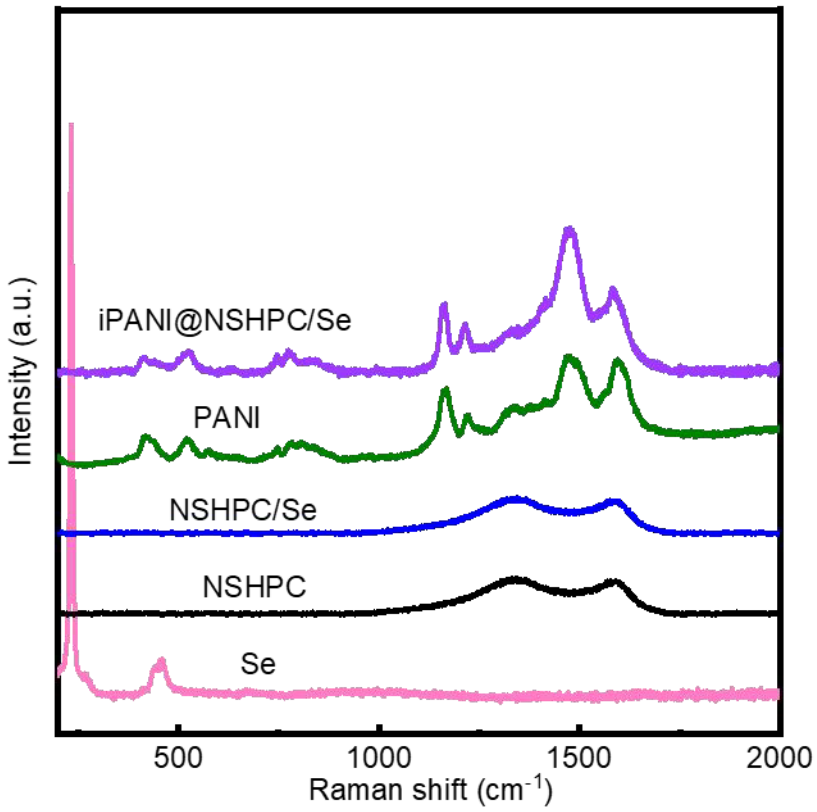


**Figure 4.5** Raman spectra of Se, NSHPC, NSHPC/Se, PANI and i-PANI@NSHPC/Se composite.

Furthermore, **Figure 4.5** displays the Raman spectra of the as-prepared materials. For the pristine Se, there is a characteristic peak at 236 $cm^{-1}$. NSHPC has two broad peaks at 1340 and 1565 $cm^{-1}$, which correspond to the disordered (D band) and graphitized carbon (G band), respectively. The intensity ratio ($R = I_D/I_G$) reflects the defects in the carbon matrix, in which R = 1.1 in NSHPC, indicating the low graphitic nature of NSHPC [14]. This might be due to the defects in the carbon matrix caused by nitrogen and sulphur dopants [29]. After Se infiltration, no obvious Se peaks can be seen in the Raman spectrum of the NSHPC/Se composite, which further demonstrates a good incorporation of Se into the NSHPC host. In addition, the R value of NSHPC/Se decreases to 1.01, reflecting an increased graphitic property compared to that of NSHPC due to the strong interaction between Se atoms and carbon matrix [22]. The i-PANI@NSHPC/Se composite shows similar Raman spectrum to that of pure PANI, which also proves that the NSHPC/Se composite is uniformly wrapped by the PANI coating.

The infiltration of Se into different carbon hosts was further investigated by the Brunauer-Emmett-Teller (BET) method. As shown in **Figure 4.4b**, the BET results show that NSHPC has a large specific surface area (1434 $m^2\ g^{-1}$) and the total pore volume based on BJH model is about 0.76 $cm^3\ g^{-1}$ ($V_{micropore}$ = 0.45 $cm^3\ g^{-1}$). Based on the pore size distributions in **Figure 4.4c**, the majority of porosity in NSHPC is in the region with pore size less than 4 nm. As reported previously, the micro and mesopores can effectively confine Se [20, 30]. Based on the density of amorphous Se (4.26 g $cm^{-3}$), the micropores in NSHPC can hold as much as 65.7 wt% Se. After Se impregnation, the surface area decreases to 50.4 $m^2\ g^{-1}$ and the micro-meso pores almost disappear, giving a total pore volume of 0.15 $cm^3\ g^{-1}$. In addition, the unoccupied volume is expected to buffer the large volume expansion during cycling, which is crucial for improving the cycle stability [22].

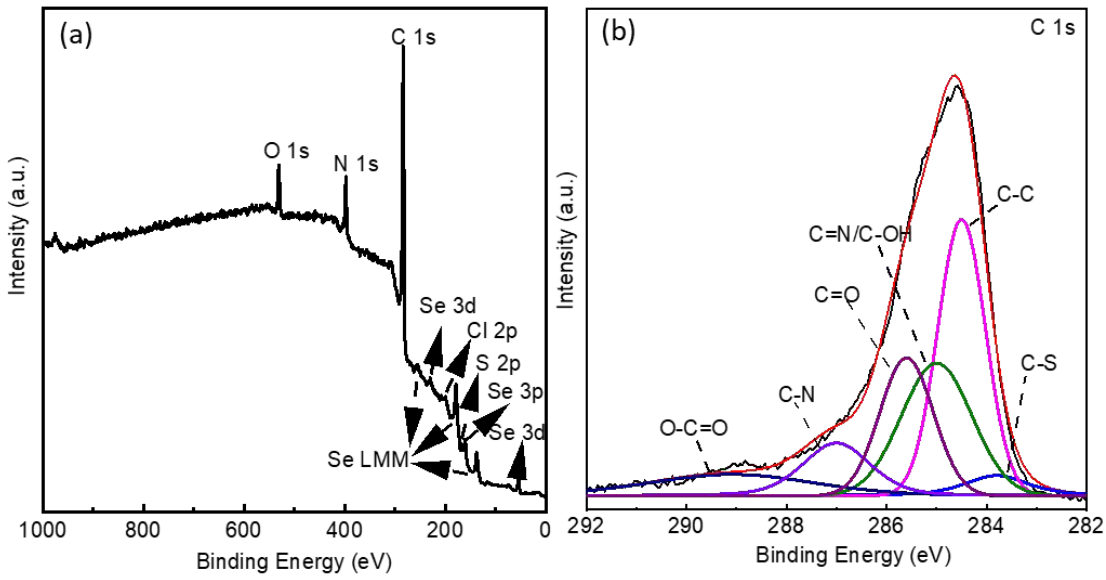


**Figure 4.6 (a)** XPS survey spectrum of i-PANI@NSHPC/Se. **(b)** high-resolution of C 1s XPS spectra acquired from i-PANI@NSHPC/Se composite.

The X-ray photoelectron spectroscopy (XPS) measurement was conducted to investigate the chemical nature of i-PANI@NSHPC/Se. **Figure 4.6a** shows the XPS survey spectrum of i-PANI@NSHPC/Se composite, in which the peaks at 532 eV (O 1s), 399 eV (N 1s), 285 eV (C 1s), 200 eV (Cl 2p) and 164 eV (S 2p) are observed. In addition, the signals of Se 3d and Se 3p are also presented. The spectrum of C 1s (**Figure 4.6b**) in i-PANI@NSHPC/Se can be divided into several peaks at 284.5, 285, 285.6, 289.1, 287 and 283.8 eV, which correspond to C-C, C=N/C-OH, C=O, O-C=O, C-N and C-S [31], respectively. These indicate strong interactions between C and N, S dopants. In addition, the oxygen groups on the carbon matrix are also believed to improve the binding ability to polyselenides [22, 30]. For N 1s in **Figure 4.4d**, it shows three typical peaks located at 398.4 (pyridinic N), 400.1 (pyrrolic N) and 401.2 eV (graphitic N), respectively. Both the pyridinic and pyrrolic N are beneficial for the electrochemical activity [31]. **Figure 4.4e** shows three typical peaks of S 2p at around 163.6, 164.8 and 168.8eV, which confirms the existence of C-S-C, C=S and C-SOx, respectively. According to the previous study, the thiophene S (S atoms that directly bonded with carbon

via C-S bonding) is able to positively charge the carbon matrix [21], leading to strong interactions between the positively charged carbon and polyselenides. The XPS spectrum of Se is depicted in **Figure 4.4f**, the two peaks at 56.2 and 55.34 eV are assigned to 3d Se3/2 and 3d Se5/2 with a spin-orbit splitting of 0.86 eV. In addition, there is a weak peak at around 58.2 eV, which might be attributed to the surface oxidation of selenium or the strong interaction between Se and the porous carbon [32-33].

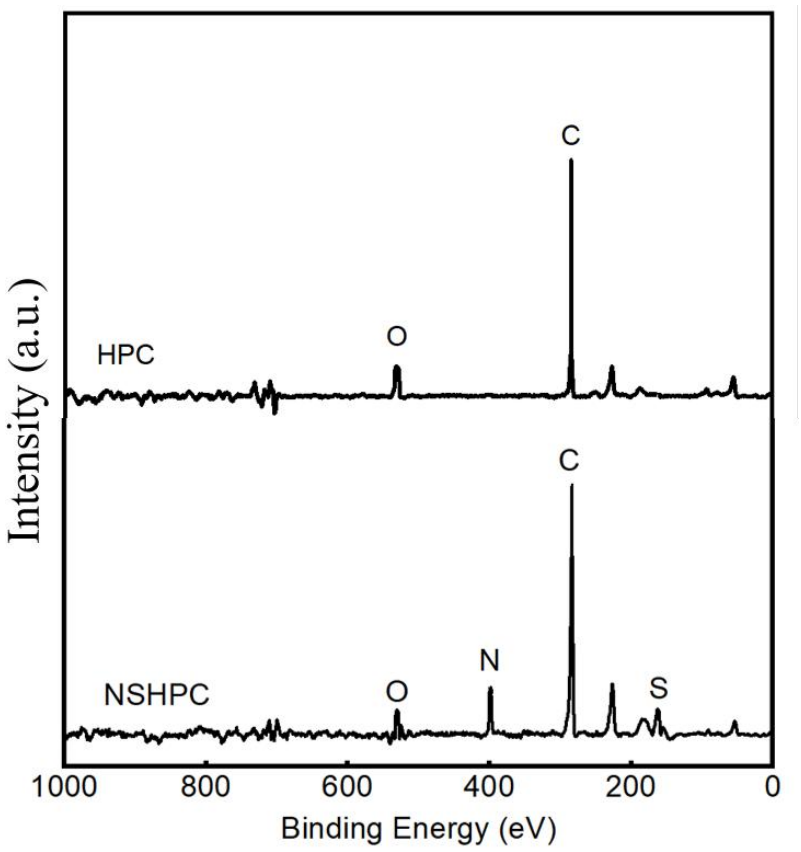


**Figure 4.7** XPS survey spectrum of HPC and NSHPC

To further confirm the contents of doped N and S in NSHPC composite, the NSHPC is dried at 120 °C for 24 hours under vacuum to remove any moisture for XPS measurement. **Table 4.1** shows the elemental composition from the XPS results. The contents of N and S in NSHPC are 7.4 at.% (7.9 wt.%) and 3.9 at.% (9.6 wt.%), respectively. The atom ratios of N/S in NSHPC is 1.897, which is close to the ratio of N/S in thiourea (2:1) as the dopant. In

addition, the XPS survey of HPC was also conducted (**Figure 4.7**). The small amount of O in HPC and NSHPC could be due to the surface oxidation of carbon matrix and KOH activation that brings –OH groups onto the carbon surface.

**Table 4.1** Element composition data in N, S dual-doped hierarchical porous carbon obtained from XPS analysis

| Elements | wt. % | at. % |
|---|---|---|
| C | 78.1 | 84.9 |
| N | 7.9 | 7.4 |
| S | 9.6 | 3.9 |
| O | 4.4 | 3.6 |
| N/S | -- | 1.897 |

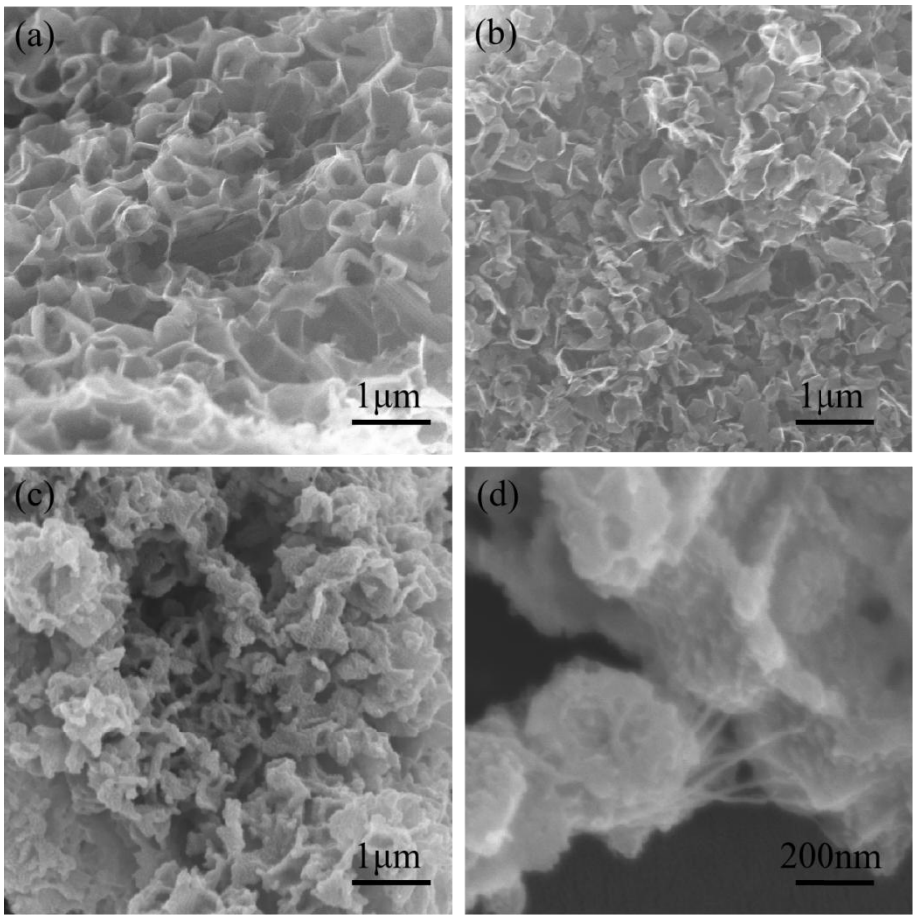


**Figure 4.8** SEM images of **(a)** HPC. **(b)** HPC/Se. **(c, d)** i-PANI@HPC/Se.

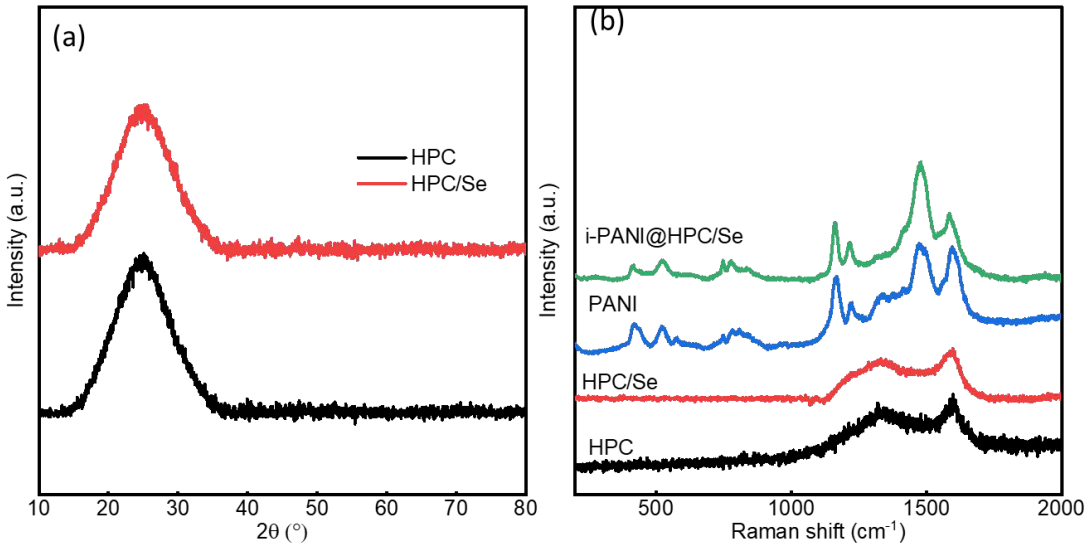


**Figure 4.9 (a)** XRD spectra of HPC and HPC/Se. **(b)** Raman spectra of HPC, HPC/Se, PANI and i-PANI@HPC/Se.

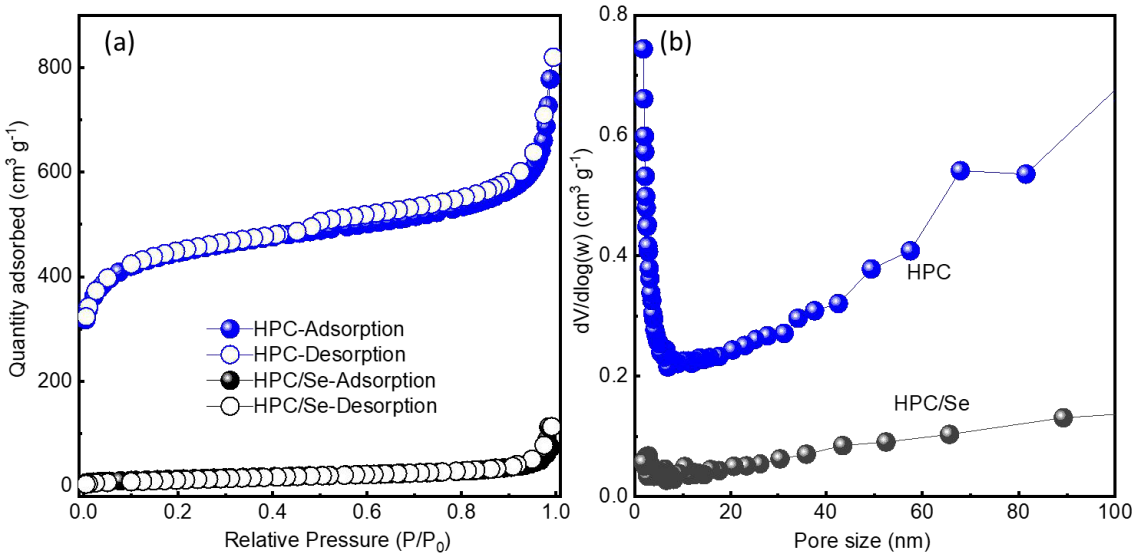


**Figure 4.10 (a)** Nitrogen adsorption-desorption isotherms of NSHPC and NSHPC/Se composite. **(b)** Pore size distributions of NSHPC and NSHPC/Se.

For comparison, hierarchical porous carbon (HPC) and HPC/Se without N and S doping were also prepared by removing thiourea from the reactant. Characterizations of HPC and HPC/Se are presented in **Figure (4.8-4.10)**. The SEM images are shown in **Figure 4.8a and b**, in which the HPC also shows a porous structure with obvious macropores and the HPC/Se has a similar structure to HPC with no bulk Se on the carbon surface. In addition, both XRD and Raman spectra (**Figure 4.9**) of HPC/Se show there are no obvious Se peaks, indicating a good incorporation of Se into HPC matrix. The decrease of specific surface area and pores also indicates that Se is loaded into the micro and meso pores of HPC (as shown in **Figure 4.10**).

## 4.3.3 TG measurement

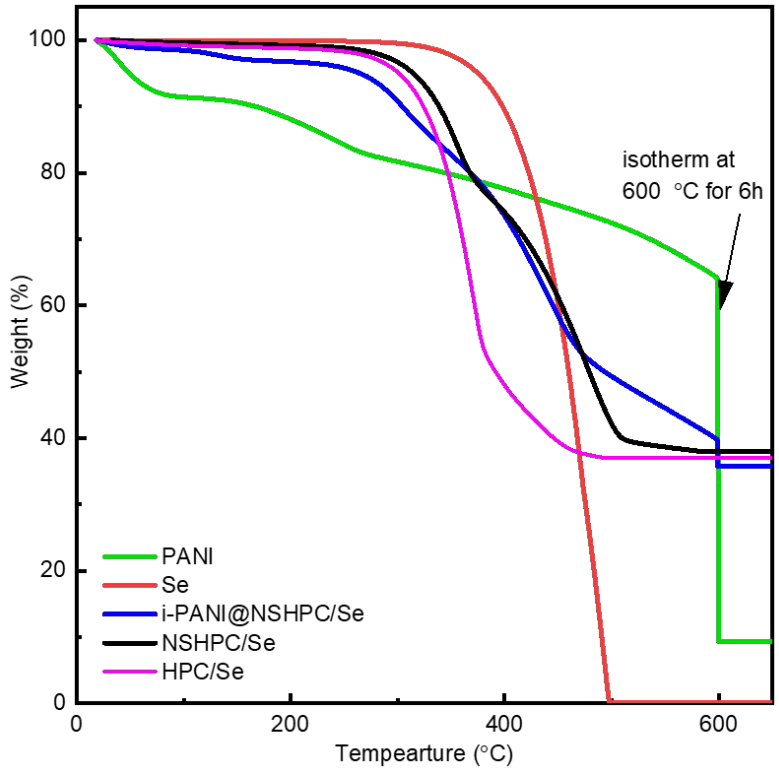


**Figure 4.11** TG profiles of Se, PANI, HPC/Se, NSHPC/Se and i-PANI@NSHPC/Se composites.

To investigate the Se content in these composites, the thermogravimetric analysis (TGA) under N2 atmosphere is employed in **Figure 4.11**. The contents of Se in HPC/Se and NSHPC/Se are about 63 wt% and 62 wt%, respectively, which are less than the initial amount (66.7 wt%). The difference may be due to the evaporation of Se on the carbon surface under 300 °C. It is worth noting that the elimination rate of Se in NSHPC/Se composite is much slower than that of pure Se, which might be due to both the physical and chemical interaction between Se and carbon matrix. This phenomenon is also observed for S in N, S dual-doped porous carbon. The evaporation of Se is even slower after PANI coating, which could be the result of the PANI layer that prevent Se from evaporation. The mass loss of i-PANI@NSHPC/Se composite can be divided into three steps: 1) evaporation of $H_2O$ on the surface of i-PANI@NSHPC/Se composite below 100 °C; 2) further elimination of $H_2O$ inside the pores of the composite and partial carbonization of PANI in the range of 100-300 °C; 3) further carbonization of PANI and evaporation of Se in the range of 300-600 °C. To accurately obtain the mass loss of PANI after fully carbonization, an isothermal treatment under 600 °C for 6 h is conducted for both pure PANI and i-PANI@NSHPC/Se sample. The weight loss of PANI before 100 °C could be due to the evporation of unbound $H_2O$ and HCl. Taking consideration of mass change of both Se (100 wt% mass loss) and PANI (~90 wt% mass loss), the content of Se in i-PANI@NSHPC/Se is calculated to be 57 wt%, which is higher than most of the previously reported works.

## 4.3.4 Electrochemical measurements

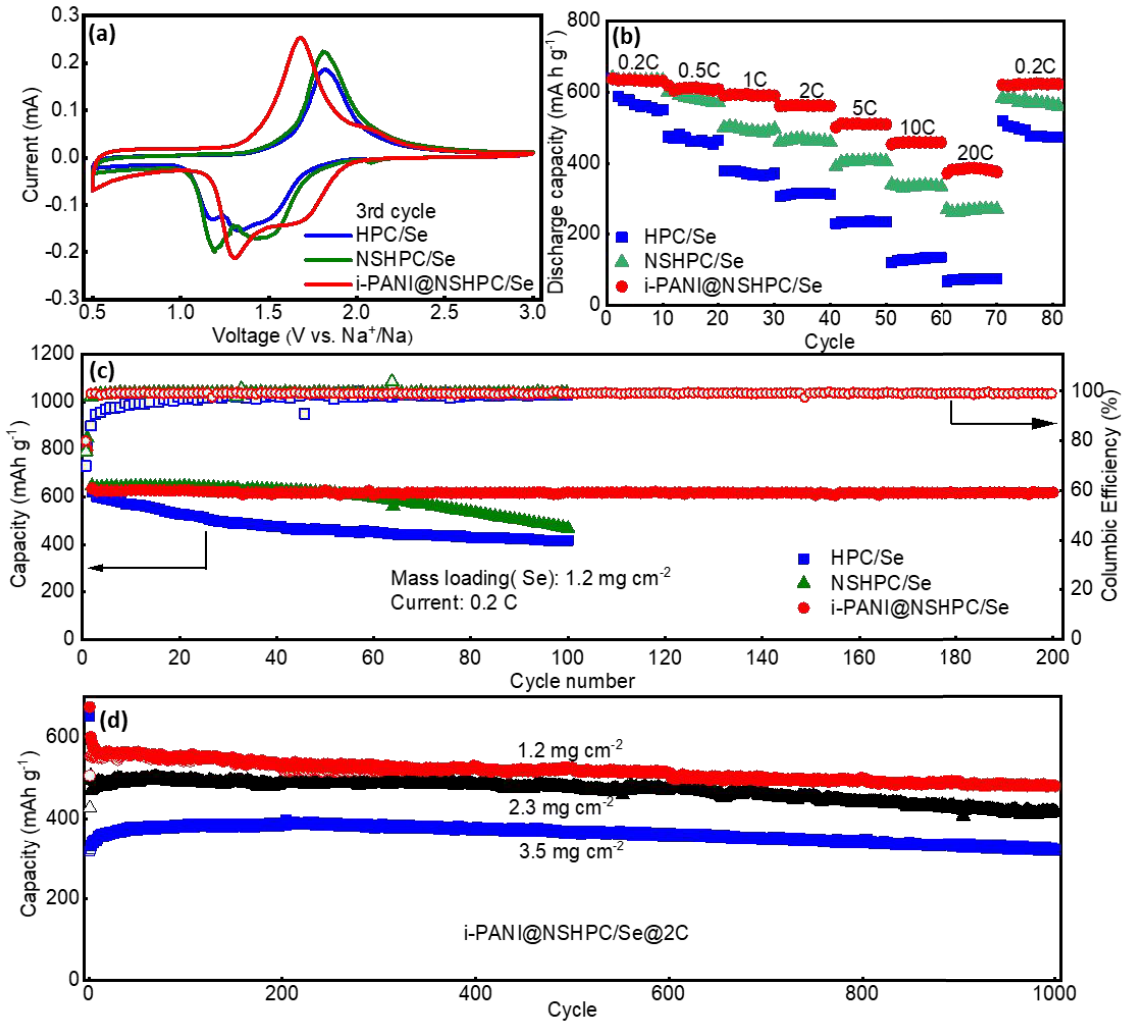


**Figure 4.12 (a)** the 3rd cycle CV curves of HPC/Se, NSHPC/Se and i-PANI@NSHPC/Se at a scan rate of 0.1 mV $s^{-1}$ in the range of 0.5-3.0 V. **(b)** Rate performances of HPC/Se, NSHPC/Se and i-PANI@NSHPC/Se composites. **(c)** Cycling performances of HPC/Se, NSHPC/Se and i-PANI@NSHPC/Se at a current density of 0.2 C with Se mass loading of 1.2 mg $cm^{-2}$. **(d)** Long cycling performance of i-PANI@NSHPC/Se battery at 2 C with Se areal mass loading of 1.2, 2.3 and 3.5 mg $cm^{-2}$.

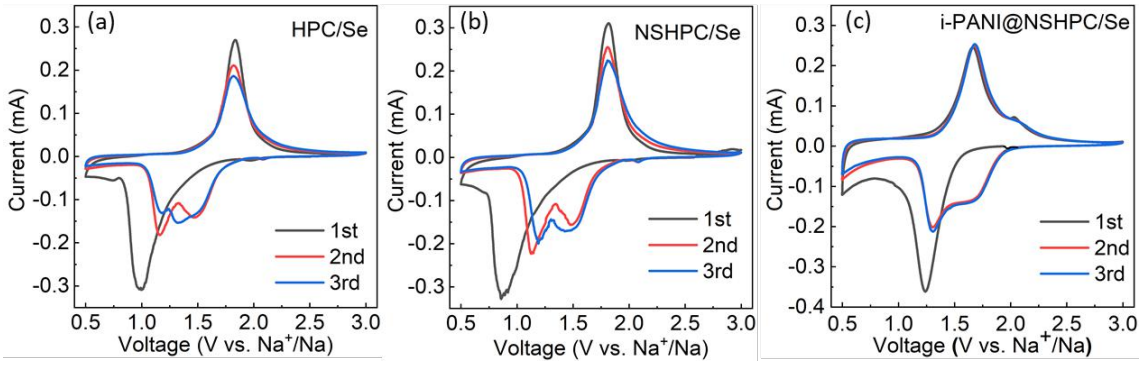


**Figure 4.13** CV profiles of **(a)** HPC/Se. **(b)** NSHPC/Se and **(c)** i-PANI@NSHPC/Se.

**Figure 4.12a** and **Figure 4.13** show cyclic voltammetry (CV) characteristics of HPC/Se, NSHPC/Se and i-PANI@NSHPC/Se electrodes at 0.1 mV/s within 0.5-3 V. The i-PANI@NSHPC/Se cathode exhibits a pair of anodic and cathodic peaks at ~1.7 and 1.2 V in the first cycle (**Figure 4.13c**), respectively. This signifies a direct conversion from $Se_8$ to $Na_2Se$ without formation of complex polyselenides in the first cycle [11, 14, 22]. Upon the second discharge process, two cathodic peaks are observed, indicating the formation of intermediates. While the anodic peaks are stable and overlap with each other in the following cycles, which suggests that $Na_2Se$ is directly oxidized to Se [30]. HPC/Se and NSHPC/Se also present similar CV behaviour to that of i-PANI@NSHPC/Se in **Figure 4.13a, b**. However, both HPC/Se and NSHPC/Se cathodes display larger polarization than i-PANI@NSHPC/Se. The lowest potential polarization and best reversibility in i-PANI@NSHPC/Se could be due to the improved electrochemical reaction kinetics and enhanced ionic transfer with interconnected PANI coating. Other works also confirms that coating with polymers, graphene and $Al_2O_3$ will have influences on the redox peaks with narrower potential intervals [13, 23, 26, 34]. In addition, as indicated in **Figure 4.12a**, the amplitudes of the redox peaks of HPC/Se and NSHPC/Se in the 3rd cycle are also lower than that of i-PANI@NSHPC/Se cathode as well as larger polarization, indicating the best reactivity and reversibility of PANI@NSHPC/Se among the three samples. **Figure 4.12b** shows the rate capability of HPC/Se, NSHPC/Se and

i-PANI@NSHPC/Se electrodes. The i-PANI@NSHPC/Se electrode has the best rate performance among the three electrodes, which presents a high capacity of 386 mAh $g^{-1}$ at 20 C and then recovers back to 626 mAh $g^{-1}$ at the current of 0.2 C. Whereas, HPC/Se and NSHPC/Se only deliver 74 and 270 mAh $g^{-1}$ at the current of 20 C, respectively. The excellent rate performance of i-PANI@NSHPC/Se electrode could be attributed to the high conductivity and fast charge transport in the interconnected PANI structure.

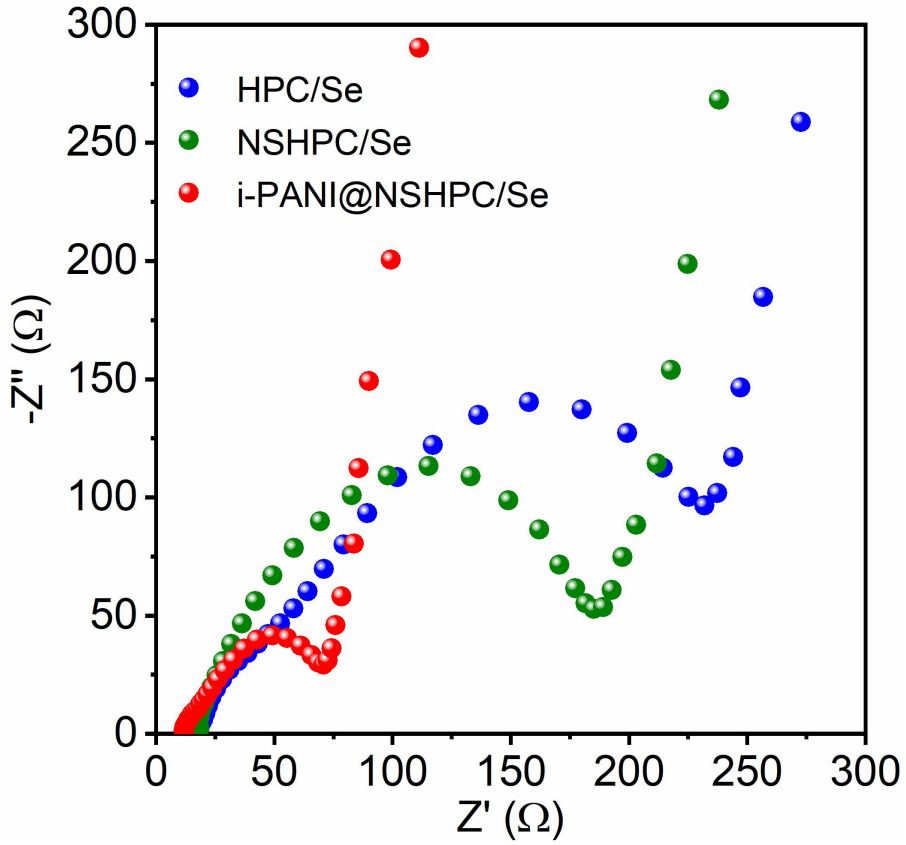


**Figure 4.14** Nyquist plots of HPC/Se, NSHPC/Se and i-PANI@NSHPC/Se after third cycle from 1M Hz to 0.1 Hz at room temperature.

This is further investigated by the electrochemical impedance spectroscopy (EIS) measurements in **Figure 4.14**. As it shows, the i-PANI@NSHPC/Se cathode has the lowest charge transfer resistance ($R_{ct}$) compared to that of HPC/Se and NSHPC/Se, which suggests a preferable kinetics of Na ion diffusion in the i-PANI@NSHPC/Se electrode. The cycling

performances of the three electrodes are presented in **Figure 4.12c** at a current density of 0.2 C. For HPC/Se, it shows an obvious capacity decay upon the initial cycle and stays relatively stable after 40 cycles. This could be due to the weak physical interactions between polyselenides and HPC host. In contrast, the NSHPC/Se electrode delivers a quite stable capacity in the first 60 cycles but then undergoes fast capacity decay. It is assumed that the N, S dopants play important role in maintaining the capacity due to the chemical adsorption between N, S doped carbon and polyseleindes. However, the long-lasting exposure of Se to the electrolyte without any protection will induce serious 'shuttle effect', leading to fast capacity decay. Notably, i-PANI@NSHPC/Se presents ultra-stable cyclability at 0.2 C, maintaining a capacity of 617 mAh $g^{-1}$ after 200 cycles, corresponding to 91.4% of its theoretical capacity.

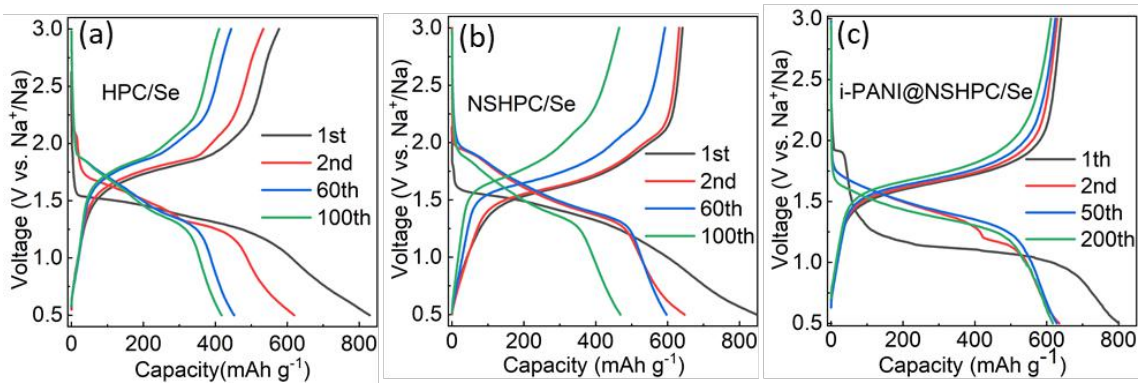


**Figure 4.15** GDC profiles of **(a)** HPC/Se, **(b)** NSHPC/Se and **(c)** i-PANI@NSHPC/Se

The detailed galvanostatic discharge/charge profiles at 0.2 C are presented in **Figure 4.15**. As indicated, all three cathodes present high discharge capacities exceeding the theoretical capacity (678 mAh $g^{-1}$) in the first discharge, which is due to the formation of SEI layer and side reactions between Se and the electrolyte [7]. The first charge capacities of the three cathodes (HPC/Se, NSHPC/Se and i-PANI@NSHPC/Se) are 577, 641 and 640 mAh $g^{-1}$, corresponding to the initial Coulombic Efficiency (ICE) of 70%, 75.7% and 80.1%,

respectively. The highest ICE of i-PANI@NSHPC/Se cathode indicates the highest utilization of the active material. In addition, the polarization of HPC/Se and NSHPC/Se becomes larger as the cycle increases, which could be due to the severe 'shuttle effect' that causes the loss of Se on the cathodes. The smaller polarization of i-PANI@NSHPC/Se cathode further confirms the preferable kinetics of i-PANI@NSHPC/Se for Na-Se batteries. Therefore, i-PANI@NSHP/Se has superior electrochemical activity and conductivity than HPC/Se and NSHPC/Se, with improved rate and cycling performances. In addition, the Coulombic efficiency (CE) of i-PANI@NSHPC/Se cell is over 99% after the 1st cycle. Both the high CE and excellent cyclability suggest that the parasitic shuttle effect has been effectively suppressed in the i-PANI@NSHPC/Se batteries. Importantly, the novel interconnected structure of PANI can enhance the conductivity of the electrode, which makes it kinetically preferable for fast transport of charges. The stable long cycling performances of i-PANI@NSHPC/Se at 2 C with different Se areal mass loadings are shown in **Figure 4.12d**. All three i-PANI@NSHPC/Se batteries with Se areal mass loadings of 1.2, 2.3 and 3.5 mg $cm^{-2}$ present stable cyclability and high capacities.

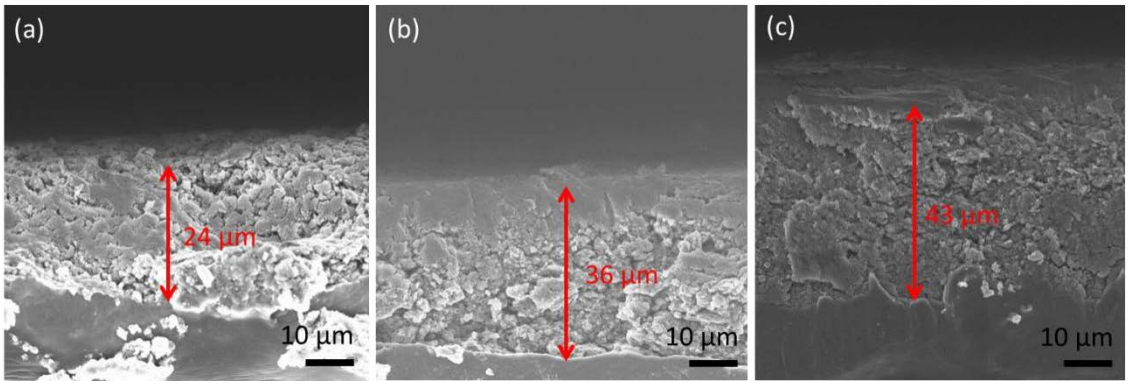


**Figure 4.16** SEM images of the cathode cross section corresponding to **(a)** 1.2 mg $cm^{-2}$, **(b)** 2.3 mg $cm^{-2}$, **(c)** 3.5 mg $cm^{-2}$.

**Figure 4.16** shows the corresponding cross-section SEM images of the electrodes with different Se areal mass loading (denoted as i-PANI@NSHPC/Se-1.2, i-PANI@NSHPC/Se-2.3 and i-PANI@NSHPC/Se-3.5). For the i-PANI@NSHPC/Se-1.2 cathode, it delivered the highest capacity and maintains 480 mAh $g^{-1}$ after 1000 cycles at 2 C with nearly 100% CE and low capacity fading rate. To the best of our knowledge, this is the one of the best performances in Na-Se batteries so far. The i-PANI@NSHPC/Se-2.3 and i-PANI@NSHPC/Se-3.5 cathodes also delivered stable cycling performances only with slightly lower capacities. Interestingly, there is a capacity recovery for i-PANI@NSHPC/Se-2.3 and i-PANI@NSHPC/Se-3.5 cathodes at the initial stage, which could be due to the gradual activation of Se under high current densities. When compared to other works in Na-Se battery in **Figure 4.12 e** and **f,** our results show superior performances over the previously reported studies. As indicated, most studies have tried to achieve high areal mass loading with long stable cycling performance. However, as the cycles and areal mass loading increase, the shuttle effect become more eminent, leading to poor capacity retention.

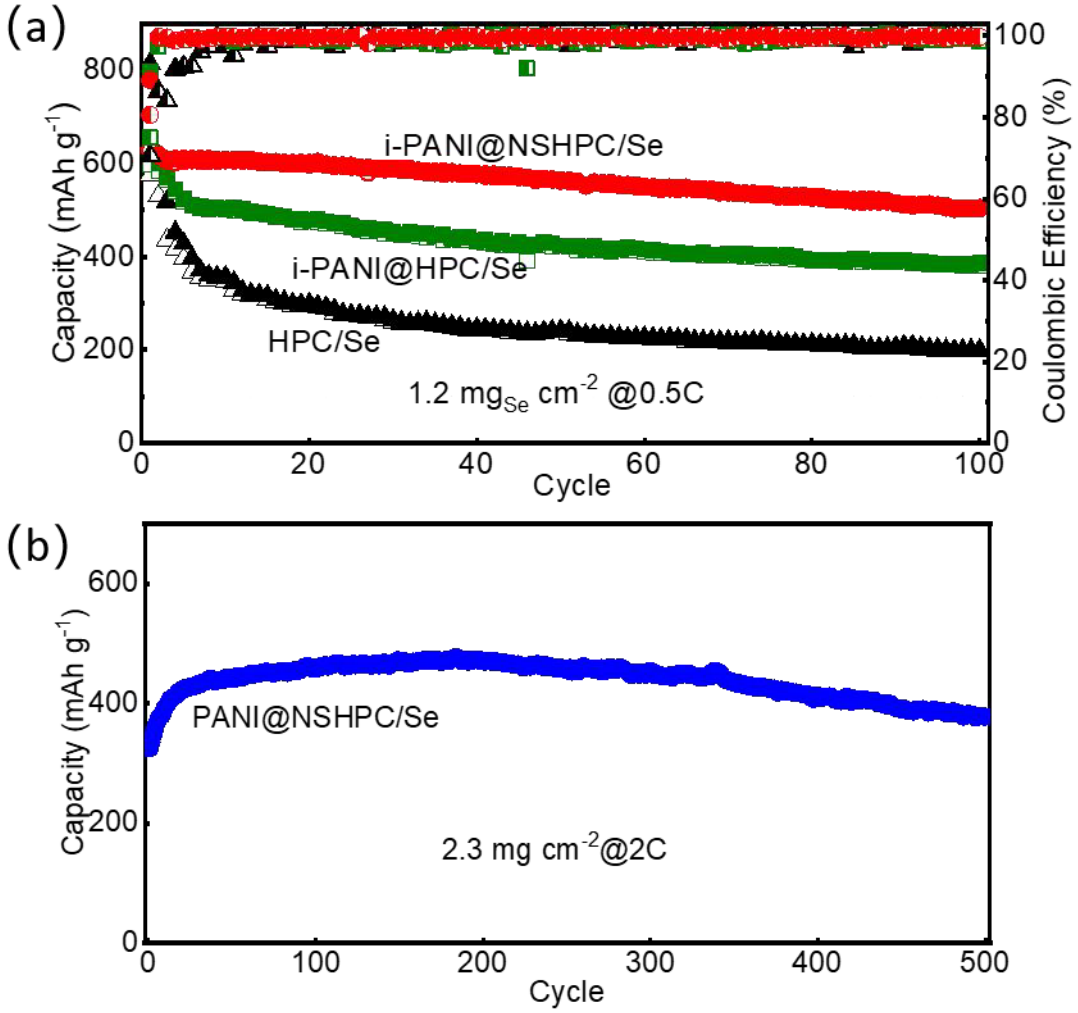


**Figure 4.17 (a)** Cycling performance of HPC/Se, i-PANI@HPC/Se and i-PANI@NSHPC/Se at 0.5 C with Se areal mass loading of 1.2 mg $cm^{-2}$, **(b)** cycling performance of PANI@NSHPC/Se at 2 C with Se areal mass loading of ~2.3 mg $cm^{-2}$.

To verify the physical limitations of interconnected PANI coating without N, S doping, the HPC/Se composite with only interconnected PANI coating (i-PANI@HPC/Se) was prepared in the same way as i-PANI@NSHPC/Se for comparison. The SEM images of i-PANI@HPC/Se are presented in Figure 4.8c and d, in which a rough surface on HPC/Se and the interconnected PANI network can be observed. Raman spectra were conducted to further prove the successful coating of PANI on HPC/Se in **Figure 4.9b**, the similar Raman spectrum of i-PANI@HPC/Se to that of pure PANI indicates that HPC/Se are uniformly wrapped by

PANI layer. Then, the HPC/Se, i-PANI@HPC/Se and i-PANI@NSHPC/Se composites were tested as the cathode materials in Na-Se battery for 100 cycles at a current of 0.5 C (**Figure 4.17**). For the HPC/Se battery, the capacity quickly decreases to ~300 mAh $g^{-1}$ after about 10 cycles at 0.5 C and can only maintain 200 mAh $g^{-1}$ after 100 cycles. For the i-PANI@HPC/Se battery, it has much better cycling performance than HPC/Se battery and can deliver a capacity of ~ 380 mAh $g^{-1}$ after 100 cycles at 0.5 C, which suggests that the shuttle effect is suppressed by interconnected PANI coating. Although the capacity of i-PANI@HPC/Se is much higher than HPC/Se after 100 cycles, it decreases fast in the first few cycles. The fast capacity decay of i-PANI@HPC/Se indicates the loss of Se from the cathode, which could be due to the weak interaction between Se and undoped carbon host. In contrast, i-PANI@NSHPC/Se has much improved cyclability with higher capacity than i-PANI@HPC/Se. After 100 cycles, the i-PANI@NSHPC/Se cathode can still deliver a high capacity of ~505 mAh $g^{-1}$, which could be attributed to the synergistic effects of N, S dual-doping and interconnected PANI coating.

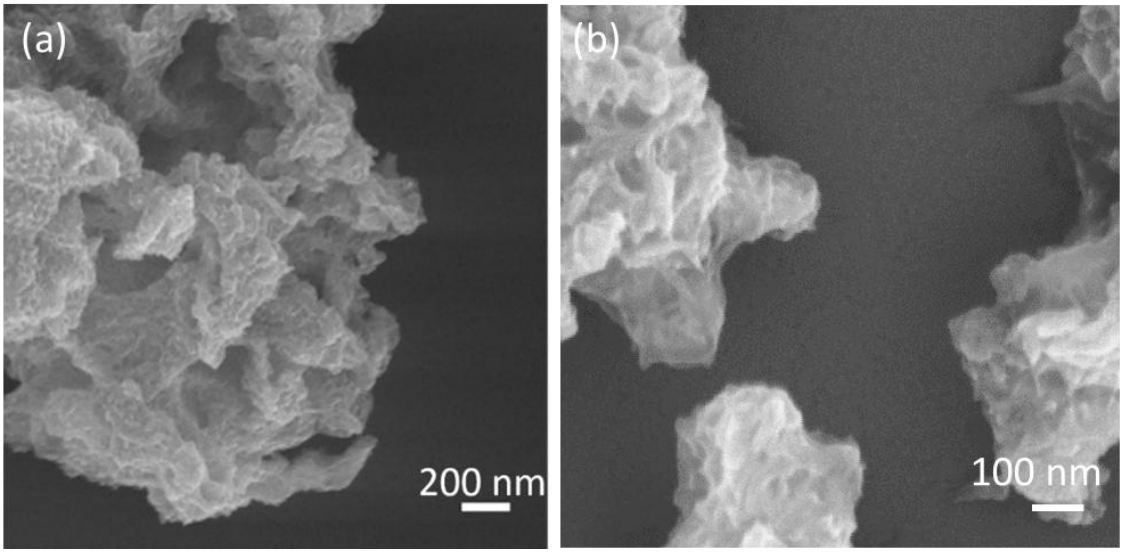


**Figure 4.18** SEM image of PANI@NSHPC/Se.

In addition, the advantages of the interconnected structure of PANI coating without interconnected structure was also investigated for comparison (PANI@NSHPC/Se). The SEM image of PANI@NSHPC/Se is shown in **Figure 4.18**, which shows a rough surface on the NSHPC/Se composite without interconnected PANI network. The long cycling performance of the electrodes (PANI@NSHPC/Se) was tested at 2 C with Se areal mass loading of 2.3 mg $cm^{-2}$. As it shows in **Figure 4.17b**, the PANI@NSHPC/Se cathode exhibits a quite stable performance in the first 200 cycles with a slight increase of capacity from initial cycles but decreases gradually in the following cycles. There is a long activation stage in the first 50 cycles which might be due to the electrolyte penetration and the low utilization of active material (Se) in the initial cycling stage. Compared to that of i-PANI@NSHPC/Se cathode, the PANI@NSHPC/Se cathode delivers lower capacity, longer activation stage and faster capacity decay.

## 4.3.5 DFT calculations

To theoretically verify the interaction between NSHPC and Se species, the binding energy between different carbon matrix and polyselenide representatives ($Na_2Se$, $NaSe_2$) have been calculated based on the First-Principle computational methods. The most stable geometric configurations of the $NaSe_2$ and $Na_2Se$ molecules interacting with different carbon substrates are shown in **Figure 4.19(a-l)** and **Figure 4.20** along with the corresponding binding energies. The possible N, S dual-doped carbon configurations are 1N + 1S doped carbon (denoted as NS-C), 2N + 1S doped graphene (N2S-C) and pure carbon is selected as the carbon matrices in **Figure 4a-l**. The optimized geometry conformation models are established based on the previous reports.[39] The undoped carbon matrix only offers relatively low binding energies to both $NaSe_2$ and $Na_2Se$, which are -0.66 eV and -1.01 eV, respectively, indicating a weak interaction between $NaSe_2$/$Na_2Se$ and the undoped carbon matrix. In

contrast, after doping with N and S, the binding energies between NS-C, N2S-C and $NaSe_2$/$Na_2Se$ are -2.63/-3.81 eV and -4.23/-5.54 eV, respectively, which indicates stronger chemical interaction between the $NaSe_2$/$Na_2Se$ and N, S dual-doped carbon.

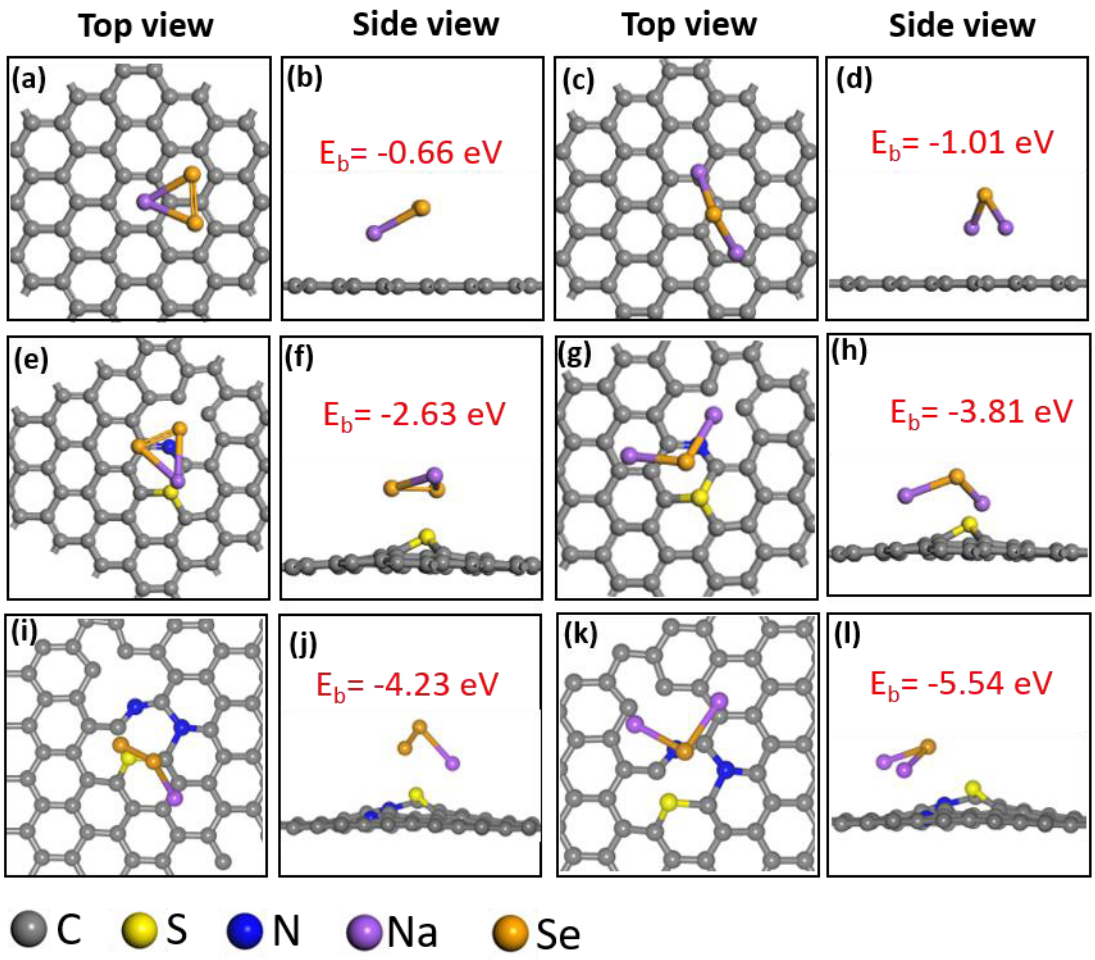


**Figure 4.19** Ab initio calculations illustrating the binding between $NaSe_2$, $Na_2Se$ and various carbon matrices: **(a-d)** carbon matrices. **(e-h)** 1N + 1S doped carbon. **(i-l)** 2N + 1S doped carbon.

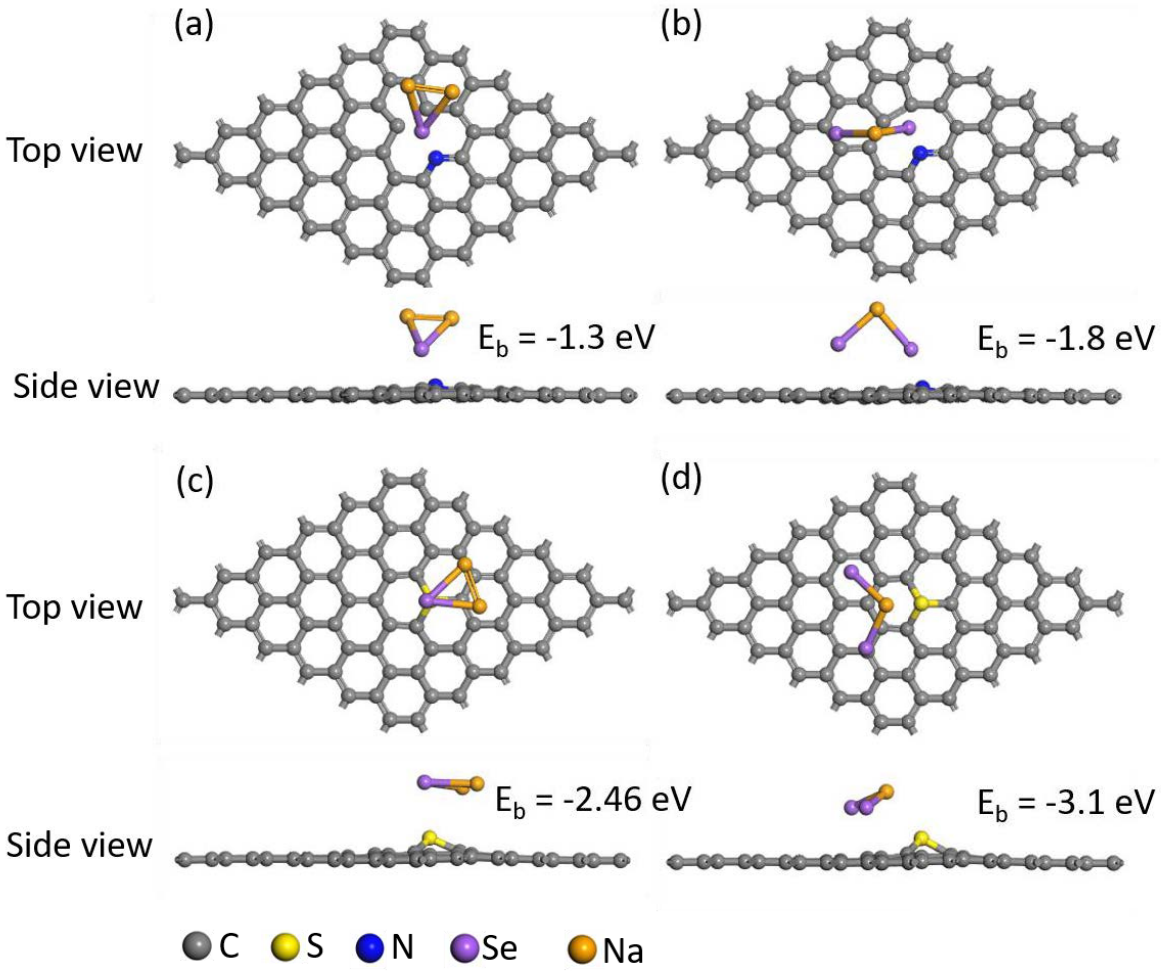


**Figure 4.20** Ab initio calculations illustrating the binding between $NaSe_2$, $Na_2Se$ and different carbon substrates **(a, b)** N doping. **(c, d)** S doping along with the binding energies.

## 4.3.6 *Ex situ* characterization study

Furthermore, *ex situ* instrumental analyses were conducted to figure out the possible mechanisms for the improved electrochemical performance of i-PANI@NSHPC/Se cells in **Figure 4.21a-j**. The cathode materials, glass fibre separators and corresponding anodes were taken out for *ex situ* Raman, digital images and *ex situ* SEM, EDS mapping, respectively. **Figure 4.21a** shows the *ex situ* Raman spectra of HPC/Se, NSHPC/Se and i-PANI@NSHPC/Se batteries after 100 cycles at 0.2 C. The obvious Se peaks in HPC/Se and

NSHPC/Se composites suggest the detective Se on the surface of the cathode, which could be due to the diffusion of sodium polyselenides and then re-oxidized to Se on the surface of the carbon matrix. While there is no obvious Se peak observed in the i-PANI@NSHPC/Se sample, indicating that the diffusion of polyselenides is effectively suppressed by the PANI layer. **Figure 4.21 (b,e, h)** show the corresponding SEM images of the Na anodes, in which **Figure 4.21 (b,e)** (anodes in HPC/Se and NSHPC/Se cells) show rough surfaces with many coarse $Na_2Se$ agglomerations, suggesting severe parasitic reactions between dissolved sodium polyselenides and metallic sodium anode during discharge/charge cycles. In contrast, it is interesting to note that the surface of Na anode in i-PANI@NSHPC/Se cell (**Figure 4.21h**) is relatively smooth and no obvious aggregations can be observed. The less deposition of $Na_2Se$ on the anode side of i-PANI@NSHPC/Se cell indicates a suppressed shuttle effect. This can also be confirmed from the corresponding Se elemental mapping characterization shown in **Figure 4.21c,f** and **i**, in which obvious Se can be detected in the Na anodes of HPC/Se and NSHPC/Se cells, while only little amount of Se is observed in the Na anode of i-PANHI@NSHPC/Se battery. The Se elemental mapping results are consistent with the *ex situ* SEM images. Furthermore, **Figure 4.21d,g** and **j** show the glass fibres of the corresponding cells. The colour change after cycling is due to the polyselenides diffusion on the glass fibre separators. Compared to that of **Figure 4.21j,** the darker yellow separators in **Figure 4.21d** and **g** are consistent with the *ex situ* Raman, SEM and mapping results. Furthermore, the XPS spectra of i-PANI@NSHPC/Se after the 1st discharge and 1st charge are presented in 6. An obvious change can be observed during the first cycling, in which the Se $3d_{3/2}$ remain unchanged, but the Se $3d_{5/2}$ spectrum shifts to lower binding energy (from 55.35 eV to 55 eV) after fully discharging to 0.5V and then recovers back to the original state (from 55 eV to 55.35 eV) after charging to 3V. This suggests that the redox process of i-

PANI@NSHPC/Se electrode is highly reversible during cycling, which is also observed in a previous study in Li-Se battery [7].

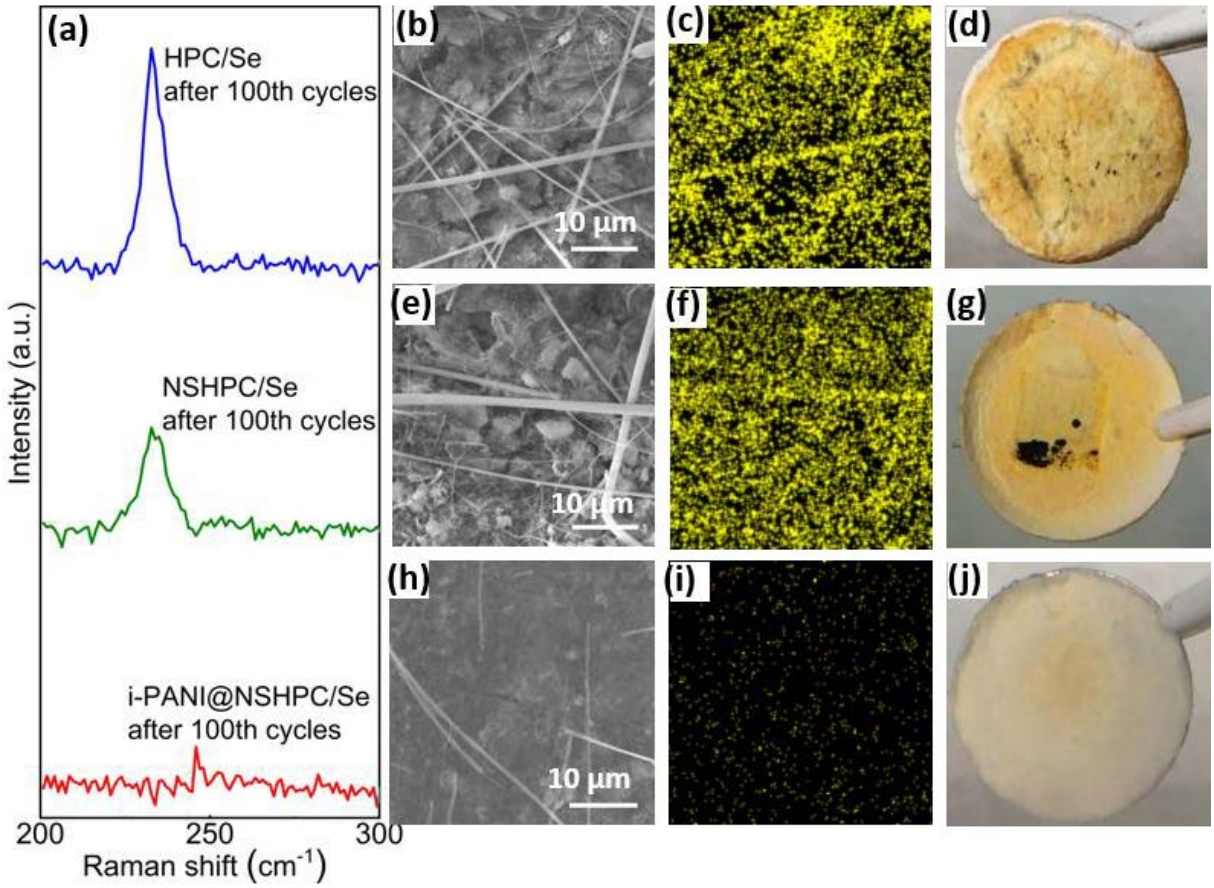


**Figure 4.21 (a)** *ex situ* Raman spectra of HPC/Se, NSHPC/Se and i-PANI@NSHPC/Se electrode after 100 cycle and their corresponding **(b,e,h)** SEM images of the Na anodes, **(c,f,i)** EDS mapping of Se element on Na anode, **(d,g,j)** digital images of glass fibre separators.

## 4.3.7 Proposed Mechanisms

**Figure 4.22** schematically illustrates the improved electrochemical performances of i-PANI@NSHPC/Se cathode. As shown in **Figure 4.22a** (HPC/Se), Se is confined in the micro/meso pores of the carbon matrix in the form of ring-structured $Se_8$ after infiltration. During cycling, the cyclic $Se_8$ converts to chain-like $Se_n$ [28, 40], which is reported to be more

thermodynamically stable and more conductive than the $Se_8$ rings [41]. However, the rapid capacity decay (67% of capacity retention after 100 cycles) implies that there is a serious 'shuttle effect', which could be due to the weak physical interactions between HPC and the chain-like $Se_n$. For NSHPC/Se in **Figure 4.22b**, it shows stable capacity retention at the beginning, but starts to dramatically fade after ~60 cycles. Compared to that of HPC/Se, the initial stable cycling performance of NSHPC/Se is attributed to the N, S dual-doped carbon host that can provide chemical adsorption for polylselenides. However, the fast capacity decay indicates that the dissolution of polyselenides occurs after certain cycles due to the unprotected NSHPC/Se composite. As a result, only 73% of capacity was retained over 100 cycles at 0.2 C. After coated with interconnected PANI (**Figure 4.22c**), the polyselenides are locked inside the carbon matrix and the polymer layer can function as a diffusion barrier. Furthermore, the interconnected structure connects each individual particles, which can enhance the conductivity, leading to ultra-stable cycling performance with high capacities. As presented in **Figure 4.22c**, 97.3% of the capacity was retained after 200 cycles. The enhanced electrochemical performances could be attributed to the synergistic effects of N, S dual doping and interconnected PANI coating, which provides both physical confinement and chemical binding for polyselenides.

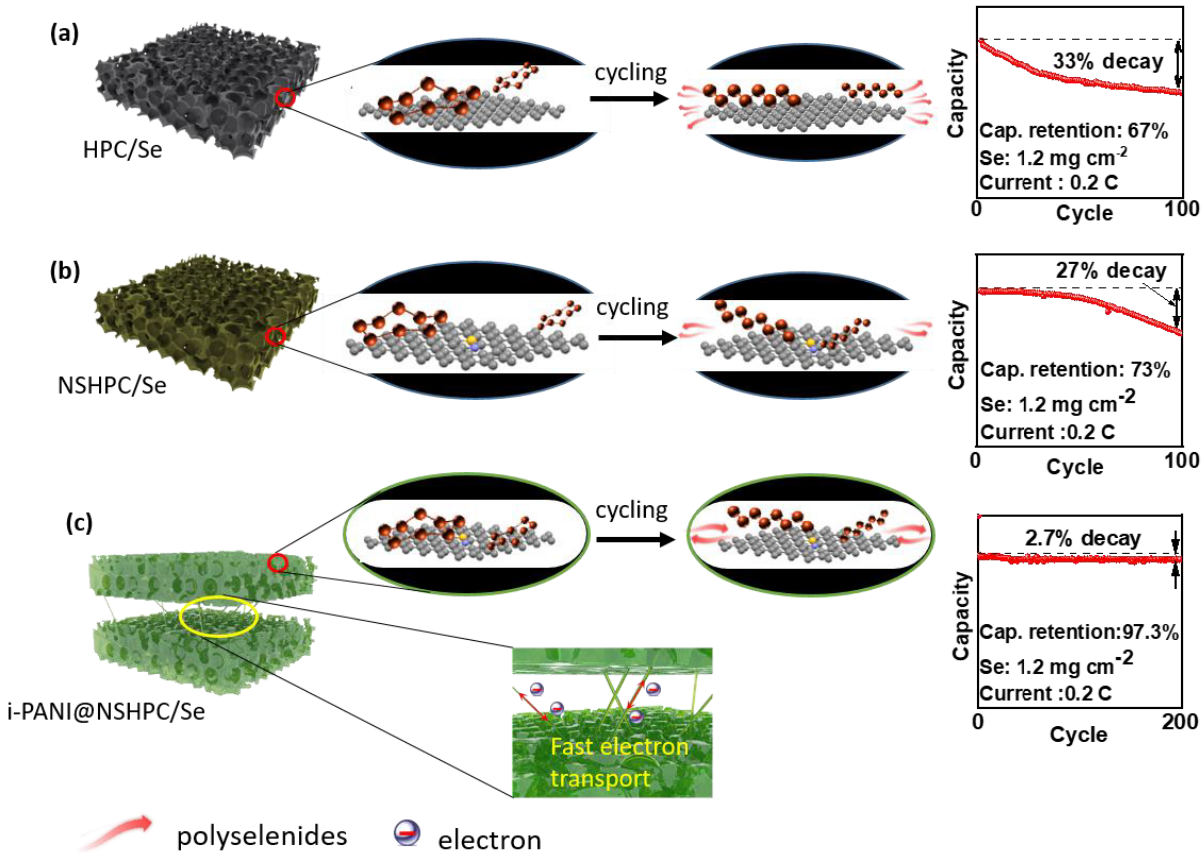


**Figure 4.22** Schematic illustration of the novel *in situ* polymerization coating for advanced Na-Se cathode structures. **(a)** Hierarchical porous carbon as a host for selenium (HPC/Se), which exhibits capacity decay upon the initial cycles. **(b)** N, S dual-doped hierarchical porous carbon as a host for Se (NSHPC/Se), which exhibits improved cycling performance in the initial cycles but undergoes fast capacity decay after certain cycles. **(c)** Interconnected PANI coating on NSHPC/Se (i-PANI@NSHPC/Se), which exhibits ultra-stable cycling performance.

## 4.4 Summary

In summary, we have developed N, S dual-doped hierarchical porous carbon/Se composite coated with interconnected PANI as a stable cathode material for Na-Se batteries. The rationally designed structure of i-PANI@NSHPC/Se composite enhances the areal mass

loading of Se and suppress the shuttle effect of polyselenides. The i-PANI@NSHPC/Se cathode also exhibits high conductivity for electrons and ions due to the hierarchical porous structure and interconnected conductive PANI networks. In addition, the DFT calculation result confirms that the N, S dual-doped porous carbon enhances the chemical adsorption between the N, S doped carbon matrix and $Na_xSe$ ($0<x\leq2$). Compared to HPC/Se and NSHPC/Se, i-PANI@NSHPC/Se enables an extremely stable cycling performance with 617 mAh $g^{-1}$ at 0.2 C over 200 cycles and an ultra-high rate capability with ~380 mAh $g^{-1}$ at 20 C. In addition, a high capacity retention over 1000 cycles has been achieved with high Se areal mass loading and high current density. The *ex situ* characterizations of Raman, XPS, SEM and EDS mapping also suggest that the polyselenides are effectively confined on the cathode side. The excellent electrochemical performances of i-PANI@NSHPC/Se can be attributed to the synergistic effect of N, S dual-doping and interconnected PANI coating. These include: a) the interconnected PANI structure provides high-speed pathways for electrons transport, leading to enhanced rate performance and high Se areal mass loading performance, b) the PANI coating layer provides a diffusion barrier for polyselenides, which effectively avoids the shuttle effect during cycling, c) the advantages of chemical adsorption between the carbon matrix and polyselenides can be maintained by protection of PANI layer upon long-term cycles, leading to high stability. The outstanding performance of i-PANI@NSHPC/Se cathode provides new insights into the development of advanced battery systems.

## 4.5 References


1. Liu, H.; Liu, X.; Li, W.; Guo, X.; Wang, Y.; Wang, G.; Zhao, D., Porous Carbon Composites for Next Generation Rechargeable Lithium Batteries. *Adv. Energy Mater.* **2017,** *7* (24), 1700283.

2. Tian, H.; Wang, T.; Zhang, F.; Zhao, S.; Wan, S.; He, F.; Wang, G., Tunable porous

carbon spheres for high-performance rechargeable batteries. *Journal of Materials Chemistry A* **2018,** *6* (27), 12816-12841.

3. Li, X. N.; Liang, J. W.; Li, X.; Wang, C. H.; Luo, J.; Li, R. Y.; Sun, X. L., High-performance all-solid-state Li–Se batteries induced by sulfide electrolytes. *Energy Environ. Sci* **2018,** *11*, 2828-2832.

4. Song, J.; Guo, X.; Zhang, J.; Chen, Y.; Zhang, C.; Luo, L.; Wang, F.; Wang, G., Rational Design of Free-Standing 3D Porous MXene/RGO Hybrid Aerogels as Polysulfides Reservoir for High-Energy Lithium-Sulfur Batteries. *J. Mater. Chem. A* **2019**.

5. Abouimrane, A.; Dambournet, D.; Chapman, K. W.; Chupas, P. J.; Weng, W.; Amine, K., A new class of lithium and sodium rechargeable batteries based on selenium and selenium-sulfur as a positive electrode. *J Am Chem Soc* **2012,** *134* (10), 4505-8.

6. Luo, C.; Xu, Y. H.; Zhu, Y. J.; Liu, Y. H.; Zheng, S. Y.; Liu, Y.; Langrock, A.; Wang, C. S., Selenium@Mesoporous Carbon Composite with Superior Lithium and Sodium Storage Capacity. *ACS Nano* **2013,** *7* (9), 8003-8010.

7. Ding, J.; Zhou, H.; Zhang, H.; Stephenson, T.; Li, Z.; Karpuzov, D.; Mitlin, D., Exceptional energy and new insight with a sodium–selenium battery based on a carbon nanosheet cathode and a pseudographite anode. *Energy Environ. Sci.* **2017,** *10* (1), 153-165.

8. Xu, X.; Zhou, D.; Qin, X.; Lin, K.; Kang, F.; Li, B.; Shanmukaraj, D.; Rojo, T.; Armand, M.; Wang, G., A room-temperature sodium-sulfur battery with high capacity and stable cycling performance. *Nat. Commun.* **2018,** *9* (1), 3870.

9. Li, Q.; Liu, H.; Yao, Z.; Cheng, J.; Li, T.; Li, Y.; Wolverton, C.; Wu, J.; Dravid, V. P.,

Electrochemistry of Selenium with Sodium and Lithium: Kinetics and Reaction Mechanism. *ACS Nano* **2016,** *10* (9), 8788-95.

10. Wang, H.; Jiang, Y.; Manthiram, A., Long Cycle Life, Low Self-Discharge Sodium-Selenium Batteries with High Selenium Loading and Suppressed Polyselenide Shuttling. *Adv. Energy Mater.* **2018,** *8* (7), 1701953.

11. Yang, X.; Wang, H.; Yu, D. Y. W.; Rogach, A. L., Vacuum Calcination Induced Conversion of Selenium/Carbon Wires to Tubes for High-Performance Sodium-Selenium Batteries. *Adv. Funct. Mater.* **2018,** *28* (8), 1706609.

12. Jin, J.; Tian, X.; Srikanth, N.; Kong, L. B.; Zhou, K., Advances and challenges of nanostructured electrodes for Li–Se batteries. *Journal of Materials Chemistry A* **2017,** *5* (21), 10110-10126.

13. Zhang, J.; Xu, Y.; Fan, L.; Zhu, Y.; Liang, J.; Qian, Y., Graphene–encapsulated selenium/polyaniline core–shell nanowires with enhanced electrochemical performance for Li–Se batteries. *Nano Energy* **2015,** *13*, 592-600.

14. Yuan, B.; Sun, X.; Zeng, L.; Yu, Y.; Wang, Q., A Freestanding and Long-Life Sodium-Selenium Cathode by Encapsulation of Selenium into Microporous Multichannel Carbon Nanofibers. *Small* **2018,** *14* (9), 1703252.

15. Wu, F.; Yushin, G., Conversion cathodes for rechargeable lithium and lithium-ion batteries. *Energy Environ. Sci.* **2017,** *10* (2), 435-459.

16. Jayaprakash, N.; Shen, J.; Moganty, S. S.; Corona, A.; Archer, L. A., Porous hollow carbon@sulfur composites for high-power lithium-sulfur batteries. *Angew. Chem. Int. Ed.* **2011,** *50* (26), 5904-8.

17. Schuster, J.; He, G.; Mandlmeier, B.; Yim, T.; Lee, K. T.; Bein, T.; Nazar, L. F., Spherical ordered mesoporous carbon nanoparticles with high porosity for lithium-sulfur batteries. *Angew. Chem. Int. Ed.* **2012,** *51* (15), 3591-5.

18. Tang, C.; Zhang, Q.; Zhao, M. Q.; Huang, J. Q.; Cheng, X. B.; Tian, G. L.; Peng, H. J.; Wei, F., Nitrogen-doped aligned carbon nanotube/graphene sandwiches: facile catalytic growth on bifunctional natural catalysts and their applications as scaffolds for high-rate lithium-sulfur batteries. *Adv. Mater.* **2014,** *26* (35), 6100-5.

19. Ding, J.; Zhou, H.; Zhang, H.; Tong, L.; Mitlin, D., Selenium Impregnated Monolithic Carbons as Free-Standing Cathodes for High Volumetric Energy Lithium and Sodium Metal Batteries. *Adv. Energy Mater.* **2018,** *8* (8), 1701918.

20. Zeng, L.; Zeng, W.; Jiang, Y.; Wei, X.; Li, W.; Yang, C.; Zhu, Y.; Yu, Y., A Flexible Porous Carbon Nanofibers-Selenium Cathode with Superior Electrochemical Performance for Both Li-Se and Na-Se Batteries. *Adv. Energy Mater.* **2015,** *5* (4), 1401377.

21. Xu, J.; Su, D.; Zhang, W.; Bao, W.; Wang, G., A nitrogen–sulfur co-doped porous graphene matrix as a sulfur immobilizer for high performance lithium–sulfur batteries. *J. Mater. Chem. A* **2016,** *4* (44), 17381-17393.

22. Zhao, X.; Yin, L.; Zhang, T.; Zhang, M.; Fang, Z.; Wang, C.; Wei, Y.; Chen, G.; Zhang, D.; Sun, Z.; Li, F., Heteroatoms dual-doped hierarchical porous carbon-selenium composite for durable Li–Se and Na–Se batteries. *Nano Energy* **2018,** *49*, 137-146.

23. Li, G.-C.; Li, G.-R.; Ye, S.-H.; Gao, X.-P., A Polyaniline-Coated Sulfur/Carbon Composite with an Enhanced High-Rate Capability as a Cathode Material for Lithium/Sulfur Batteries. *Adv. Energy Mater.* **2012,** *2* (10), 1238-1245.

24. Yang, Y.; Yu, G. H.; Cha, J. J.; Wu, H.; Vosgueritchian, M.; Yao, Y.; Bao, Z. A.; Cui, Y., Improving the Performance of Lithium-Sulfur Batteries by Conductive Polymer Coating. *ACS Nano* **2011,** *5* (11), 9187-9193.

25. Zhou, W.; Yu, Y.; Chen, H.; DiSalvo, F. J.; Abruna, H. D., Yolk-shell structure of polyaniline-coated sulfur for lithium-sulfur batteries. *J. Am. Chem. Soc.* **2013,** *135* (44), 16736-43.

26. Wang, B.; Zhang, J.; Xia, Z.; Fan, M.; Lv, C.; Tian, G.; Li, X., Polyaniline-coated selenium/carbon composites encapsulated in graphene as efficient cathodes for Li-Se batteries. *Nano Research* **2018,** *11* (5), 2460-2469.

27. Yang, W.; Yang, W.; Ding, F.; Sang, L.; Ma, Z.; Shao, G., Template-free synthesis of ultrathin porous carbon shell with excellent conductivity for high-rate supercapacitors. *Carbon* **2017,** *111*, 419-427.

28. Yang, C. P.; Xin, S.; Yin, Y. X.; Ye, H.; Zhang, J.; Guo, Y. G., An advanced selenium-carbon cathode for rechargeable lithium-selenium batteries. *Angew Chem Int Ed Engl* **2013,** *52* (32), 8363-7.

29. Yang, J.; Zhou, X.; Wu, D.; Zhao, X.; Zhou, Z., S-Doped N-Rich Carbon Nanosheets with Expanded Interlayer Distance as Anode Materials for Sodium-Ion Batteries. *Adv. Mater.* **2017,** *29* (6).

30. Yao, Y.; Chen, M.; Xu, R.; Zeng, S.; Yang, H.; Ye, S.; Liu, F.; Wu, X.; Yu, Y., CNT Interwoven Nitrogen and Oxygen Dual-Doped Porous Carbon Nanosheets as Free-Standing Electrodes for High-Performance Na-Se and K-Se Flexible Batteries. *Adv. Mater.* **2018**, 1805234.

31. Niu, S.; Lv, W.; Zhou, G.; He, Y.; Li, B.; Yang, Q. H.; Kang, F., N and S co-doped porous carbon spheres prepared using L-cysteine as a dual functional agent for high-performance lithium-sulfur batteries. *Chem. Commun. (Camb)* **2015,** *51* (100), 17720-3.

32. Cai, Q.; Li, Y.; wang, L.; Li, Q.; Xu, J.; Gao, B.; Zhang, X.; Huo, K.; Chu, P. K., Freestanding hollow double-shell Se@CN x nanobelts as large-capacity and high-rate cathodes for Li-Se batteries. *Nano Energy* **2017,** *32*, 1-9.

33. Liu, Y.; Si, L.; Du, Y.; Zhou, X.; Dai, Z.; Bao, J., Strongly Bonded Selenium/Microporous Carbon Nanofibers Composite as a High-Performance Cathode for Lithium–Selenium Batteries. *J. Phys. Chem. C* **2015,** *119* (49), 27316-27321.

34. Ma, D.; Li, Y.; Yang, J.; Mi, H.; Luo, S.; Deng, L.; Yan, C.; Zhang, P.; Lin, Z.; Ren, X.; Li, J.; Zhang, H., Atomic layer deposition-enabled ultrastable freestanding carbon-selenium cathodes with high mass loading for sodium-selenium battery. *Nano Energy* **2018,** *43*, 317-325.

35. Luo, C.; Wang, J.; Suo, L.; Mao, J.; Fan, X.; Wang, C., In situ formed carbon bonded and encapsulated selenium composites for Li–Se and Na–Se batteries. *Journal of Materials Chemistry A* **2015,** *3* (2), 555-561.

36. Zeng, L.; Wei, X.; Wang, J.; Jiang, Y.; Li, W.; Yu, Y., Flexible one-dimensional carbon–selenium composite nanofibers with superior electrochemical performance for Li–Se/Na–Se batteries. *J. Power Sources* **2015,** *281*, 461-469.

37. Xu, Q.; Liu, T.; Li, Y.; Hu, L.; Dai, C.; Zhang, Y.; Li, Y.; Liu, D.; Xu, M., Selenium Encapsulated into Metal-Organic Frameworks Derived N-Doped Porous Carbon Polyhedrons as Cathode for Na-Se Batteries. *ACS Appl. Mater. Interfaces* **2017,** *9* (47), 41339-41346.

38. Sun, F.; Li, Y.; Wu, Z.; Liu, Y.; Tang, H.; Li, X.; Yue, Z.; Zhou, L., In situ reactive coating of metallic and selenophilic Ag2Se on Se/C cathode materials for high performance Li–Se batteries. *RSC Advances* **2018,** *8* (57), 32808-32813.

39. Pang, Q.; Tang, J.; Huang, H.; Liang, X.; Hart, C.; Tam, K. C.; Nazar, L. F., A nitrogen and sulfur dual-doped carbon derived from polyrhodanine@cellulose for advanced lithium-sulfur batteries. *Adv. Mater.* **2015,** *27* (39), 6021-8.

40. Liu, J.; Lan, D.; Huang, X.; Zhang, F.; Huang, A.; Xiao, Y.; Zhao, Z.; Liu, L.; Ke, X.; Shi, Z.; Guo, Z., GO@Se@Ni Cathode Materials for Lithium-Selenium Battery. *Journal of The Electrochemical Society* **2018,** *166* (3), A5259-A5264.

41. Xu, G.-L.; Liu, J.; Amine, R.; Chen, Z.; Amine, K., Selenium and Selenium–Sulfur Chemistry for Rechargeable Lithium Batteries: Interplay of Cathode Structures, Electrolytes, and Interfaces. *ACS Energy Lett.* **2017,** *2* (3), 605-614.

# Chapter 5 Interface engineering of MXene composite separator for high-performance Li-Se and Na-Se batteries

## 5.1 Introduction

The soaring demand for electric vehicles and grid-scale energy storage today necessitates high-capacity rechargeable batteries.[1-6] As one of the chalcogen elements, selenium (Se) has been widely investigated as a cathode material in alkali-metal batteries due to its high theoretical capacity (678 mAh $g^{-1}$) and comparable volumetric capacity to the alkali metal-sulfur batteries (Se, 3268 mAh $cm^{-3}$ vs S, 3467 mAh $cm^{-3}$).[7-9] The good conductivity of Se (1 × $10^{-3}$ S $m^{-1}$) endows it highly reactive with alkali metals through a conversion type reaction: $2M^{+} + Se + 2e^{-} \leftrightarrow M_2Se$, M=Li, Na.[10-11] However, the development of metal-Se batteries has been blocked by the severe shuttle effect of polyselenides, particularly in ether-based electrolyte, where the polyselenides diffuse across the separator and react with the metal anode.[12-13] Tremendous efforts have been devoted to the design of advanced cathode host materials to mitigate the shuttle effect.[14-15] These designed cathode strategies include: employing porous carbon materials as the hosts;[7, 16-19] coating the cathode materials with graphene, metal oxide or conductive polymers;[20-24] and hetero-atoms doping.[25-27] However, these cathode engineering would inevitably reduce the mass ratio of selenium by introducing additional components, leading to decreased energy density.[28]

Recently, functional separators have been prepared to inhibit the shuttle effect in Se or S based batteries.[17, 29-34] For example, MXenes ($M_{n+1}X_nT_x$, where M = transition metal, X = carbon/nitrogen, n = 1, 2 and 3, $T_x$ represents surface functional groups) modified separators have been proved to be effective in suppressing the shuttle effect due to their anisotropic shape and large 2D dimensions that increases the diffusion pathway of

polysulfide/polyselenide species.[35-37] In addition, MXene shows strong adsorption to polysulfides due to the Lewis acid-base interaction between polysulfides and Ti sites, [38-39] which may also work for polyselenides. Nazar and co-workers have shown that the surface environment on MXene enhances such Lewis acid-base chemisorption via thiosulfate formation.[38] However, this enhanced adsorption undergoes a two-step process with sluggish kinetics. Although the shuttle effect can be mitigated, the battery showed slow redox reaction, especially under high current densities. In addition, the MXene nanosheets also suffer from restacking and poor electrolyte affinities due to the van der Waals forces and rich hydrophilic surface groups (-OH and –F), respectively.[40-41] It is well known that the hydrophilic groups on MXene have low compatibility to organic electrolyte.[42] The inferior separator-electrolyte contact will lead to a poor solid-electrolyte interface and slow electrolyte infiltration process.[43]

Herein, we developed a novel self-assembled cetrimonium bromide (CTAB)/carbon nanotube (CNT)/$Ti_3C_2T_x$ MXene composite modified polypropylene (PP) (CCNT/MXene/PP) separator with tuned separator-electrolyte interface properties for both Li-Se and Na-Se batteries. The adsorption property of MXene to polyselenides can be greatly enhanced due to the synergetic Lewis acid-base interaction between CTAB/MXene and negatively charged polyselenide anions, which have been proved by X-ray photo electron spectroscopy (XPS) and density functional theory (DFT) calculations. *In situ* permeation experiments were conducted for the first time to test the electrochemical behaviour of Li-Se batteries and the suppressed shuttle effect with CCNT/MXene/PP separator. Meanwhile, the enlarged interlayer spacing due to the intercalation of CTAB molecules between MXene layers is beneficial for fast ionic transport. CNT network was incorporated into the MXene nanosheets to further improve the electrolyte penetration and prevent restacking of the delaminated MXene nanosheets. Owing to the flexible feature of 1D-CNT and 2D MXene materials, ultra-

thin CCNT/MXene/PP separators with low areal mass loadings of ~0.09 mg $cm^{-2}$ have been obtained. When the CCNT/MXene/PP separator is applied in Li-Se batteries using commercial carbon black/Se cathode (high Se loading of 73.37 wt%), the battery delivered an outstanding cyclability with a low capacity decay of 0.05% per cycle over 500 cycles at 1 C. The free-standing carbon cloth/Se cathode with a high Se areal mass loading of 5.1 mg $cm^{-2}$ still maintained a capacity of 485 mAh $g^{-1}$ after 100 cycles. Furthermore, the functionalized separators also perform well in Na-Se batteries, achieving a high capacity retention of 72.6% upon 300 cycles.

## 5.2 Experimental section

### 5.2.1 Materials

Hexadecyltrimethylammonium bromide (CTAB, ≥99%), isopropyl alcohol (≥98%) were purchased from Sigma-Aldrich. All chemicals were used as received without further purification.

### 5.2.2 Preparation of MXene ($Ti_3C_2T_X$) modified PP separator (MXene/PP)

The MXene ($Ti_3C_2T_x$) was prepared by etching the MAX ($Ti_3AlC_2$) phase material according to our previous work. Typically, 0.5 g of lithium fluoride was dissolved into 5 ml of HCl (6.5 M) solution under stir, followed by the slow addition of MAX powder. Then, the mixture was stirred for 2 days to ensure complete etching. The resulting MXene ($Ti_3C_2T_x$) suspension was then obtained by washing and centrifuge several times. A diluted MXene suspension (0.2 mg/ml) was prepared for future use. 5 ml of the MXene suspension (0.2 mg/ml) was first sonicated for 30 min and used for preparing the MXene/PP separator by a

filtration method through a Celgard 3501 separator with a diameter of 3.6 cm. During this process, Ar atmosphere was introduced to avoid the oxidation of MXene.

### 5.2.3 Preparation of CCNT/PP, CNT/ PP and CCNT/MXene/PP separators

The cetrimonium bromide (CTAB) grafted CNT (CCNT) was first prepared to form a uniform suspension. Generally, a CTAB (>99%, Sigma Aldrich) solution (0.5 wt%) was prepared by dissolving 0.5 mg CTAB in 99.5 mg DI water with vigorous stir. 50 mg of the commercial CNT powder was then added into 50 ml of CTAB solution, followed by a strong probe sonication process for 30 min to get uniform CNT suspension. After that, the suspension was centrifuged to remove excess of CTAB and re-dispersed in distilled water to form a stable CNT suspension with a concentration of 0.2 mg $ml^{-1}$. To prepare the CCNT/PP separator, 5 ml of the CTAB-CNT suspension was first probe-sonicated and then filtered through a Celgard separator. To figure out the role of CTAB on the electrochemical performance, CNT was also dispersed into isopropyl alcohol (CNT/IPA). The separator CNT/PP was prepared by filtering the CNT/IPA suspension (5ml, 0.2 mg $ml^{-1}$) through the Celgard separator. To prepare the CCNT/MXene/PP separator, 5 ml of MXene suspension (0.2 mg $ml^{-1}$) was slowly added into 10 ml of CCNT suspension (0.2 mg $ml^{-1}$) under probe sonication, followed by stirring overnight with additional drop of CTAB solution. After that, the uniform CCNT/MXene suspension was obtained and 5 ml of the suspension was filtered through Celgard separator to get the CCNT/MXene/PP separator.

## 5.2.4 Preparation of cathode electrode

200 mg of carbon black was mixed with 600 mg of selenium by grinding. Then, the mixture was transferred to a tube furnace in a glass vial and heated at 260 °C for 12 h under $N_2$ atmosphere with a heating rate of 2 °C/min. The final product was collected and labelled as CB/Se. The cathode electrodes were prepared by a conventional slurry coating. The slurry was prepared by mixing the CB/Se composite, carbon black and PVDF with a mass ratio of 8:1:1 in the NMP solvent. The slurry was then spread onto the Al foil by a doctor blade and dried in a vacuum oven at 60 °C for 12 h. The average areal mass loading of Se on each electrode is 1.8 mg $cm^{-2}$. To prepare the free standing cathode, Se powder was spread on the surface of carbon cloth in a mass ratio of 1:1. Then the carbon cloth-Se composite was heat treated at 260 °C for 12 h, the resultant product was collected as the CC/Se cathode material with a high areal Se mass loading of 5.1 mg $cm^{-2}$.

## 5.2.5 Materials Characterization

The morphology investigations were examined with a field emission scanning electron microscopy (FESEM, Zeiss Supra 55VP) and transmission electron microscopy (TEM, JEOL JEM-2011). The X-ray diffraction was employed to investigate the phase information with a Bruker D8 Discover X-ray diffractometer using Cu Kα radiation (λ = 0.15406 nm). Raman spectra were obtained using a Renishaw inVia Raman spectrometer system (Gloucestershire, UK) equipped with a Leica DMLB microscope (Wetzlar, Germany). XPS measurements were conducted using the ESCALAB250Xi (Thermo Scientific, UK), which is equipped with monochromated Al Kα. Brunauer-Emmett-Teller (BET) and Barrer-Joyner-Halenda (BJH) method were employed to determine the porous structure of the samples with a Micromeritics 3 Flex analyser (Micromeritics Instruments Corporation, USA). The thermogravimetric

analyser (TGA, 2960 SDT system) was used to determine the content of selenium in the composite under $N_2$ atmosphere up to 800 °C with a heating rate of 10 °C/min.

## 5.2.6 Electrochemical Measurements

The electrochemical performances with different separators were tested using 2032-type coin cells which were assembled in Ar-filled glove box ($O_2$<0.1 ppm, $H_2O$<0.1 ppm). For Li-Se batteries, the coin cells consist cathode material (CB/Se), lithium foil as the counter electrode and modified separators. The electrolyte was 1 M lithium bis-trifluoromethane sulfonylimide (LiTFSI) in 1,3-dioxolane and 1,2-dimethoxyethane (1/1, v/v) with 2 wt% $LiNO_3$. The galvanostatic charge and discharge profiles were obtained using a LAND CT2001A system in the range of 1.0-3.0 V and the specific capacity is calculated based on the mass of selenium. The cyclic voltammograms (CV) and electrochemical impedance spectroscopy (EIS) measurements were collected with a VMP3 multichannel potentiostat. The CV measurements for Li-Se batteries were performed at a scan rate of 0.1-0.5 mV $s^{-1}$ in the range of 1.0-3.0 V (vs. $Li/Li^+$). The EIS tests were performed in the frequency range from 100 kHz to 0.01 Hz. For Na-Se batteries, sodium foil was used as the counter electrode and the electrolyte consists of 1 M $NaClO_4$ in ethylene carbonate-diethyl carbonate (EC:DEC=1:1, v:v). The galvanostatic charge and discharge profiles were conducted in the range of 0.5-3.0 V. The CV tests were conducted in the range of 0.5-3.0 V at the scan rate of 0.1 mV $s^{-1}$.

## 5.2.7 Preparation of the *in situ* permeation experiment

*In situ* permeation experiment were conducted with an H-type cell in Li-Se batteries. The H-type cell consists of a cathode (CB/Se), an anode (Li metal) on each side of the cell and a separator (PP or CCNT/MXene/PP separators) in between. The H-type cell was assembled with the electrolyte (0.5M LiTFSI in DOL/DME) and tightly sealed to avoid any contact with

air in the glovebox. The assembled H-type cell was then taken out for the galvanostatic charge/discharge test at a low current density of 0.05 C.

## 5.2.8 Transference number of lithium ions

The lithium ion transference number (LTN) for the cells with different separators was investigated with chronoamperometry by using the CHI electrochemical working station at a constant step potential of 10 mV. The coin cells (CR2032) were assembled with the separators sandwiched between two lithium metal electrodes. The LTN was then calculated based on the ratio of steady state current to the initial state current according to the equation:

$$t_{Li+} = I_s/I_o \qquad \text{(Equation 1)}$$

where $t_{Li+}$ represents the transference number, $I_s$ and $I_o$ represent the current at the steady state and initial state, respecitively.

**Lithium ion diffusion coefficient:** The lithium ion diffusion coefficients for the cells with various separators were calculated from the slop of the linear plot of the peak current ($I_p$) versus the square root of the scan rate ($V^{1/2}$) based on a series of cyclic voltammograms at the scan rates from 0.1-0.5 mV $s^{-1}$ according to the Randles-Sevick equation:

$$I_p = 2.69 \times 10^5 \times n^{1.5} \times A \times {D_{Li^+}}^{0.5} \times C_{Li} \times \nu^{0.5} \qquad \text{(Equation 2)}$$

where $D_{Li}^+$ represents the lithium ion diffusion coefficient ($cm^2$ $s^{-1}$), $I_p$ is the peak current (A), n stands for the number of electrons involved in the reaction (n=2 for Li-Se batteries), A is the electrode area ($cm^2$), $C_{Li}$ and ν represent the lithium ion concentration (mol $L^{-1}$) and scan rate (V $s^{-1}$), respectively.

## 5.2.9 Computation methods

All calculations were carried out by using the projector augmented wave method in the framework of the density functional theory (DFT), as implemented in the Vienna *ab-initio* Simulation Package (VASP). The generalized gradient approximation (GGA) and Perdew–Burke–Ernzerhof (PBE) exchange functional was used. Structural relaxation calculations were performed by using the spin-polarized GGA method. The plane-wave energy cutoff was set to 500 eV. The convergence criterions of energy and force calculations were set to $10^{-5}$ eV/atom and 0.01 eV $Å^{-1}$, respectively. To explore the interactions between the polyselenide $Li_2Se_n$ (n=4 and 6) and substrates, including the carbon nanotubes, $Ti_3C_2T_x$ MXene with -F and -OH groups, CATB, and CATB modified $Ti_3C_2T_x$ MXene, the adsorption energies of the polyselenide $Li_2Se_n$ (n=4 and 6) on the above substrate surfaces were calculated. A vacuum region of 15 Å is applied to avoid interactions between the neighboring configurations. DFT-D3 method was used to account for the vdW interactions between organic molecule and substrate surface. Herein, the adsorption energies ($E_a$) were calculated by the energy difference of the system after and before adsorption: $E_a = E_{(Li2Sen\text{-}substrate)} - E_{Li2Sen} - E_{substrate}$, where $E_{(Li2Sen\text{-}substrate)}$, $E_{Li2Sen}$ and $E_{substrate}$ represent the DFT energies of the polyselenide $Li_2Se_n$ (n=4 and 6) molecule adsorption on the substrate surfaces, the energy of an isolated $Li_2Se_n$ molecule and the energy of the clean substrate surface.

## 5.3 Results and Discussion

### 5.3.1 Morphology and Structure

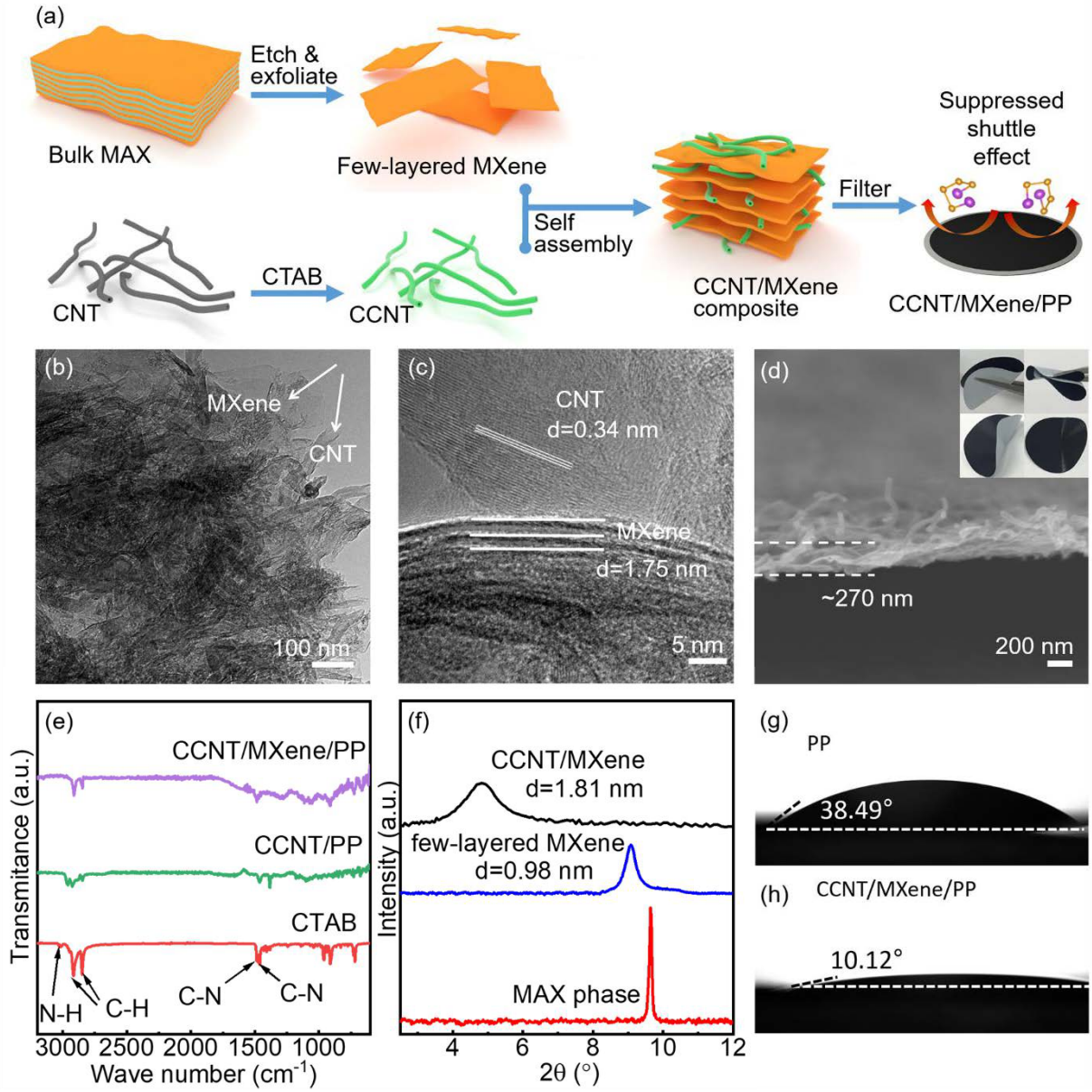


**Figure 5.1 (a)** Schematic preparation of CCNT/MXene/PP separator. **(b)** TEM image of CCNT/MXene composite. **(c)** HRTEM image of CCNT/MXene/PP composite. **(d)** Cross section SEM of CCNT/MXene/PP separator with folding/recovery test (inset). **(e)** FT-IR spectra of CTAB, CCNT/PP and CCNT/MXene/PP separators. **(f)** XRD of MAX phase, few-

layered Mxene nanosheets and CCNT/MXene composite. **(g, h)** Electrolyte wettability tests of PP and CCNT/MXene/PP separators, respectively, with LiTFSI in DOL/DME (1/1 by volume, 2 wt% $LiNO_3$).

**Figure 5.1a** shows the preparation of the CCNT/MXene/PP separators. In the first step, MXene ($Ti_3C_2T_x$) nanosheets were prepared by etching $Ti_3AlC_2$ MAX phase with LiF and HCl followed by washing and sonication to form a stable suspension. The etched multi-layered and few-layered MXene nanosheets were investigated by the scanning electron microscopy (SEM, **Figure 5.2**). The multi-layered MXenes show a typical accordion-like structure and the few-layered MXenes present a 2D nanosheet morphology. Secondly, the CTAB functionalized CNTs (CCNT) were prepared via a sonication-assisted solution reaction. CTAB is a cationic surfactant that have shown strong Lewis acid-base interaction to polysulfides/polyselenides.[44] The MXene suspension was then mixed with CCNT suspension in a mass ratio of 1:2 via probe sonication. The self-assembled CCNT and MXene composites were obtained through the electrostatic interactions, which effectively prevents the restacking of MXene nanosheets. After that, a small amount of CTAB solution was dropped into the mixture under probe-sonication to form a stable suspension. The CCNT/MXene/PP separators were then prepared by simply filtering the uniform CCNT/MXene suspension onto the PP separators.

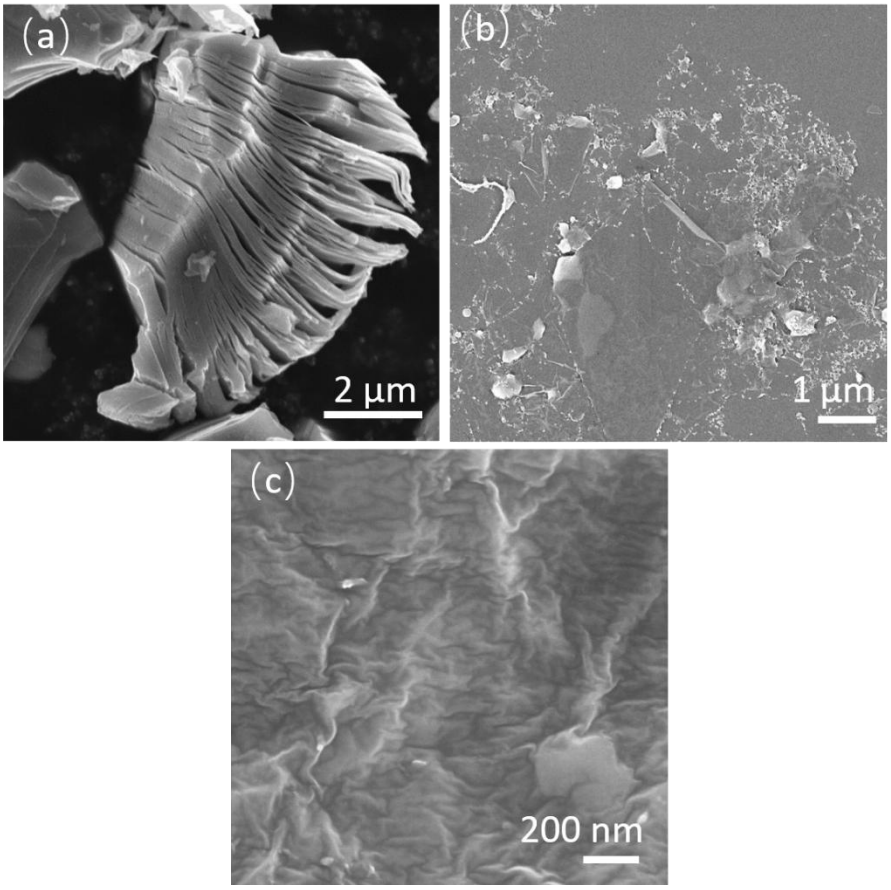


**Figure 5.2 (a)** SEM image of multi-layered $Ti_3C_2T_x$ MXene etched from the MAX precursor, **(b, c)** few-layered MXene nanosheets.

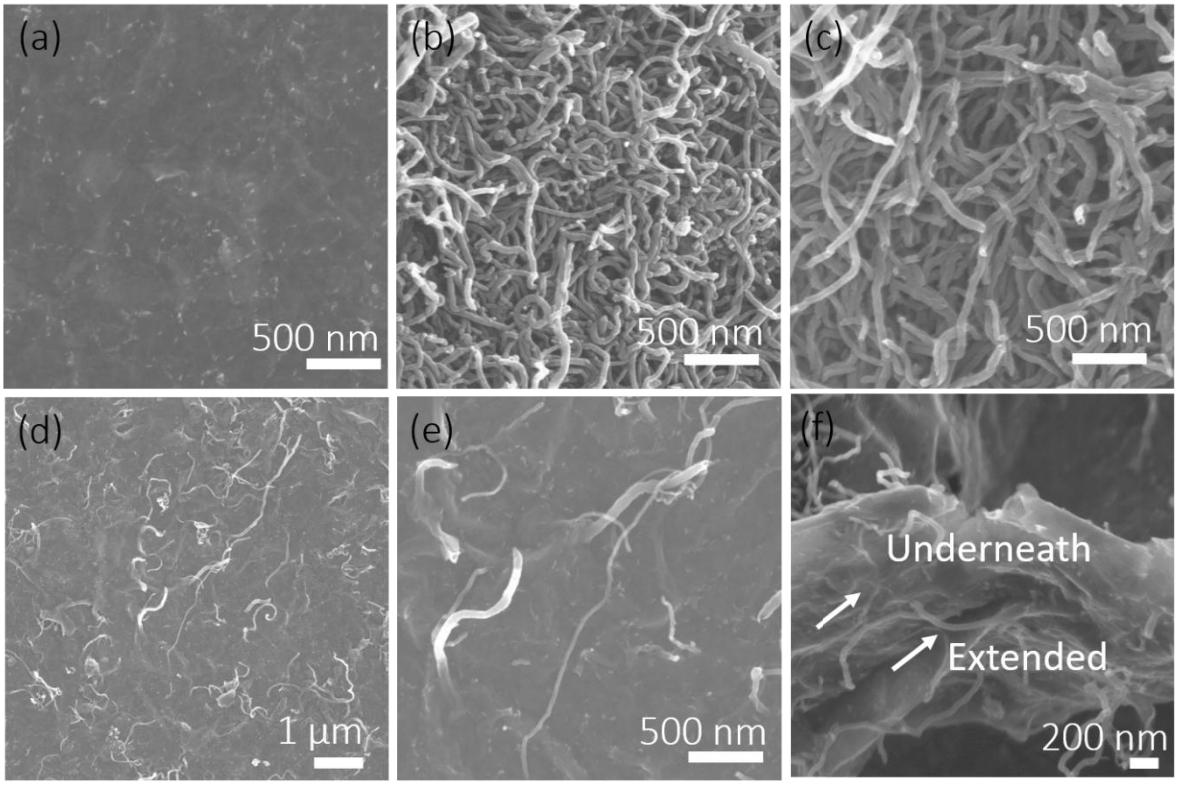


**Figure 5.3** Top view SEM images of **(a)** MXene/PP, **(b)** CCNT/PP, **(c)** CNT/PP and **(d-f)** CCNT/MXene/PP separators.

For comparison, MXene/PP, CCNT/PP and CNT/PP (without CTAB modification) separators were also prepared via a similar filtration process as control samples (**Figure 5.3 a-c**). **Figure 5.3 (d-f)** show that CNT extends outward the surface of CCNT/MXene/PP separator with interconnected networks, which provides more active sites for polyselenides precipitation.

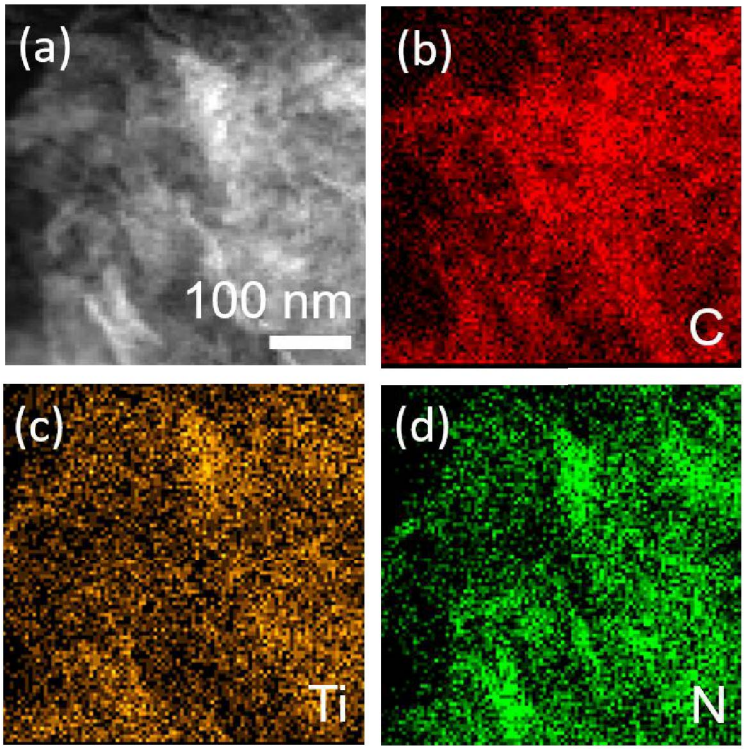


**Figure 5.4 (a)** Scanning transmission electron microscopy (STEM) and elemental mapping images of **(b)** C, **(c)** Ti and **(d)** N in a selected region of CCNT/MXene composite.

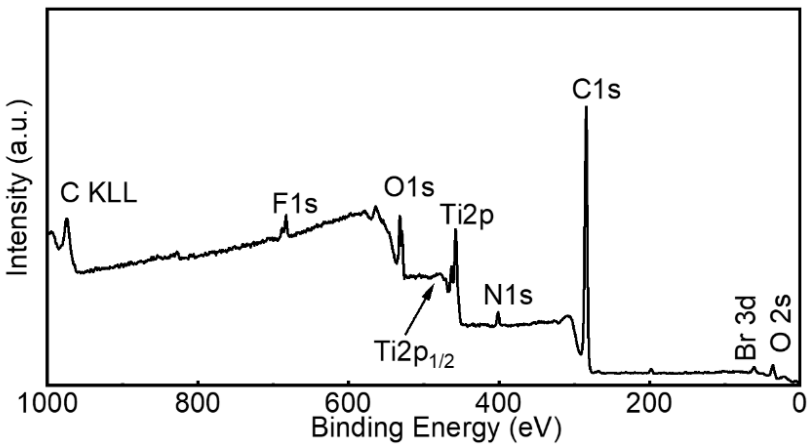


**Figure 5.5** XPS survey spectrum of CCNT/MXene composite on the CCNT/MXene/PP separator.

The transmission electron microscopy (TEM) image of CCNT/MXene composite (**Figure 5.1b**) shows that the CCNT and MXene are stacked together. The scanning transmission electron microscopy (STEM) image of the CCNT/MXene composite and the corresponding energy-dispersive X-ray (EDX) elemental mapping results demonstrate the uniform distributions of CTAB, CNT and MXene in the composite (**Figure 5.4**). The XPS spectra of CCNT/MXene composite in **Figure 5.5** also confirms the co-existence of C (285 eV), Ti (453 eV), N (399 eV), O (532 eV) and F (682 eV) elements and their corresponding elemental composition (**Table 5.1**). The CTAB is approximately 4.68 wt% based on the elemental composition. The high-resolution TEM (HRTEM) image in **Figure 5.1c** indicates the successful combination of CCNT and MXene, in which the CNT has a lattice distance of 0.34 nm and the MXene has an enlarged interlayer spacing of ~1.75 nm, which could be attributed to the intercalation of CTAB into the MXene layers.[42] The cross section image of CCNT/MXene/PP separator in **Figure 5.1d** shows that the CCNT/MXene on PP separator is ultra-thin with a thickness of ~270 nm. The thin-layered functional composite with a small mass loading on the separator is preferable for high energy density batteries. The folding/recovery test (inset of **Figure 5.1d**) shows that the CCNT/MXene/PP separator can recover to its original shape after being bended and folded, demonstrating a high mechanical stability, excellent flexibility and robustness.

**Table 5.1** Element composition in CCNT/MXene composite from XPS analysis

| Elements | wt. % | at. % |
|---|---|---|
| C | 59.04 | 79.22 |
| Ti | 28.26 | 9.48 |
| O | 5.89 | 5.93 |
| F | 5.92 | 5.02 |
| N | 0.18 | 0.21 |
| Br | 0.70 | 0.14 |

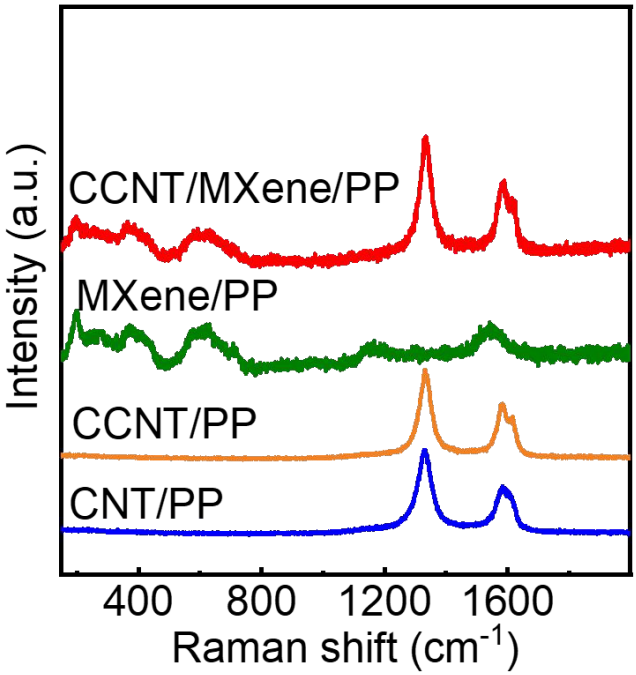


**Figure 5.6** Raman spectra of CNT/PP, CCNT/PP, MXene/PP and CCNT/MXene/PP separators.

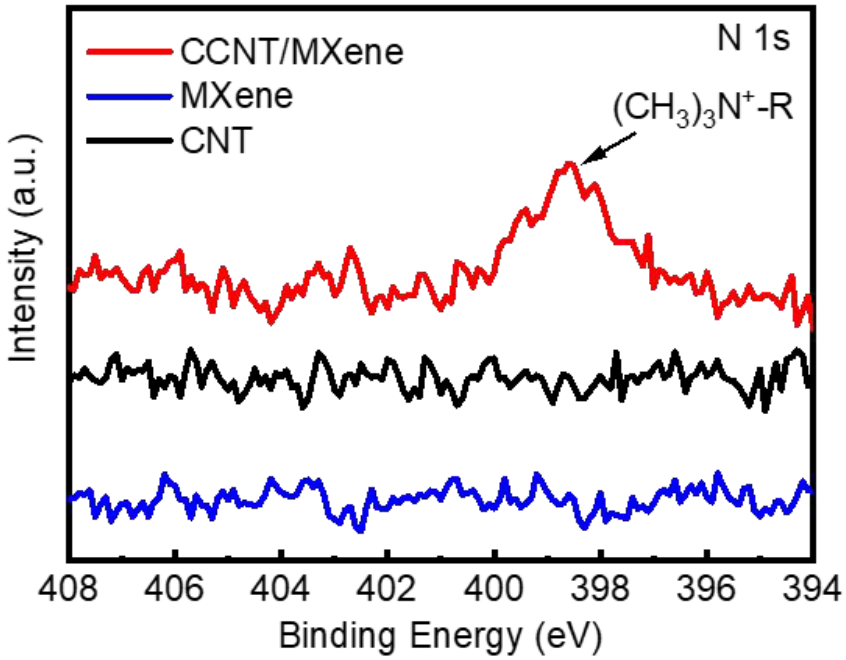


**Figure 5.7** N 1s XPS spectra of CNT, MXene and CCNT/MXene composite.

The Raman spectroscopy (**Figure 5.6**) has been employed to investigate the structure of the as-prepared separators. For the MXene/PP separator, it shows typical $Ti_3C_2T_x$ peaks at around 201.2, 380.3 and 646 $cm^{-1}$.[33] The two broad peaks at 1330 and 1584 $cm^{-1}$ in the CNT/PP separator are attributed to the disordered D-band and graphitized G-band of carbon, respectively.[22] In addition, CCNT has the similar Raman spectrum to the pristine CNTs, indicating that CTAB functionalization does not change the structure of CNTs. The CCNT/MXene/PP separator shows combined peaks of CCNT and MXene, suggesting the uniform mixing of CCNT and MXene composite. Furthermore, to confirm the functionalization of CTAB on the CCNT/PP and CCNT/MXene/PP separators, we measured the Fourier transform infrared spectroscopy (FT-IR) and XPS spectra. In **Figure 5.1e**, the peaks at ~2917.8 and 2848.4 $cm^{-1}$ in CTAB are attributed to the C-H symmetrical and asymmetric stretching vibrations, respectively. After mixing CNT suspension with CTAB solution, the obtained CCNT composite also shows the two characteristic bands at ~2917.7 and 2848.7 $cm^{-1}$, indicating the successful functionalization of CTAB on CNT surface. For the CCNT/MXene/PP separator, the above-mentioned two peaks both right shifted to lower wave numbers at 2912.1 and 2846.4 $cm^{-1}$, respectively. This peak shift could be attributed to the insertion of $CTA^+$ chains into the interlayers of MXene nanosheets.[42] The XPS spectra (**Figure 5.7**) also reveal the successful incorporation of $CTA^+$ chains in the CCNT/MXene composite.[45] **Figure 5.1f** shows the XRD patterns of various composites at the low two-theta range. The MAX phase has a typical peak at ~10°, corresponding to the (002) peak of $Ti_3AlC_2$. After etching treatment, the (002) peak became broader and left shifted to lower angle, which is attributed to the successful extraction of Al atoms from $Ti_3AlC_2$. The inter-lamellar spacing between the few-layered MXene nanosheets is about 0.975 nm based on the Scherrer formula, corresponding to the previous report.[42] The broadest (002) peak was observed in CCNT/MXene composite at the lowest two-theta degree of 4.8°, demonstrating

an dramatically expanded inter-lamellar space of ~1.83 nm. The increased inter-lamellar spacing further proves the intercalation of CTAB cations into the interlayer of negatively charged MXenes by electrostatic interaction.[42] A similar approach was also reported to synthesize single-layered $MoS_2$/graphene composite with the assistance of CTAB for Li-ion batteries with fast ion transport.[46] In addition, the positively charged $CTA^+$ may promote the adoption of polyselenide anions. As a result, with the synergistic Lewis acid-base interaction induced by $CTA^+$ and 2D MXene nanosheets, the CCNT/MXene/PP composite separator can strongly adsorb the polyselenides without prohibiting the transport of ions and electrons (**Figure 5.1a**).

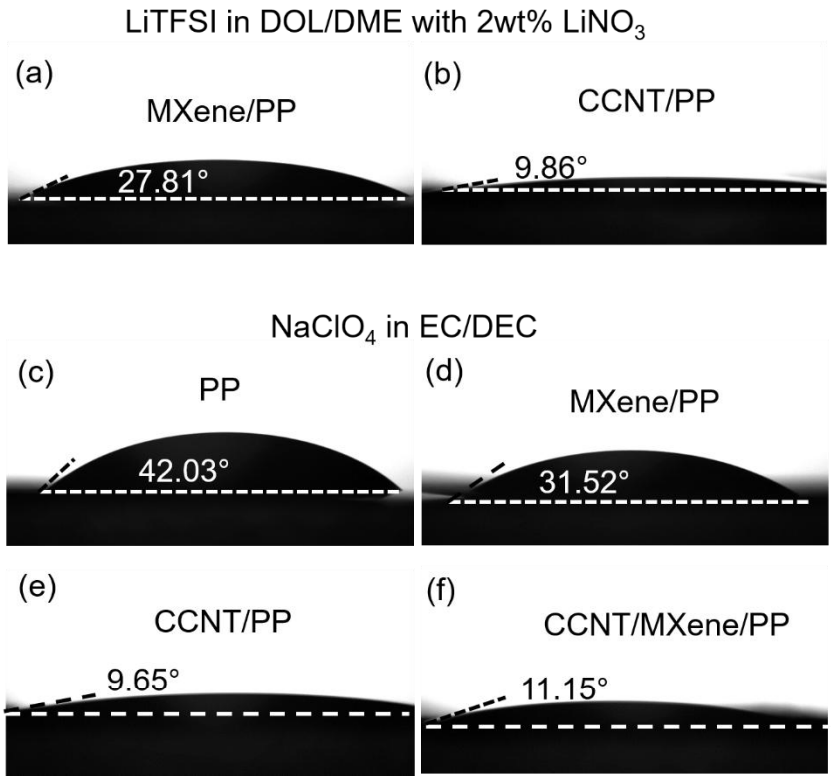


**Figure 5.8** Electrolyte wettability test of different separators with **(a, b)** LiTFSI in DOL/DME (1/1 by volume) with 2 wt% $LiNO_3$, **(c-f)** $NaClO_4$ in EC/DEC (1/1 by volume) electrolyte.

Importantly, the electrolyte wettability of CCNT/MXene/PP has been greatly improved with the assistance of interconnected CNT networks. High electrolyte permeable separator is preferred for the fast conversion-type redox reactions on the solid-electrolyte interface. Here, the hydrophilicity of various separators were evaluated by measuring the contact angles on the separator-electrolyte interfaces in **Figure 5.1g** and **Figure 5.8a-f**. Within 0.5 s, the contact angle (CA) of the electrolyte on the CCNT/MXene/PP separator was 10.12° (**Figure 5.1h**), much lower than the PP separator (38.49°, **Figure 5.1g**) and MXene/PP separator (27.81°, **Figure 5.8a**). The large CA on MXene/PP separator suggests the incompatibility of hydrophilic surface groups on MXene with the organic electrolyte. The smallest CA of 9.86° in CCNT/PP separator is due to the interconnected CNT network, showing good electrolyte compatibility. The improved wettability in CCNT/MXene/PP separator is beneficial for the fast ion/electron migration. We also examined the wettability of the as-fabricated separators with Na-ion electrolyte ($NaClO_4$ in EC/DEC). As shown in **Figure 5.8c-f**, a similar phenomenon was also observed, where the CCNT/PP and CCNT/MXene/PP separators displayed much better electrolyte wettability than the bare PP and MXene/PP separators. The small CA on CCNT/MXene/PP separator also suggests its superior compatibility with Na-ion electrolyte.

## 5.3.2 DFT calculations

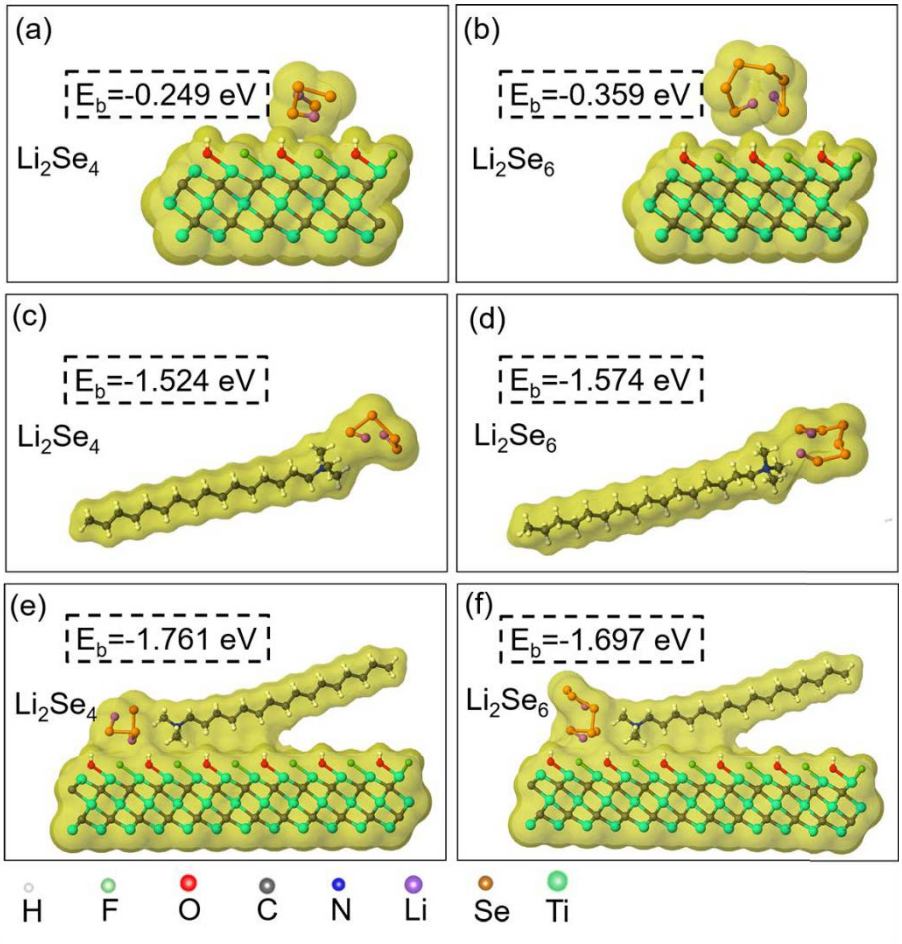


**Figure 5.9** Optimized molecular models of the interactions between $Li_2Se_4$, $Li_2Se_6$ and **(a, b)** MXene ($Ti_3C_2T_x$), **(c, d)** CTAB, **(e, f)** CTAB-MXene via the first-principle calculations along with the corresponding binding energies.

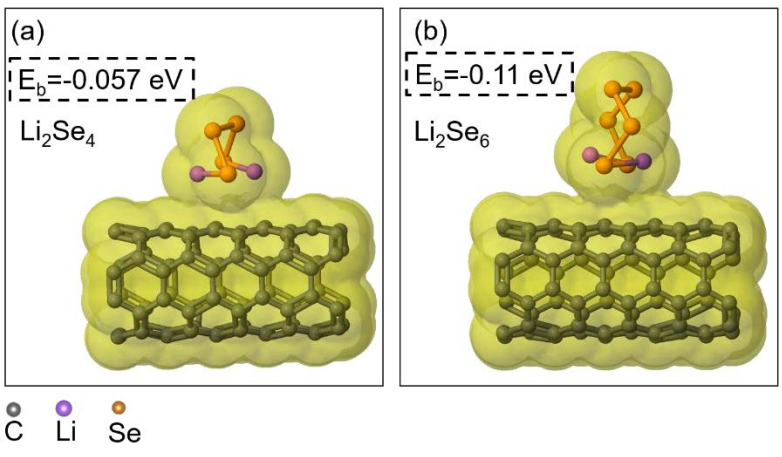

**Figure 5.10** Optimized molecular models of the interactions between **(a)** $Li_2Se_4$, **(b)** $Li_2Se_6$ and CNT via the first-principle calculations with the corresponding binding energies.

To theoretically study the interactions between CTAB, MXene and lithium polyselenide species, the first-principle calculations were conducted to investigate the binding energies ($E_b$) between representative polyselenides ($Li_2Se_4$/$Li_2Se_6$) and MXene, CTAB as well as the CTAB-MXene systems. As the CNTs were also applied in the experiment, the interactions between $Li_2Se_4$/$Li_2Se_6$ and CNT were calculated firstly. As shown in **Figure 5.10**, a negligible $E_b$ of -0.057/-0.11 eV was computed between CNTs and $Li_2Se_4$/$Li_2Se_6$, respectively. This result coincides with previous reports, revealing the weak physical interaction between carbon matrix and polyselenides.[25] Therefore, our calculations mainly focus on the CTAB, MXene and CTAB/MXene substrates (as shown in **Figure 5.9**). As demonstrated in **Figure 5.9 (a and b)**, MXene shows a mild adsorption strength to $Li_2Se_4$ ($E_b$=-0.249 eV) and $Li_2Se_6$ ($E_b$=-0.359 eV). The moderate $E_b$ between MXene and polyselenides could be ascribed to the -OH/-F surface groups that hinders direct contact between polyselenides species and Lewis acid Ti sites. In contrast, CTAB shows strong affinities to both $Li_2Se_4$ and $Li_2Se_6$ with $E_b$ of -1.524 eV and -1.574 eV, repectively (**Figure 5.9c and d**). The strong interactions originates from the intimate charge attraction between positively charged $CTA^+$ and negatively charged polyselenides anions, which was also previously verified in Li-S batteries.[44] Interestingly, after combining CTAB with MXene in **Figure 5.9 (e and f)**, the CTAB/MXene substrate demonstrates stronger affinities to $Li_2Se_4$ (-1.764 eV) and $Li_2Se_6$ (-1.697 eV) compared with the individual substrates. It is known that the anchoring of CTAB molecules on a substrate can modify the surface properties of the substrate, e.g. increasing the wettability and changing the localized charge density through electrostatic interactions.[47-49] These modifications may be responsible for the enhanced synergistic adsorption of CTAB-MXene substrate for the polyselenides. The XPS spectrum

of Ti 2p in **Figure 5.11** further suggests that the CCNT/MXene/PP separator shows stronger Ti-Se binding energy (455 eV)[50] compared to that of MXene/PP separator after the 1st cycle, which is consistent with the calculation results.

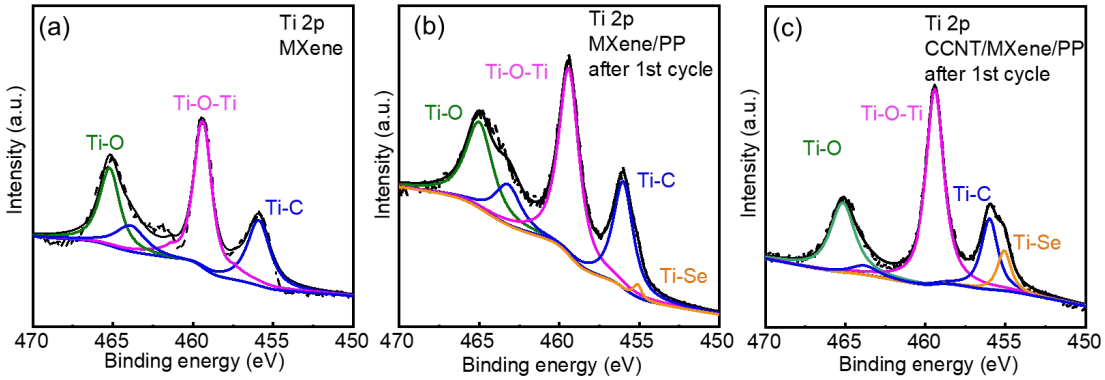


**Figure 5.11** XPS spectra of Ti 2p in **(a)** MXene, **(b)** MXene/PP separator after 1st cycle and **(c)** CCNT/MXene/PP separator after 1st cycle.

## 5.3.3 *in situ* permeation experiment and mechanism study

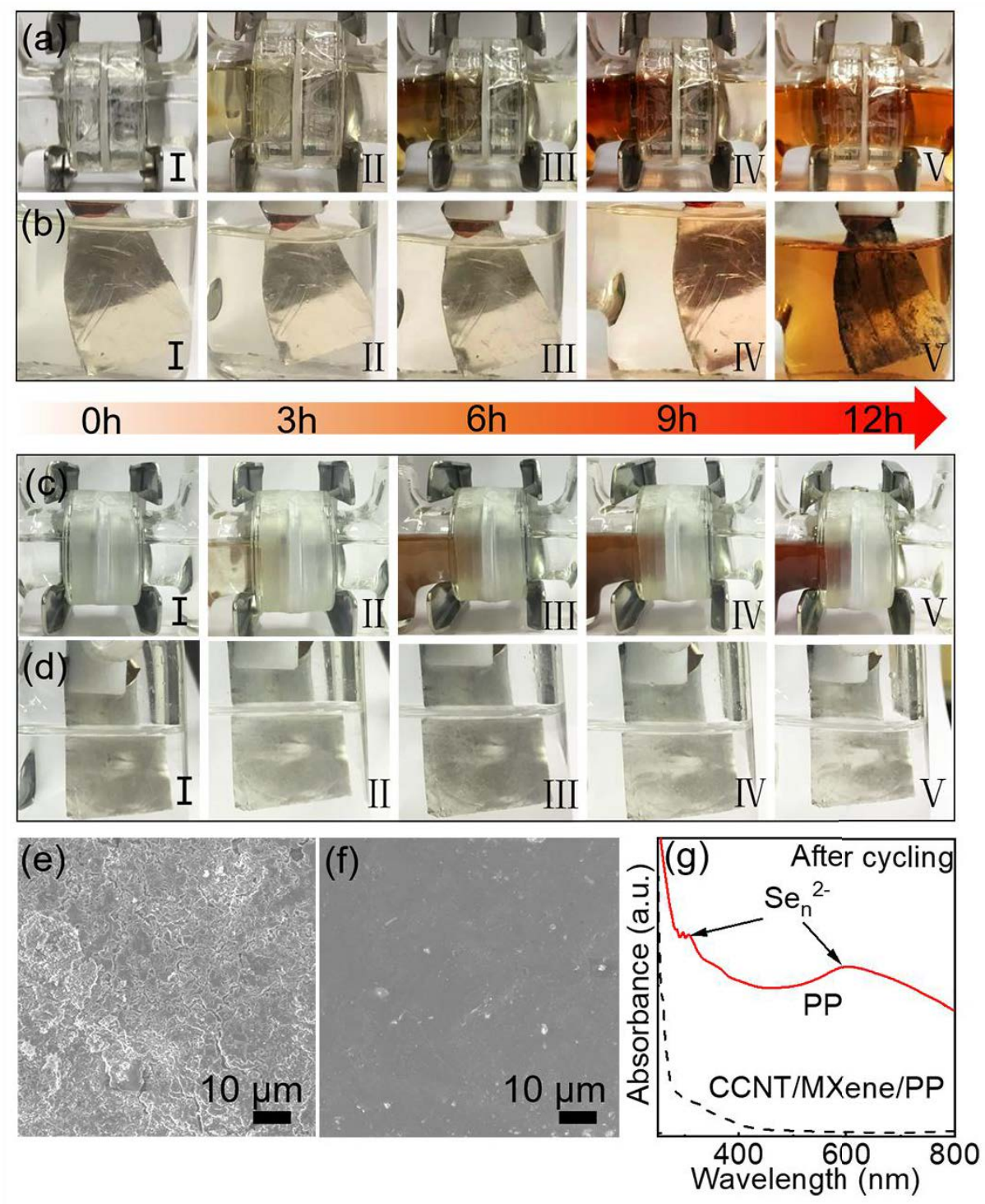


**Figure 5.12** *In situ* permeation tests during the first discharge at 0.1 C for the (a, b) PP and **(c, d)** CCNT/MXene/PP separators with an H-type cell for Li-Se batteries. SEM images of Li anode of the H-type cell after discharging with **(e)** PP separator and **(f)** CCNT/MXene/PP

separator. **(g)** UV-vis spectrum of electrolyte in the right chambers of corresponding H-type cells after discharging.

As the CCNT/MXene/PP separator shows superior separator-electrolyte interface and strong adsorption to the polyselenides, the separator was then employed in Li-Se batteries using an H-type cell (**Figure 5.12a-d**) for *in situ* permeation experiment. The behaviour of polyselenides can be systematically studied and the suppressed shuttle effect is visually observed. Here, the H-type cell was assembled with a cathode (CB/Se) and Li anode on two sides of the cell and the separators (PP or CCNT/MXene/PP) were placed in the middle. As shown in **Figure 5.12a (I)**, the electrolyte is clear on both sides in the freshly assembled cell with PP separator. Upon discharging (**Figure 5.12a (II)**), a light brown colour appears on the left (cathode) side, indicating the generation of polyselenides. As discharge proceeds (**Figure 5.12a (III)**), the dissolved polyselenides become concentrated. Upon extended discharging (**Figure 5.12a (IV)**), the electrolyte turns to red and a light red colour can be observed on the anode side , which suggests the formation of short-chain polyselenides ($Se_n^{2-}$, $n \leq 4$) and their diffusion to the anode side.[51] As the discharge goes in-depth (**Figure 5.12a (V)**), the red colour of electrolyte on both sides turns to the same level, indicating a severe shuttle effect. In particular, the depletion of polyselenides by Li anode can be clearly observed in **Figure 5.12b (I-V)**, where the polyselenides react with Li metal to form black $Li_2Se$ on the surface of Li metal. The *in situ* permeation investigation clearly demonstrated that the soluble polyselenides can severely shuttle to the anode upon the first discharge. In sharp contrast, the CCNT/MXene/PP separator has strong blocking effects on the polyselenides with no obvious polyselneids observed on the anode side (**Figure 5.12c (I-V)**). Notably, the colour of Li metal anode does not change obviously during discharge (**Figure 5.12d (I-V)**), indicating that the Li anode is protected by the CCNT/MXene/PP separator. Moreover, *ex situ* SEM, *ex situ* EDS mapping of the Li metal and *ex situ* UV-vis measurement of the electrolyte on the anode

side of the H-type cell after discharge were characterized to further confirm the suppressed shuttle effect (**Figure 5.12e-g** and **Figure 5.13**). The smooth surface of Li metal (**Figure 5.12f**) and no polyselenides in **Figure 5.12g** indicates that the polyselenides are effectively blocked by the CCNT/MXene/PP separator.[52]

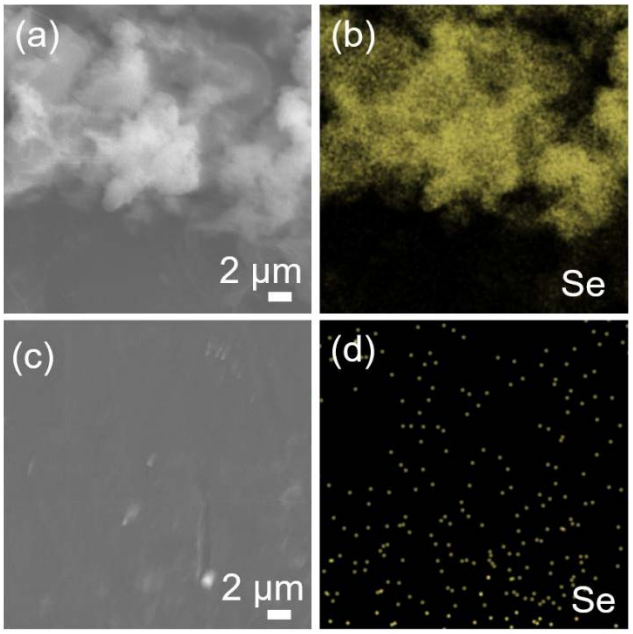


**Figure 5.13** SEM images of Li metal and corresponding EDS mapping of Se on the Li anode in the H-type cell after cycling with **(a, b)** PP separator and **(c, d)** CCNT/MXene/PP separator.

## 5.3.4 Electrochemical measurements

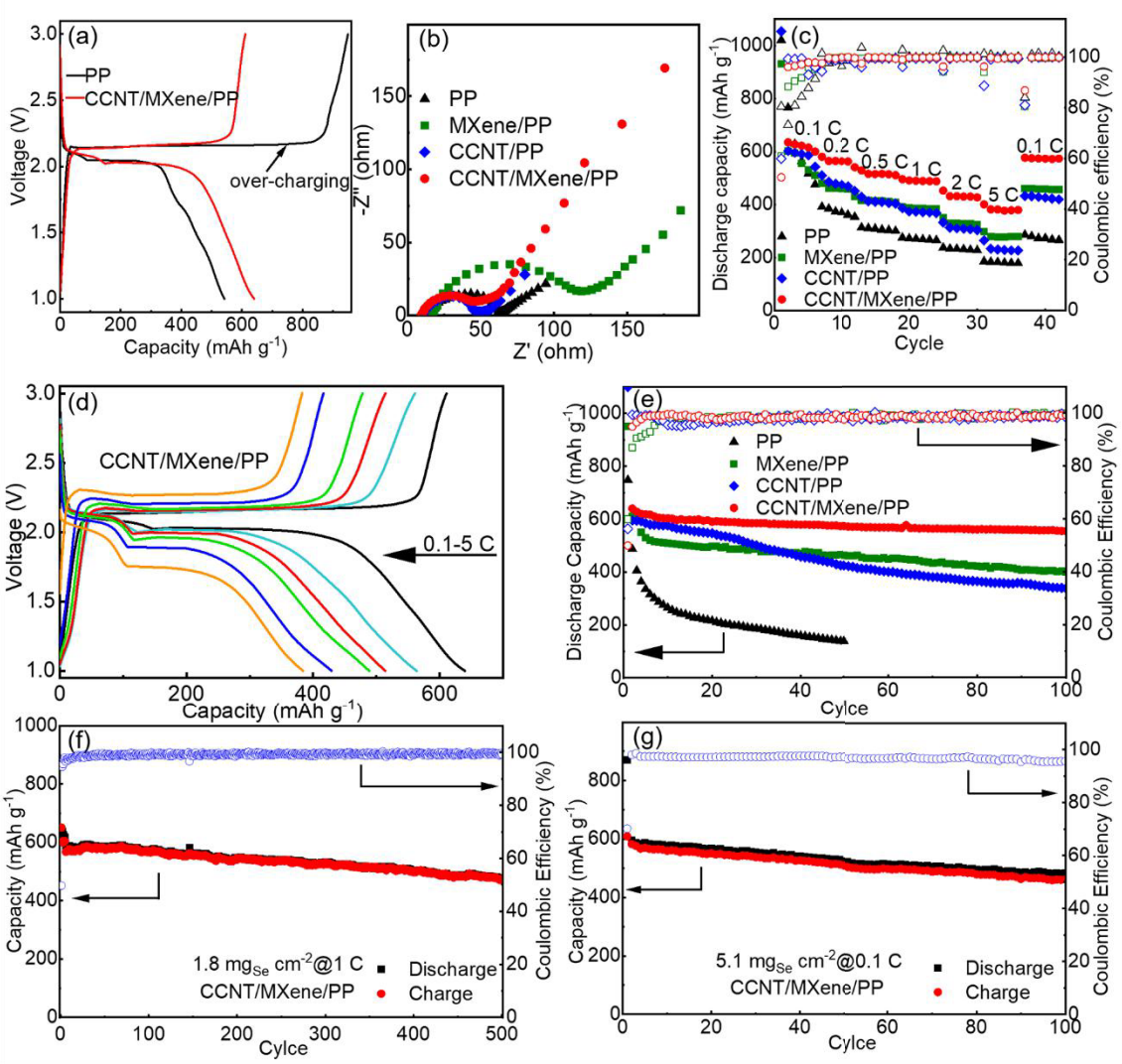


**Figure 5.14** Electrochemical performance of Li-Se batteries with different separators. **(a)** The second charge/discharge profiles of the cells with PP, MXene/PP, CCNT/PP and CCNT/MXene/PP separators at 0.1 C. **(b)** Electrochemical impedance spectra (EIS) of the cells with different separators before cycling. **(c)** Rate performance with various separators. **(d)** Corresponding charge-discharge curves of the cell with CCNT/MXene/PP separator. **(e)** Cycling performances and Columbic efficiencies at 0.1 C for the cells with various separators. **(f)** Long-term cycling stability over 500 cycles with CCNT/MXene/PP separator at 1C. **(g)**

Cycling stability of the CCNT/MXene/PP cell with a high Se area mass loading of 5.1 mg $cm^{-2}$ at 0.1 C over 100 cycles.

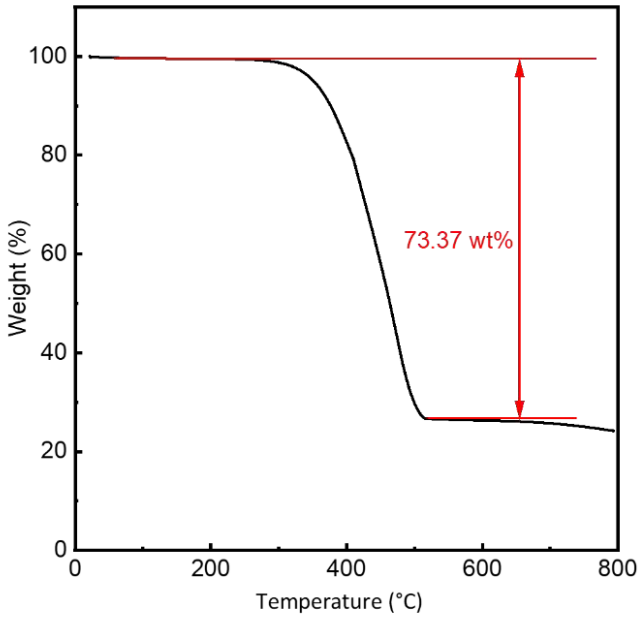


**Figure 5.15** TG profiles of CB/Se composite in $N_2$ atmosphere.

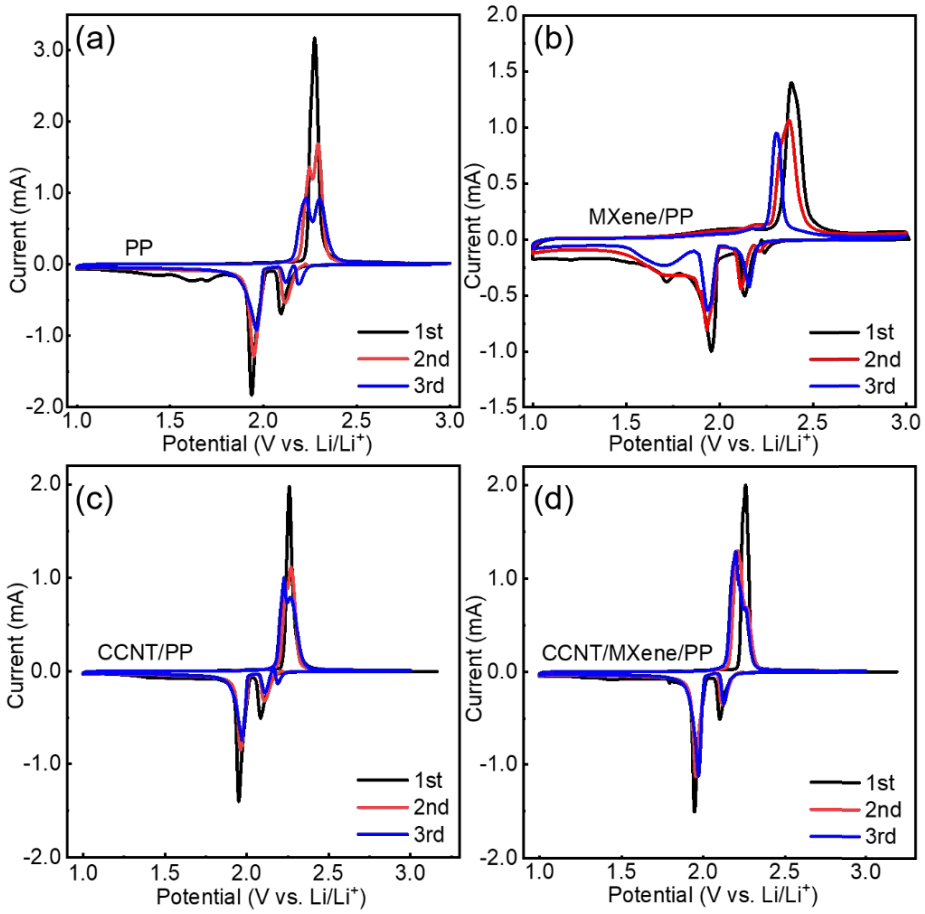


**Figure 5.16** CV curves of the batteries with **(a)** PP, **(b)** MXene/PP, **(c)** CCNT/PP and **(d)** CCNT/MXene/PP separators.

**Figure 5.14** shows the electrochemical performances of the Li-Se batteries with various separators. The battery consists carbon black/Se composite cathode (73.37 wt% by TGA measurement, **Figure 5.15**), lithium metal anode and different separators. Firstly, we measured the cyclic voltammetry (CV) behaviours of the Li-Se cells with various separators at a scan rate of 0.1 mV $s^{-1}$. As indicated in **Figure 5.16**, the cell with CCNT/MXene/PP separator shows two typical cathodic peaks in the first cycle, which corresponds to the transformation from Se to high-order $Li_2Se_n$ ($n \geq 4$) at 2.10 V and then from $Li_2Se_4$ to solid $Li_2Se_2$/$Li_2Se$ at 1.95 V. The subsequent anodic peak at 2.26 V represents the conversion of polyselenides to $Se_8$.[51] The cells with the other three separators also show similar CV behaviours to that of CCNT/MXene/PP based cell. However, differing from the cells with PP,

MXene/PP and CCNT/PP separators, the CV curves of the cell with CCNT/MXene/PP separator after first cycle are almost unchanged, suggesting the highly reversible redox reactions. Furthermore, **Figure 5.14a** presents the 2nd cycle galvanostatic discharge/charge profiles at 0.1 C with different separators. The battery with CCNT/MXene/PP separator delivers a high discharge capacity of 639.7 mAh $g^{-1}$ with a high Coulombic efficiency (CE) of 95.4% in the second cycle. However, for the PP separator, it only presents a capacity of 540 mAh $g^{-1}$ in the second cycle. Interestingly, during the delithiation process, the long charging plateaus leads to an over-charging capacity of 950 mAh $g^{-1}$, which is due to the severe shuttle effect.[7] The other batteries with MXene/PP, CCNT/PP and CCNT/MXene/PP do not show obvious over-charging plateaus, indicating that the shuttle reaction is inhibited by the modified separators. Specifically, the battery with MXene/PP separator delivers discharge/charge capacity of 608.7/531.8 mAh $g^{-1}$ with a low CE of 87% in the second cycle. The low CE could be due to the restack of MXene nanosheets.[53] For the CCNT/PP separator, the discharge and charge capacities in the second cycle are ~590.3 and 588.4 mAh $g^{-1}$, respectively. The high discharge/charge capacities with CCNT/PP separator indicate that the CTAB modified cross-linked CCNT not only prohibits shuttling of polyseleniedes but also provides a high CE of 99.68% in the 2nd cycle.

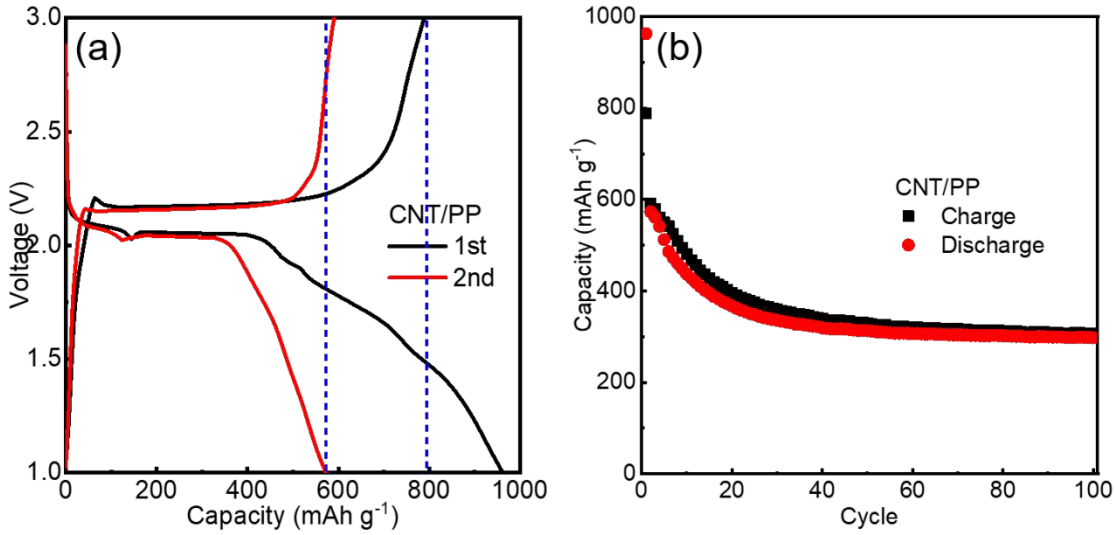

**Figure 5.17** Electrochemical performance of the battery with CNT/PP separator.

For comparison, the cell with CNT/PP separator (without CTAB modification) shows an over-charging behaviour and undergoes fast capacity decay (**Figure 5.17**) due to the weak physical interaction between CNT and polyselenides. This suggests that CTAB can provide strong interactions to polyselenides.

In addition, the superior electrolyte-separator interface in CCNT/MXene/PP separator also benefits the ion/electron conductivity. The electronic and ionic conductivities were firstly investigated by the EIS measurement (**Figure 5.14b**). All the four separators exhibit single semicircles in high frequency region, where the CCNT/MXene/PP separator shows the smallest resistance. The small resistance in CCNT/MXene/PP battery may be attributed to the interconnected CNT networks and the enlarged interlayer spacing in MXene layers as compared to the MXene/PP battery.[28]

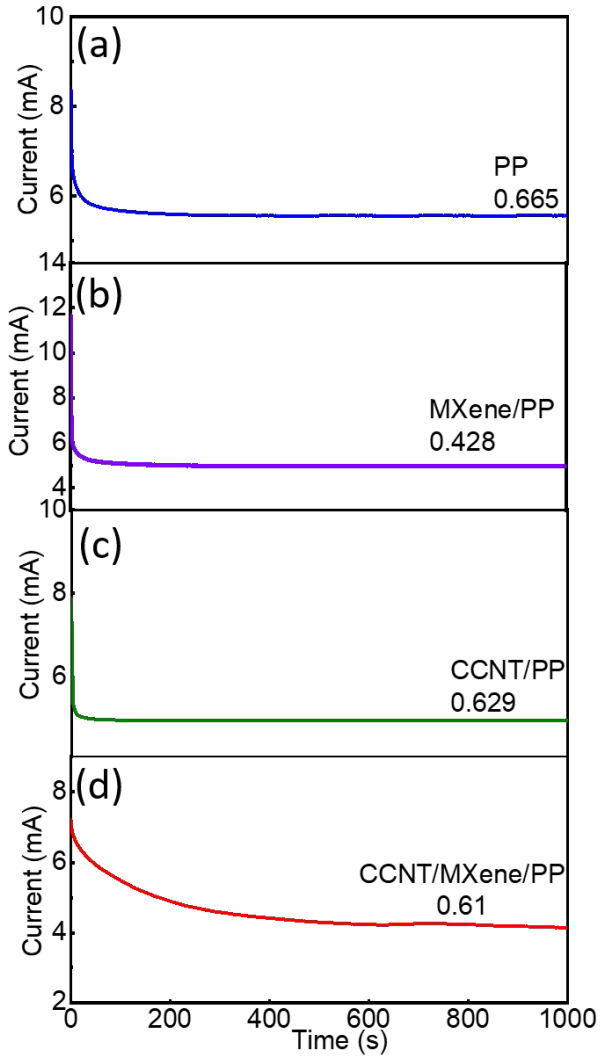


**Figure 5.18** Lithium ions transference number for **(a)** PP, **(b)** Mxene/PP, **(c)** CCNT/PP and **(d)** CCNT/MXene/PP separators.

Besides, the lithium transference number (LTN) is another key factor that influence the utilization of the active materials, power density and high current performance.[29] The LTN was obtained by applying a 10 mV potential on the batteries with different separators sandwiched between two Li electrodes. As a result, the current-time (*i*-*t*) curves are obtained (**Figure 5.18**) and the LTN is evaluated based on the ratio of steady state current to the initial current. It shows that the LTN of CCNT/MXene/PP separator (0.61) is much higher than that of MXene/PP separator (0.428), which is comparable to that of PP (0.665) and CCNT/PP (0.629) separators, demonstrating a superior Li ion transport efficiency.

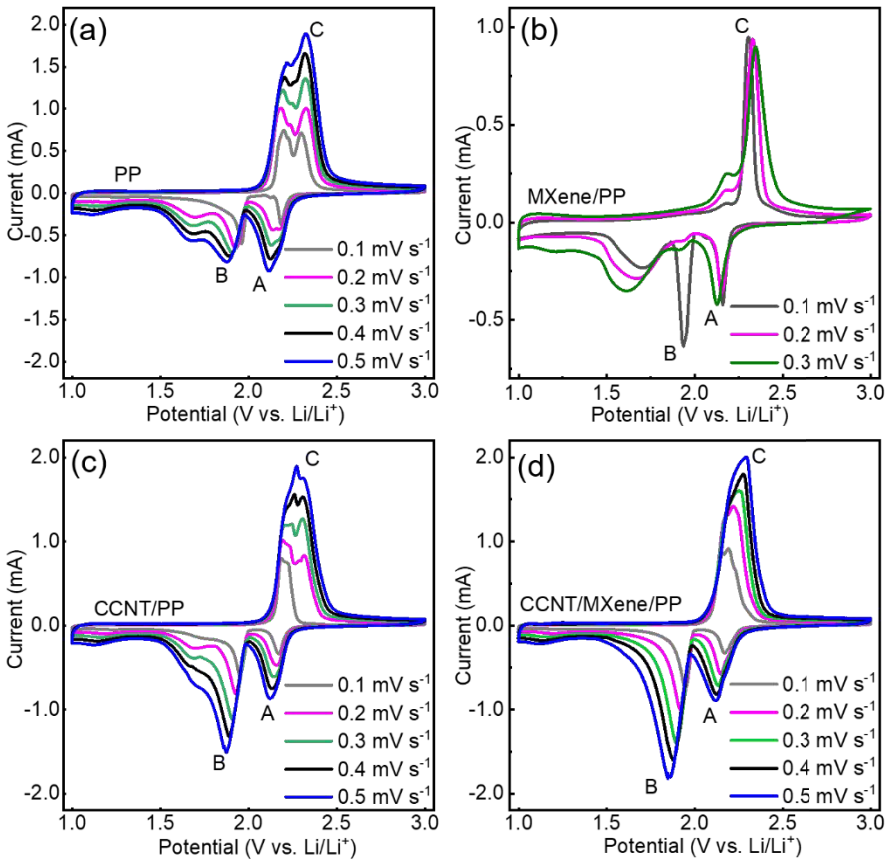


**Figure 5.19** Cyclic voltammograms at various voltage scan rates of Li-Se batteries with different separators.

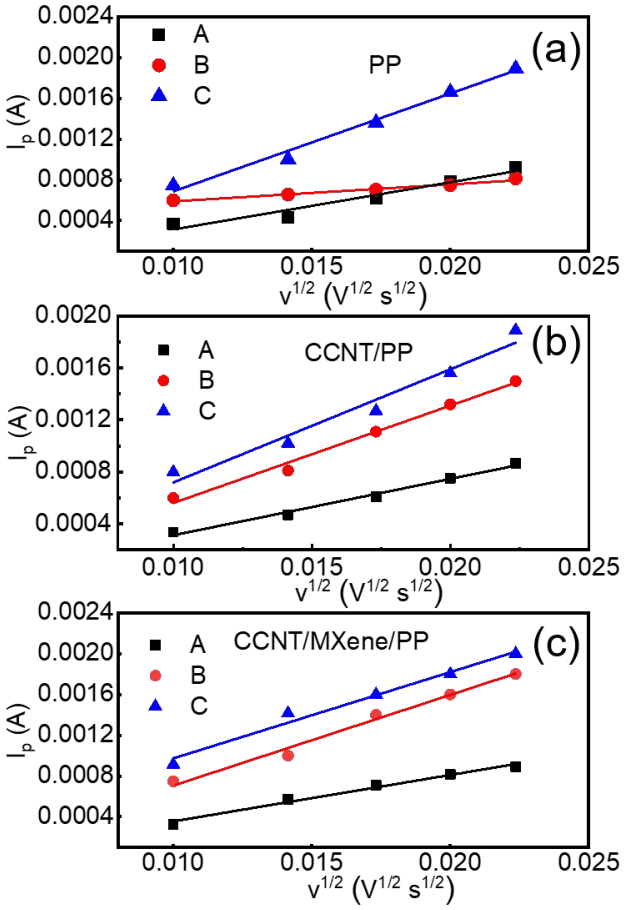


**Figure 5.20** Corresponding linear fits of the peak currents of Li-Se batteries with **(a)** PP separator, **(b)** CCNT/PP separator and **(c)** CCNT/MXene/PP separator.

The Li ion diffusion coefficients ($D_{Li^+}$) are quantitatively calculated based on a series of cyclic voltammograms (CV) under various scan rates (**Figure 5.19 and 5.20**). The Li ion diffusion coefficient is calculated based on the Randles-Sevick equation. The value of Li ion diffusion coefficients for the batteries with different separators are summarized in **Table 5.2**. It is noted that the diffusion coefficients at peak A are almost the same magnitude for CCNT/PP ($3.25\times10^{-9}$ $cm^2$ $s^{-1}$) and CCNT/MXene/PP ($3.18\times10^{-9}$ $cm^2$ $s^{-1}$) separators, lower than that of PP separator ($1.56\times10^{-8}$ $cm^2$ $s^{-1}$). The peak A involves the formation high-order polyselenides. Although the shuttle effect is inhibited by the modified separators, the open

pores on PP separator are also blocked, leading to slow Li ion diffusion.[29] At the peak B, the high-order polyselenides gradually convert to solid $Li_2Se_2$/$Li_2Se$. These solid lithium selenides can easily precipitate on the PP separator, forming an inactive layer that hinders the Li ion diffusion across PP separator with a small $D_{Li^+}$ of $4\times10^{-10}$ $cm^2$ $s^{-1}$. In contrast, the CCNT/MXene/PP separator can provide extra precipitation sites for the solid lithium selenides and protect the PP separator from blocking, therefore facilitating a fast Li-ion transport ($1.34\times10^{-8}$ $cm^2$ $s^{-1}$). This further coincides with **Figure 5.14a**, in which the large capacity at the low plateau indicates the recovered activities and efficient utilization of the $Li_2Se_n$ species. However, the MXene/PP separator delivers a poor Li ion diffusion, which is consistent with the EIS and LTN results.

**Table 5.2** The Li-ion diffusion coefficient with different separators

| Peak ($cm^2$ $s^{-1}$) | PP | MXene/PP | CCNT/PP | CCNT/MXene/PP |
|---|---|---|---|---|
| A | $1.56\times10^{-8}$ | -- | $3.25\times10^{-9}$ | $3.18\times10^{-9}$ |
| B | $4.00\times10^{-10}$ | -- | $9.80\times10^{-9}$ | $1.34\times10^{-8}$ |
| C | $3.60\times10^{-9}$ | -- | $1.30\times10^{-8}$ | $1.25\times10^{-8}$ |

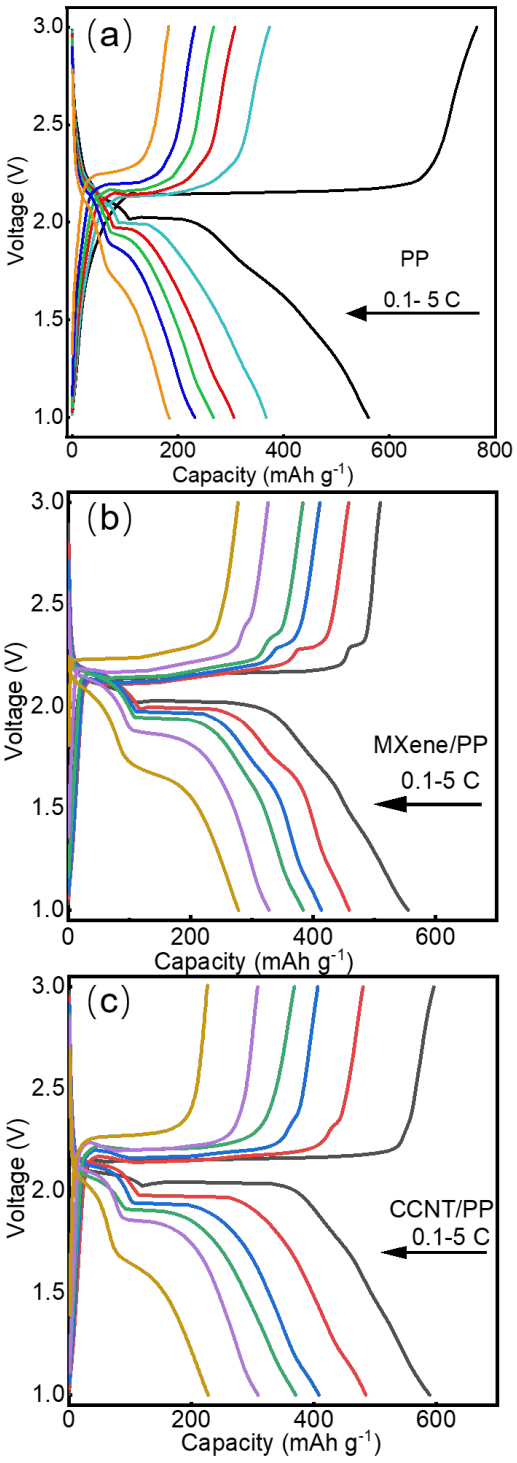


**Figure 5.21** Corresponding discharge/charge profiles of the cells with **(a)** PP separator, **(b)** MXene/PP separator and **(c)** CCNT/PP separator.

Based on the EIS, LTN and $D_{Li^+}$ results, a superior rate capability of the battery with CCNT/MXene/PP separator is demonstrated in **Figure 5.14c** from 0.1 to 5 C. As expected, the battery with CCNT/MXene/PP separator achieves an excellent rate performance with a high discharge capacity above 600 mAh $g^{-1}$ at 0.1 C and 380 mAh $g^{-1}$ at a high current of 5 C, which are much higher than that of PP (~180 mAh $g^{-1}$), MXene/PP (~277 mAh $g^{-1}$) and CCNT/PP (~230 mAh $g^{-1}$) separators at 5C. In addition, the CCNT/MXene/PP based battery also shows a good capacity recovery of 575 mAh $g^{-1}$ when the current returns back to 0.1 C from 5 C. The corresponding discharge/charge curves of CCNT/MXene/PP battery in **Figure 5.14d** also reveals its good rate performance, where the battery can maintain a flat plateau at high currents up to 5 C. However, the other three batteries (**Figure 5.21**) did not deliver flat plateaus at 5C. The superior rate capability suggests the fast reaction kinetics and effectively suppressed shuttle reaction in the battery with CCNT/MXene/PP separator. Furthermore, the cycling performances of the batteries with different separators at 0.1 C were shown in **Figure 5.14e**. The CCNT/MXene/PP battery delivered the highest discharge capacity of ~640 mAh $g^{-1}$ in the second cycle and maintained a reversible capacity of 554 mAh $g^{-1}$ at 0.1 C after 100 cycles with a small capacity fading of 0.13% per cycle. However, the batteries with PP, MXene/PP, CCNT/PP separators can only deliver 137, 398 and 337 mAh $g^{-1}$, respectively. In particular, the battery with MXene/PP separator delivers more stable cycling performance than CCNT/PP separator, suggesting MXene is beneficial for long cycling performance at low C rate.

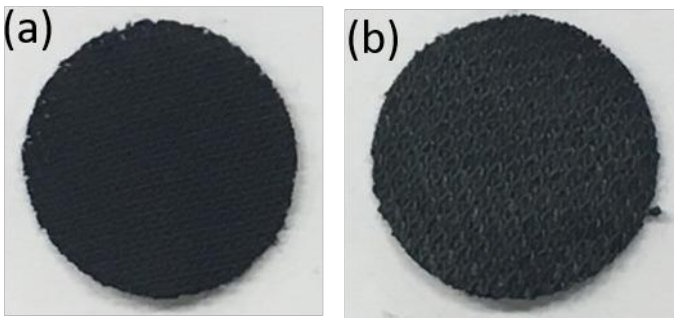

**Figure 5.22** Digital images of **(a)** carbon cloth and **(b)** carbon cloth loaded with 50 wt% Se.

To investigate the long cycling stability of the battery with CCNT/MXene/PP separator, the battery was first tested at a current of 0.1 C for 5 cycles and then cycled at a high current of 1C for 500 cycles (**Figure 5.14f**). The battery showed a high stability with only a capacity decay of 0.05% per cycle, maintaining a high reversible capacity of 478 mAh $g^{-1}$ after 500 cycles. Moreover, we evaluated the high Se areal mass loading performance (5.1 mg $cm^{-2}$, **Figure 5.22**). As a result, the cell with CCNT/MXene/PP separator presented a stable cycling stability with a high capacity of 485 mAh $g^{-1}$ after 100 cycles (**Figure 5.14g**). This result is one of the best performances among the previous works in Li-Se batteries.

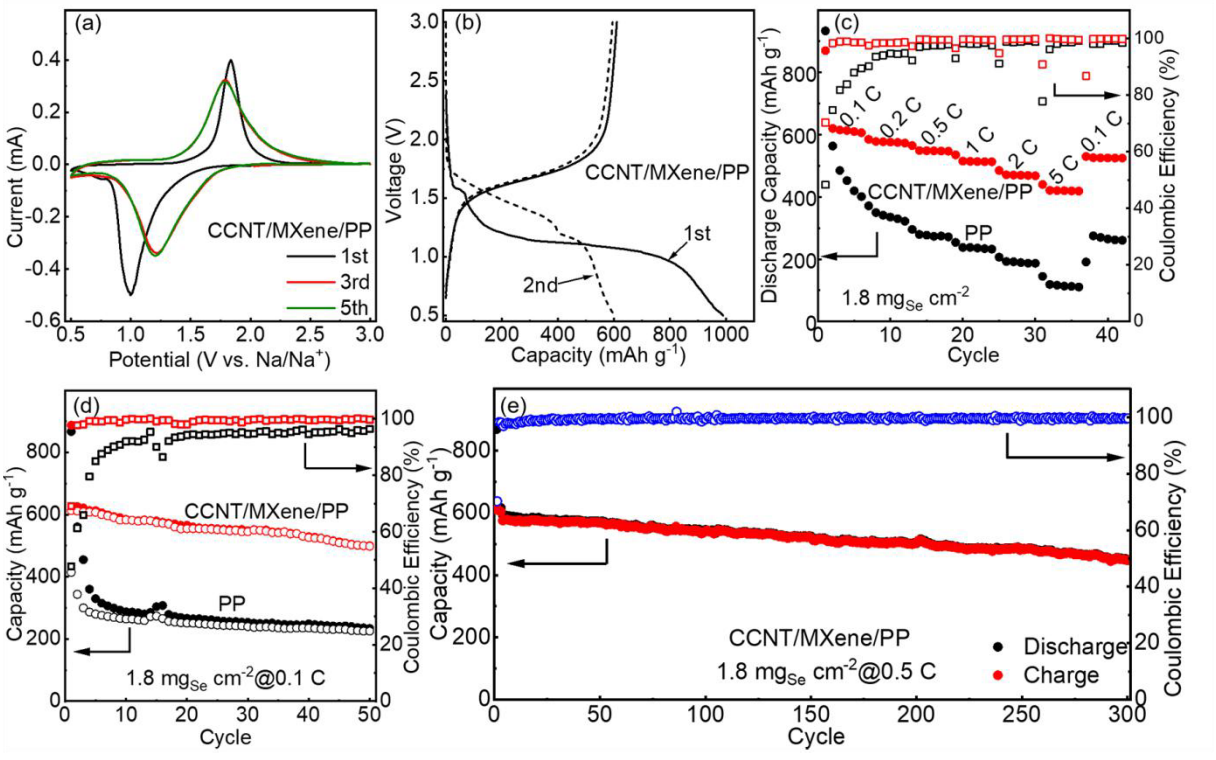


**Figure 5.23** Electrochemical performance of Na-Se batteries **(a)** CV curves of the cell with CCNT/MXene/PP separator in the cut off voltage range of 0.5-3 V. **(b)** The 1st and 2nd discharge-charge curves of the battery with CCNT/MXene/PP separator. **(c)** Rate

performance of the cells with PP and CCNT/MXene/PP separators. **(d)** Cycling performance of the cells with PP and CCNT/MXene /PP separators at 0.1 C. **(e)** Long cycling performance of the cell with CCNT/MXene/PP separators at 0.5C.

To demonstrate the universal application of the as-prepared CCNT/MXene/PP separator, we further evaluated its electrochemical performance in Na-Se batteries. **Figure 5.23a** shows the selected CV curves of Na-Se battery with CCNT/MXene/PP separator. In the first cycle, it shows one pair of cathodic and anodic peaks at 1.0 V and 1.84 V, respectively, which reveals the one phase transformation between Se and $Na_2Se$ in the carbonate-based electrolyte. After the first cycle, the two peaks shift closer and remain highly overlapped in the following cycles, demonstrating the highly reversible conversion chemistry with CCCNT/MXene/PP separator. **Figure 5.23b** shows the 1st and 2nd galvanostatic discharge-charge profiles of the cells CCNT/MXene/PP separators. For the CCNT/MXene/PP battery, it delivers initial discharge and charge capacities of 989.5 and 610 mAh $g^{-1}$, respectively. The irreversible capacity can be attributed to the side reactions and the formation of SEI layer.

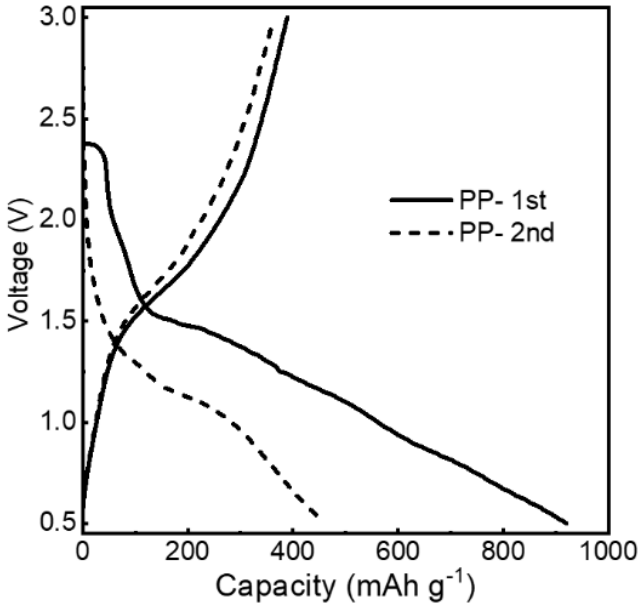


**Figure 5.24** Discharge and charge profile of the battery with PP separator in Na-Se battery.

The battery using PP separator also shows similar charge/discharge profiles to that of CCNT/MXene/PP battery (**Figure 5.24**). However, the battery with PP separator has an extremely low ICE of 47.8% and can only deliver a low discharge capacity of 455.5 mAh $g^{-1}$ in the second cycle. **Figure 5.23c** shows the rate capabilities of the batteries. It shows that the PP battery delivers fast capacity decay at 0.1 C and can only present an extremely low capacity of 110.6 mAh $g^{-1}$ at 5 C. In contrast, the battery with CCNT/MXene/PP exhibits a high discharge capacity of 419 mAh $g^{-1}$ at 5 C and recovers back to 525 mAh $g^{-1}$ when the current is reversed back to 0.1 C. The improved rate capability of the CCNT/MXene/PP battery indicates a preferable Na ion transport kinetics. In addition, the good wettability of the carbonate-based electrolyte on the CCNT/MXene/PP also provides superior solid-electrolyte interfacial compatibility. As a result, the CCNT/MXene/PP shows a stable cycling performance at 0.1 C and maintains a high reversible capacity of 498 mAh $g^{-1}$ after 50 cycles (**Figure 5.23d**). By contrast, the capacity of PP battery decreases rapidly from 867 to 330 mAh $g^{-1}$ during the first 5 cycles and only delivers a low capacity of 225.6 mAh $g^{-1}$ after 50 cycles at 0.1 C. The poor cycling performance of PP battery may be attributed to the severe polyselenide shuttling and low utilization of the active material (Se).[26, 54-55] Furthermore, the long cycling performance of the CCNT/MXene/PP battery was examined at 0.5 C in **Figure 5.23e**. Owing to the fast transfer of Na ions and suppressed shuttle effect, the battery delivered a high reversible capacity of 450 mAh $g^{-1}$ after 300 cycles with a high capacity retention of 72.6 % for Na-Se batteries.

## 5.4 Summary

In summary, we have designed an ultra-thin CCNT/MXene/PP composite separator via self-assembly and filtration process. When applied in Li-Se and Na-Se batteries, the as-prepared CCNT/MXene/PP separators possess an enhanced Lewis acid-base effect for

prohibiting the shuttle effect. Meanwhile, the interconnected CNT networks and enlarged interlayer spacing of MXene can improve the electrolyte wettability and facilitate the ionic transport. *In situ* permeation test was performed to investigate the electrochemical behavior of Se during cycling, suggesting a suppressed shuttle effect and protected Li anode by CCNT/MXene/PP separator. As a result, the cells with CCNT/MXene/PP separator deliver a significantly enhanced performance in both Li-Se and Na-Se batteries. This work provides a novel strategy for building a preferable solid-electrolyte interface to suppress the shuttle effect while maintaining the fast ionic transport.

## 5.5 References


1. Li, X.; Liang, J.; Luo, J.; Wang, C.; Li, X.; Sun, Q.; Li, R.; Zhang, L.; Yang, R.; Lu, S.; Huang, H.; Sun, X., High-Performance Li-SeSx All-Solid-State Lithium Batteries. *Adv. Mater.* **2019,** *31* (17), 1808100.

2. Xu, X.; Xiong, F.; Meng, J.; An, Q.; Mai, L., Multi-electron reactions of vanadium-based nanomaterials for high-capacity lithium batteries: challenges and opportunities. *Mater. Today Nano* **2020**.

3. Wang, Y.; Wang, Y.; Kang, W.; Cao, D.; Li, C.; Cao, D.; Kang, Z.; Sun, D.; Wang, R.; Cao, Y., TiO2-Coated Interlayer-Expanded MoSe2/Phosphorus-Doped Carbon Nanospheres for Ultrafast and Ultralong Cycling Sodium Storage. *Adv. Sci.* **2019,** *6* (1), 1801222.

4. Wang, Y.; Wang, Y.; Wang, Y.-X.; Feng, X.; Chen, W.; Ai, X.; Yang, H.; Cao, Y., Developments and Perspectives on Emerging High-Energy-Density Sodium-Metal

Batteries. *Chem* **2019,** *5* (10), 2547-2570.

5. Yan, Z.; Yang, Q.-W.; Wang, Q.; Ma, J., Nitrogen doped porous carbon as excellent dual anodes for Li- and Na-ion batteries. *Chinese Chemical Letters* **2020,** *31* (2), 583-588.

6. Liao, J.; Ni, W.; Wang, C.; Ma, J., Layer-structured niobium oxides and their analogues for advanced hybrid capacitors. *Chem. Eng. J.* **2019**.

7. Luo, C.; Xu, Y. H.; Zhu, Y. J.; Liu, Y. H.; Zheng, S. Y.; Liu, Y.; Langrock, A.; Wang, C. S., Selenium@Mesoporous Carbon Composite with Superior Lithium and Sodium Storage Capacity. *ACS Nano* **2013,** *7* (9), 8003-8010.

8. Li, X. N.; Liang, J. W.; Li, X.; Wang, C. H.; Luo, J.; Li, R. Y.; Sun, X. L., High-performance all-solid-state Li–Se batteries induced by sulfide electrolytes. *Energy Environ. Sci* **2018,** *11*, 2828-2832.

9. Du, H.; Feng, S.; Luo, W.; Zhou, L.; Mai, L., Advanced Li-Se S battery system: electrodes and electrolytes. *J. Mater. Sci.Technol.* **2020**.

10. Li, Q.; Liu, H.; Yao, Z.; Cheng, J.; Li, T.; Li, Y.; Wolverton, C.; Wu, J.; Dravid, V. P., Electrochemistry of Selenium with Sodium and Lithium: Kinetics and Reaction Mechanism. *ACS Nano* **2016,** *10* (9), 8788-95.

11. Aboonasr Shiraz, M. H.; Zhu, H.; Liu, Y.; Sun, X.; Liu, J., Activation-free synthesis of microporous carbon from polyvinylidene fluoride as host materials for lithium-selenium batteries. *Journal of Power Sources* **2019,** *438*.

12. Kim, S.; Cho, M.; Lee, Y., High-Performance Li–Se Battery Enabled via a One-Piece Cathode Design. *Adv. Energy Mater.* **2019**, 1903477.

13. Jin, W.-w.; Li, H.-J.; Zou, J.-z.; Inguva, S.; Zhang, Q.; Zeng, S.-z.; Xu, G.-z.; Zeng, X.-r., 2D ultrathin carbon nanosheets derived from interconnected Al-MOF as excellent hosts to anchor selenium for Li-Se battery. *Mater. Lett.* **2019,** *252*, 211-214.

14. Jin, Y.; Liu, K.; Lang, J.; Jiang, X.; Zheng, Z.; Su, Q.; Huang, Z.; Long, Y.; Wang, C.-a.; Wu, H.; Cui, Y., High-Energy-Density Solid-Electrolyte-Based Liquid Li-S and Li-Se Batteries. *Joule* **2020,** *4* (1), 262-274.

15. Zheng, Z.; Su, Q.; Xu, H.; Zhang, Q.; Ye, H.; Wang, Z., A pomegranate-like porous carbon nanomaterial as selenium host for stable lithium-selenium batteries. *Materials Letters* **2019,** *244*, 134-137.

16. Yang, C. P.; Xin, S.; Yin, Y. X.; Ye, H.; Zhang, J.; Guo, Y. G., An advanced selenium-carbon cathode for rechargeable lithium-selenium batteries. *Angew. Chem., Int. Ed.* **2013,** *52* (32), 8363-8367.

17. Wang, H.; Jiang, Y.; Manthiram, A., Long Cycle Life, Low Self-Discharge Sodium-Selenium Batteries with High Selenium Loading and Suppressed Polyselenide Shuttling. *Adv. Energy Mater.* **2018,** *8* (7), 1701953.

18. Zeng, L.; Zeng, W.; Jiang, Y.; Wei, X.; Li, W.; Yang, C.; Zhu, Y.; Yu, Y., A Flexible Porous Carbon Nanofibers-Selenium Cathode with Superior Electrochemical Performance for Both Li-Se and Na-Se Batteries. *Adv. Energy Mater.* **2015,** *5* (4), 1401377.

19. Gao, X.; Yang, X.; Wang, S.; Sun, Q.; Zhao, C.; Li, X.; Liang, J.; Zheng, M.; Zhao, Y.; Wang, J.; Li, M.; Li, R.; Sham, T.-K.; Sun, X., A 3D-printed ultra-high Se loading cathode for high energy density quasi-solid-state Li–Se batteries. *J. Mater. Chem. A* **2020,** *8* (1), 278-286.

20. Ma, D.; Li, Y.; Yang, J.; Mi, H.; Luo, S.; Deng, L.; Yan, C.; Zhang, P.; Lin, Z.; Ren, X.; Li, J.; Zhang, H., Atomic layer deposition-enabled ultrastable freestanding carbon-selenium cathodes with high mass loading for sodium-selenium battery. *Nano Energy* **2018,** *43*, 317-325.

21. Zhang, J.; Xu, Y.; Fan, L.; Zhu, Y.; Liang, J.; Qian, Y., Graphene–encapsulated selenium/polyaniline core–shell nanowires with enhanced electrochemical performance for Li–Se batteries. *Nano Energy* **2015,** *13*, 592-600.

22. Zhang, F.; Xiong, P.; Guo, X.; Zhang, J.; Yang, W.; Wu, W.; Liu, H.; Wang, G., A nitrogen, sulphur dual-doped hierarchical porous carbon with interconnected conductive polyaniline coating for high-performance sodium-selenium batteries. *Energy Storage Materials* **2019,** *19*, 251-260.

23. Li, Z.; Zhou, C.; Hua, J.; Hong, X.; Sun, C.; Li, H. W.; Xu, X.; Mai, L., Engineering Oxygen Vacancies in a Polysulfide-Blocking Layer with Enhanced Catalytic Ability. *Adv. Mater.* **2020**, e1907444.

24. Zhang, Y.; Guo, Y.; Wang, B.; Wei, Y.; Jing, P.; Wu, H.; Dai, Z.; Wang, M.; Zhang, Y., An integrated hybrid interlayer for polysulfides/selenides regulation toward advanced Li–SeS2 batteries. *Carbon* **2020,** *161*, 413-422.

25. Zhao, X.; Yin, L.; Zhang, T.; Zhang, M.; Fang, Z.; Wang, C.; Wei, Y.; Chen, G.; Zhang, D.; Sun, Z.; Li, F., Heteroatoms dual-doped hierarchical porous carbon-selenium composite for durable Li–Se and Na–Se batteries. *Nano Energy* **2018,** *49*, 137-146.

26. Yao, Y.; Chen, M.; Xu, R.; Zeng, S.; Yang, H.; Ye, S.; Liu, F.; Wu, X.; Yu, Y., CNT Interwoven Nitrogen and Oxygen Dual-Doped Porous Carbon Nanosheets as Free-Standing Electrodes for High-Performance Na-Se and K-Se Flexible Batteries. *Adv.*

*Mater.* **2018,** *30* (49), 1805234.

27. Wu, T.; Ding, Z.; Jing, M.; Zou, G.; Hou, H.; Tian, Y.; Jiang, Y.; Hong, W.; Ji, X., Chem-Bonding and Phys-Trapping Se Electrode for Long-Life Rechargeable Batteries. *Adv. Funct. Mater.* **2019,** *29* (9), 1809014.

28. Lei, T.; Chen, W.; Lv, W.; Huang, J.; Zhu, J.; Chu, J.; Yan, C.; Wu, C.; Yan, Y.; He, W.; Xiong, J.; Li, Y.; Yan, C.; Goodenough, J. B.; Duan, X., Inhibiting Polysulfide Shuttling with a Graphene Composite Separator for Highly Robust Lithium-Sulfur Batteries. *Joule* **2018,** *2* (10), 2091-2104.

29. Ghazi, Z. A.; He, X.; Khattak, A. M.; Khan, N. A.; Liang, B.; Iqbal, A.; Wang, J.; Sin, H.; Li, L.; Tang, Z., $MoS_2$ /Celgard Separator as Efficient Polysulfide Barrier for Long-Life Lithium-Sulfur Batteries. *Adv. Mater.* **2017,** *29* (21), 1606817.

30. Wu, J.; Zeng, H.; Li, X.; Xiang, X.; Liao, Y.; Xue, Z.; Ye, Y.; Xie, X., Ultralight Layer-by-Layer Self-Assembled $MoS_2$-Polymer Modified Separator for Simultaneously Trapping Polysulfides and Suppressing Lithium Dendrites. *Adv. Energy Mater.* **2018,** *8* (35), 1802430.

31. Chung, S.-H.; Manthiram, A., Bifunctional Separator with a Light-Weight Carbon-Coating for Dynamically and Statically Stable Lithium-Sulfur Batteries. *Adv. Funct. Mater.* **2014,** *24* (33), 5299-5306.

32. Yao, S.; Cui, J.; Huang, J.-Q.; Lu, Z.; Deng, Y.; Chong, W. G.; Wu, J.; Ihsan Ul Haq, M.; Ciucci, F.; Kim, J.-K., Novel 2D Sb2S3 Nanosheet/CNT Coupling Layer for Exceptional Polysulfide Recycling Performance. *Adv. Energy Mater.* **2018,** *8* (24), 1800710.

33. Lin, C.; Zhang, W.; Wang, L.; Wang, Z.; Zhao, W.; Duan, W.; Zhao, Z.; Liu, B.; Jin, J., A

few-layered Ti3C2 nanosheet/glass fiber composite separator as a lithium polysulphide reservoir for high-performance lithium–sulfur batteries. *J. Mater. Chem. A* **2016,** *4* (16), 5993-5998.

34. Song, J.; Su, D.; Xie, X.; Guo, X.; Bao, W.; Shao, G.; Wang, G., Immobilizing Polysulfides with MXene-Functionalized Separators for Stable Lithium-Sulfur Batteries. *ACS Appl. Mater. Interfaces* **2016,** *8* (43), 29427-29433.

35. Jeong, Y. C.; Kim, J. H.; Nam, S.; Park, C. R.; Yang, S. J., Rational Design of Nanostructured Functional Interlayer/Separator for Advanced Li-S Batteries. *Adv. Funct. Mater.* **2018,** *28* (38), 1707411.

36. Zhang, X.; Zhang, Z.; Zhou, Z., MXene-based materials for electrochemical energy storage. *Journal of Energy Chemistry* **2018,** *27* (1), 73-85.

37. Pang, J.; Mendes, R. G.; Bachmatiuk, A.; Zhao, L.; Ta, H. Q.; Gemming, T.; Liu, H.; Liu, Z.; Rummeli, M. H., Applications of 2D MXenes in energy conversion and storage systems. *Chem Soc Rev* **2019,** *48* (1), 72-133.

38. Liang, X.; Rangom, Y.; Kwok, C. Y.; Pang, Q.; Nazar, L. F., Interwoven MXene Nanosheet/Carbon-Nanotube Composites as Li-S Cathode Hosts. *Adv. Mater.* **2017,** *29* (3).

39. Song, J.; Guo, X.; Zhang, J.; Chen, Y.; Zhang, C.; Luo, L.; Wang, F.; Wang, G., Rational design of free-standing 3D porous MXene/rGO hybrid aerogels as polysulfide reservoirs for high-energy lithium–sulfur batteries. *J. Mater. Chem. A* **2019,** *7* (11), 6507-6513.

40. Bao, W.; Tang, X.; Guo, X.; Choi, S.; Wang, C.; Gogotsi, Y.; Wang, G., Porous Cryo-Dried MXene for Efficient Capacitive Deionization. *Joule* **2018,** *2* (4), 778-787.

41. Dall'Agnese, Y.; Rozier, P.; Taberna, P.-L.; Gogotsi, Y.; Simon, P., Capacitance of two-dimensional titanium carbide (MXene) and MXene/carbon nanotube composites in organic electrolytes. *J. Power Sources* **2016,** *306*, 510-515.

42. Simon, P., Two-Dimensional MXene with Controlled Interlayer Spacing for Electrochemical Energy Storage. *ACS Nano* **2017,** *11* (3), 2393-2396.

43. Guo, D.; Ming, F.; Su, H.; Wu, Y.; Wahyudi, W.; Li, M.; Hedhili, M. N.; Sheng, G.; Li, L.-J.; Alshareef, H. N.; Li, Y.; Lai, Z., MXene based self-assembled cathode and antifouling separator for high-rate and dendrite-inhibited Li–S battery. *Nano Energy* **2019,** *61*, 478-485.

44. Chen, M.; Jiang, S.; Cai, S.; Wang, X.; Xiang, K.; Ma, Z.; Song, P.; Fisher, A. C., Hierarchical porous carbon modified with ionic surfactants as efficient sulfur hosts for the high-performance lithium-sulfur batteries. *Chem. Eng. J.* **2017,** *313*, 404-414.

45. Luo, J.; Zhang, W.; Yuan, H.; Jin, C.; Zhang, L.; Huang, H.; Liang, C.; Xia, Y.; Zhang, J.; Gan, Y.; Tao, X., Pillared Structure Design of MXene with Ultralarge Interlayer Spacing for High-Performance Lithium-Ion Capacitors. *ACS Nano* **2017,** *11* (3), 2459-2469.

46. Wang, Z.; Chen, T.; Chen, W.; Chang, K.; Ma, L.; Huang, G.; Chen, D.; Lee, J. Y., CTAB-assisted synthesis of single-layer MoS2–graphene composites as anode materials of Li-ion batteries. *J. Mater. Chem. A* **2013,** *1* (6), 2202-2210.

47. Nadeem, M.; Shabbir, M.; Abdullah, M. A.; Shah, S. S.; McKay, G., Sorption of cadmium from aqueous solution by surfactant-modified carbon adsorbents. *Chem. Eng. J.* **2009,** *148* (2-3), 365-370.

48. Xin, X.; Zhang, H.; Xu, G.; Tan, Y.; Zhang, J.; Lv, X., Influence of CTAB and SDS on

the properties of oil-in-water nano-emulsion with paraffin and span 20/Tween 20. *Colloid Surface A.* **2013,** *418*, 60-67.

49. Alkan, M.; Karadas, M.; Dogan, M.; Demirbas, O., Adsorption of CTAB onto perlite samples from aqueous solutions. *J Colloid Interface Sci* **2005,** *291* (2), 309-18.

50. Yablonskikh, M. V.; Shkvarin, A. S.; Yarmoshenko, Y. M.; Skorikov, N. A.; Titov, A. N., Resonant photoemission at the L3 absorption edge of Mn and Ti and the electronic structure of 1T-Mn0.2TiSe2. *J Phys Condens Matter* **2012,** *24* (4), 045504.

51. Cui, Y.; Abouimrane, A.; Lu, J.; Bolin, T.; Ren, Y.; Weng, W.; Sun, C.; Maroni, V. A.; Heald, S. M.; Amine, K., (De)lithiation mechanism of Li/SeS(x) (x = 0-7) batteries determined by in situ synchrotron X-ray diffraction and X-ray absorption spectroscopy. *J. Am. Chem. Soc.* **2013,** *135* (21), 8047-56.

52. Xia, Y.; Lu, C.; Fang, R.; Huang, H.; Gan, Y.; Liang, C.; Zhang, J.; He, X.; Zhang, W., Freestanding layer-structure selenium cathodes with ultrahigh Se loading for high areal capacity Li-Se batteries. *Electrochem. commun.* **2019,** *99*, 16-21.

53. Ahmed, B.; Anjum, D. H.; Gogotsi, Y.; Alshareef, H. N., Atomic layer deposition of SnO 2 on MXene for Li-ion battery anodes. *Nano Energy* **2017,** *34*, 249-256.

54. Wang, H.; Jiang, Y.; Manthiram, A., N-doped Fe3C@C as an efficient polyselenide reservoir for high-performance sodium-selenium batteries. *Energy Storage Mater.* **2019,** *16*, 374-382.

55. Zhao, X.; Yin, L.; Yang, Z.; Chen, G.; Yue, H.; Zhang, D.; Sun, Z.; Li, F., An alkali metal–selenium battery with a wide temperature range and low self-discharge. *J. Mater. Chem. A* **2019,** *7* (38), 21774-21782.

# Chapter 6 Conclusions

## 6.1 General conclusions

Cathode materials and separators are two of the most important components in batteries. Designing cathodes and separators with novel materials can greatly enhance the electrochemical performance of Li-Se and Na-Se batteries. In this PhD project, we firstly developed a novel material configuration for cathode material. Based on the *in-situ* polymerization method, an N, S dual-doped hierarchical porous carbon/Se composite coated with interconnected polyaniline (i-PANI@NSHPC/Se) was prepared with enhanced electrochemical performance in Na-Se batteries. Ex situ experiments were also conducted to investigate the mechanisms. The results are shown in Chapter 4.

The i-PANI@NSHPC/Se configuration has several advantages: 1) The hierarchical porous structure enables sufficient electrolyte penetration into the carbon host. 2) With the combination of PANI coating and heteroatoms doping, the 'shuttle effect' of polyselenides can be significantly suppressed owing to both physical confinement and chemical adsorption between the carbon matrix and $Na_xSe$ ($0<x\leq2$). 3) Moreover, the interconnected PANI networks provide high-speed transfer pathway for electrons and charges, enabling high rate performance.

The as-prepared i-PANI@NSHPC/Se cathode material can deliver a high reversible capacity of 617 mAh $g^{-1}$ after 200 cycles at 0.2 C, corresponding to 91.4% of its theoretical capacity. It also presents an excellent rate capability at 20 C of 380 mAh $g^{-1}$. Furthermore, stable cyclabilities over 1000 cycles have been achieved with different Se areal mass loadings (1.2, 2.3, 3.5 mg $cm^{-2}$) at 2 C.

Then, we also prepared novel self-assembled cetrimonium bromide (CTAB)/carbon nanotube (CNT)/$Ti_3C_2T_x$ MXene composite modified polypropylene (PP) (CCNT/MXene/PP) separator for improving the electrochemical performance of both Li-Se and Na-Se batteries. The CCNT/MXene/PP separator has favourable solid-electrolyte interface for fast redox reactions and electron/ion transport.

The adsorption property of MXene to polyselenides can be greatly enhanced due to the synergetic Lewis acid-base interaction between CTAB/MXene and negatively charged polyselenide anions. Meanwhile, the enlarged interlayer spacing due to the intercalation of CTAB molecules between MXene layers is beneficial for fast ionic transport. CNT network was incorporated into the MXene nanosheets to further improve the electrolyte penetration and prevent restacking of the delaminated MXene nanosheets. Owing to the flexible feature of 1D-CNT and 2D MXene materials, ultra-thin CCNT/MXene/PP separators with low areal mass loadings of ~0.09 mg $cm^{-2}$ have been obtained.

*In situ* permeation experiments were conducted for the first time to test the electrochemical behaviour of Li-Se batteries and the suppressed shuttle effect with CCNT/MXene/PP separator. The formation and diffusion of polyselenides during the intial cycles can be clearly observed. This fundamental study can provide more details and deep understanding for the Se-based battery behaviours.

When the CCNT/MXene/PP separator is applied in Li-Se batteries using commercial carbon black/Se cathode (high Se loading of 73.37 wt%), the battery delivered an outstanding cyclability with a low capacity decay of 0.05% per cycle over 500 cycles at 1 C. The free-standing carbon cloth/Se cathode with a high Se areal mass loading of 5.1 mg $cm^{-2}$ still maintained a capacity of 485 mAh $g^{-1}$ after 100 cycles. Furthermore, the functionalized separators also perform well in Na-Se batteries, achieving a high capacity retention of 72.6% upon 300 cycles.

Through this PhD study, a systematically study have been made on the Li-Se and Na-Se batteries. The two important components (cathodes and separators) have been optimized for favourable Se-based electrochemcail process.

## 6.2 Outlook

We have demonstrated that the electrochemical performance of Li-Se and Na-Se batteries can be significantly enhanced by developing novel materials for cathodes and separators. Several strategies for the cathode materials have been demonstrated to be effective in suppressing the shuttle effect while facilitating the redox reaction in Se-based batteries. By tuning the pore structure of hierarchical porous carbon materials, more active material (Se) can be effectively confined in micropores while the meso-/macropores are able to buffer the volume change during cycling and provide fast channels for electrolyte/electron/ion transport. Therefore, by designing a well-ordered hierarchical porous carbon with rational micro-/meso-/macropores, the host materials for the Se cathode can be further optimized and developed.

Doping with heteroatoms has been proved to provide strong chemical interaction between the substrates and polyselenides, leading to suppressed polyselenides shuttling and outstanding cycling stability. In theory, almost all the elements can be the dopants, the preparation method should also be facile and cost-effective. Therefore, the preparation of doping strategy with suitable dopants and substrates can be further investigated. Multi-atom doping with proper atom ratio should be further tuned for the best electrochemical performance.

It has been demonstrated that by coating with different materials on the Se/C composite, the electrochemical performance can be enhanced. However, it introduce additional components in the cathodes, leading to a lower overall Se content in the battery. In addition,

the coating method is usually complex and cannot be produced in large-scale. To solve this issues, our research indicated that the interconnected conductive polymer coating network can be facilely synthesized by tuning the concentration of monomers. Therefore, it can be further investigated by using different monomers and controlling the growth kinetics. Moreover, other coating methods, such as atomic layer deposition (ALD), in batteria electrochemical polymerization and ball-milling method, also deserves to be studied in the future.

Moreover, we have demonstrated that by modifying the separator with a favourable interface, the electrochemical performance of Li-Se and Na-Se batteries can be enhanced. The separators usually needs to be as thin and light as possible. It also needs to block the polyselenides shuttling via physical confinement, chemical adsorption or electrostatic attraction/repulsion without inhibiting the electron/ion transport. Finding different candidates to modify the separators, such as polymers, metal oxide, metal sulphides, metal selenides, carbon materials, can be the solutions. Therefore, it can be further investigated by preparing different modification methods/materials on the separators.

In summary, the materials prepared in this PhD project have been demonstrated to be beneficial for both Li-Se and Na-Se batteries. However, to develop more competitive materials for the next-generation batteries, future work is still needed in both cathode side and separators.

# Appendix A: Conferences

1. *International Coalition for Energy Storage and Innovation*, Australia, Sydney, 1-4 March 2020 (Oral Presentation).

2. *Preliminary program of 2019 International Symposium on Frontier Materials*, Australia, Sydney, 17-18 November 2019.

3. *2019 International Conference on Electrochemical Energy*, Australia, Sydney, 4-8 August 2019.

4. *International Conference for Energy Storage and Conversion*, Australia, Sydney, 16-18 July 2018.

# Appendix B: Scholarship & Awards

1. 08/2017-02/2021: UTS (University of Technology Sydney) President's Scholarship
2. 08/2017-02/2021: International Research Scholarship (University of Technology Sydney)
3. 09/2020: Paper of the Month - March and April 2020 Winners, University of Technology Sydney
4. 2010-2011: Second-class scholarship of Dalian Jiaotong University (three times)
5. 12/2011: Excellent Student of Dalian Jiaotong University
6. 06/2010: Second prize of Dalian City 19$^{th}$ College Student Mathematics Contest